UNIVERSITY OF OKLAHOMA

GRADUATE COLLEGE

THE DIRECT ANALYSIS OF SPECTRA OF TYPE IA SUPERNOVAE

A DISSERTATION

SUBMITTED TO THE GRADUATE FACULTY

in partial fulfillment of the requirements for the

degree of

DOCTOR OF PHILOSOPHY

By

Kazuhito Hatano
Norman, Oklahoma
2000

UMI Number: 9975802

THE DIRECT ANALYSIS OF SPECTRA OF
TYPE IA SUPERNOVAE

A DISSERTATION APPROVED FOR THE
DEPARTMENT OF PHYSICS AND ASTRONOMY

BY

D Branch

David Branch (Chair)

E Baron

Edward Baron

William Romanishin

William Romanishin

Ronald Kantowski

Kelvin Droegemeier

Acknowledgments

I wish to thank David Branch for his unlimited support, kindness, understanding, and patience for my works. Without his advisements, this thesis would not have been completed. I would also like to thank Eddie Baron for many discussions and answering my technical questions. I would also like to thank Bill Romanishin, Ron Kantowski, and Kelvin Droegemeier for serving as a committee member and offering useful advisements. I would like to thank the people in the supernova group, Adam Fisher, Peter Nugent, Dean Richardson, Eric Lentz, Darrin Casebeer, and Jennifer Deaton for their suggestions and discussions. I also wish to thank Nick and Penny Nicholas, my family, and my friends for kind supports. Finally, I wish to thank Peter Garnavich, Alex Filippenko, and Yulei Qiu for providing me lots of observed spectra and figures.

Table of Contents

Chapter 1

Introduction

Supernovae (SNe) are among the most fascinating events in the universe. Although SNe are explosion of stars at the final stage of stellar evolution, their maximum brightness usually becomes comparable to the brightness of a galaxy which consists of billions of stars. SNe also create and eject heavy elements such as carbon, oxygen, silicon, calcium, and iron which eventually become origin of planets and lives. Without SNe, no planet nor life could have been created because the Big Bang created only hydrogen and helium.

1.1 Classification of SNe

SNe may be classified into several types based on spectroscopy. First of all, we look for hydrogen lines in their spectra. If conspicuous hydrogen lines are not found, those SNe are classified into "type I" SNe (SNe I). If conspicuous hydrogen lines are present, those SNe are classified into "type II" SNe (SNe II). SNe I may further be sub-classified into "type Ia" (SNe Ia) if a conspicuous Si II line is found near 6150Å, "type Ib" (SNe Ib) if spectra are dominated by He I lines, or "type Ic" (SNe Ic) if neither Si II nor helium lines is strong. This dissertation focuses on the spectroscopic analysis of SNe Ia.

Spectroscopic analysis of SNe I is a relatively new research subject. For a long time, it was well-known that spectra of SNe I are alike, with a few exceptions (see Oke and Searle 1974 for those exceptions). But, it was not until the 1980's that spectra of SNe I were well understood. Branch et al. (1983) reported that, based on synthetic spectrum calculations, spectra of SNe I can be explained mainly by singly ionized intermediate mass elements such as Mg II, Si II, S II, and Ca II, and Fe II plus neutral elements such as O I and Na I. The results reported by Branch et al. are still used as the most general interpretation of spectra of typical SNe I.

By the mid-1980's, however, it was pointed out that spectra of some SNe I are fundamentally different from spectra of typical SNe I (Wheeler and Levreault 1985). First of all, in spectra of these SNe including ones discussed by Oke and Searle (1974), it was recognized that the conspicuous Si II line near 6150Å, which is characteristic of SNe I, is absent or weak. Then, Harkness et al. (1987) provided basic interpretations of these peculiar SNe I by proving that strong transitions of He I dominate their spectra. Based on these facts, it was decided that these peculiar SNe I should be called type Ib SNe, and other typical ones are type Ia SNe. In the late 1980's, some SNe, whose Si II line near 6150Å AND helium lines are weak or absent, were discovered. These SNe are called type Ic SNe today.

In 1991, two peculiar SNe Ia were discovered. In the spectra of the first one, SN 1991T, it was proven that strong Fe III lines are present (Filippenko et al. 1992b). On the other hand, Ti II transitions dominate the spectra of the second one, SN 1991bg (Filippenko et al. 1992a). Neither conspicuous Fe III nor Ti II had been identified in typical SNe Ia. But, these SNe are still classified into SNe Ia because the characteristic Si II line near 6150Å was identified in both of them. Moreover, their late time spectra are very much like those of typical SNe Ia. Branch et al. (1993) concluded that the majority of SNe Ia is spectroscopically normal (typical), and only 10 to 20 percent of SNe Ia in the current observational sample are peculiar like SNe 1991T, 1991bg, and 1986G (Ti II influences the spectra of SN 1986G, but not nearly as strongly as SN 1991bg).

1.2 Progenitor of SNe

The progenitors of SNe Ia are thought to be white dwarfs. White dwarfs are at the end point of the evolution of stars whose initial mass is less than 6 to 8 times the mass of the Sun ($M_\odot$). These low mass stars can burn hydrogen and helium by nuclear fusion, and eventually create a core which is mainly made from carbon and oxygen. But, the temperature of this core never becomes hot enough to start burning carbon. The core then tries to supply energy by contracting. But, eventually, contraction stops when the core becomes supported by degenerate electron pressure. At the same time, the star loses its outer envelope of hydrogen and helium by expansion. Within a relatively short period of time, the core alone remains. This remaining core, which is very hot, becomes a white dwarf mainly made from carbon, and supported by degenerate electron pressure.

White dwarfs cannot generate energy by their own; they cool down and eventually become invisible. But, when a white dwarf has a companion star (which could also be another white dwarf), the fate of a white dwarf may change. A white dwarf is supported by degenerate electron pressure. But, this pressure cannot support a white dwarf if its mass exceeds the so called *Chandrasekhar mass limit* which is about 1.4 $M_\odot$. When mass from a companion star transfers onto a white dwarf or when two white dwarfs merge, the total mass may reach or exceed 1.4 $M_\odot$. As a result, carbon burning starts, which ends up with a thermonuclear explosion of the white dwarf, which is observed as a type Ia supernova (SN Ia). Since a white dwarf has already lost hydrogen, no conspicuous hydrogen lines are expected in their spectra. But, these rapid thermonuclear reactions create various intermediate mass elements such as silicon, which is observed as the characteristic Si II line near 6150Å, and radioactive ^{56}Ni which decays to ^{56}Co and eventually to ^{56}Fe.

The progenitors of SNe Ibc are different from the progenitors of SNe Ia. Just as low mass stars, stars whose initial mass is greater than 6 to 8 $M_\odot$ create a carbon core. But unlike low mass stars, the temperature of this core becomes hot enough to start carbon burning (nuclear fusion). Nuclear reactions inside the core continue by creating various elments such as oxygen, neon, magnesium, silicon, sulfur and calcium; eventually, the core becomes mainly iron. Since iron is the most stable element, no energy is supplied from this iron core either by nuclear fusion or fission. Instead, iron absorbs energy which ends up with the collapse of the core.

The collapse of the core stops when the core becomes supported by repulsive forces between neutrons. This creates a powerful outward shock wave, which ends up with the explosion of the star. When a star has not lost its hydrogen envelope, conspicuous hydrogen lines are observed in its spectra (SN II). But, more massive stars have lost their hydrogen envelopes at the time of the explosion. Since their outermost layers are now made from helium, the spectra become dominated by lines of He I (SNe Ib). When a star is even more massive, it has lost even its helium envelope at the time of the explosion. As a result, no conspicuous lines of hydrogen, helium, nor silicon are observed in its spectra (SN Ic). Therefore, SNe Ibc are physically more related to SNe II than to SNe Ia.

1.3 Goal of This Dissertation

General interest in SNe is at an all-time high today. SNe Ia are not only the brightest type of SNe, but also their maximum brightness is highly homogeneous. Therefore, they have been used as a cosmological standard distance candle to determine the present cosmic expansion rate (H_0), the matter density parameter (Ω), and Einstein's cosmological constant (Λ). Accurate values of Ω and Λ will enable us to determine the space geometry and the fate of the universe. In the last year or so, general interest in SNe Ibc has also dramatically increased because of their apparent connection to gamma ray bursts. And, the number of supernova discoveries has been practically exploding. In 1998, about 150 new SNe were discovered compared to 20 or so per year in the 1980's. The amount of high-quality data has also been accumulating rather rapidly. Therefore, observation is well ahead of understanding and theory.

In order to use SNe Ia as a cosmological distance candle, however, it is essential to understand the spectra and nature of SNe Ia. For example, some peculiar SNe Ia do exist (e.g. those like SN 1991T, over–luminous events, and those like SN 1991bg, sub–luminous events). If SNe Ia are to be used as a standard candle in cosmology, these over–luminous and sub–luminous events must be excluded from the sample. It will be, therefore, vital to carefully analyze SNe spectra. Understanding any kind of spectroscopic sequence would also increase the efficiency of cosmological applications.

The main goal of this dissertation is to directly analyze spectra of SNe Ia at any photospheric phase, to increase the theoretical understanding. For this purpose, I use the fast, parametrized synthetic spectrum code, Synow, used in past by Dr. David Branch and his collaborators. This code is very useful to determine within which velocity interval an ion can be detected. Then, the inferred composition structure will give a guidence for those who work on hydrodynamical explosion models. In the past, this kind of collaboration led to the W7 model (Nomoto et al. 1984), the best explosion model for SNe Ia to date. I also use more empirical methods; measuring wavelengths of some spectral features by hand, and relating the information to other observables.

Chapter 2

Ion Signatures in Supernova Spectra

ABSTRACT

A systematic survey of ions that could be responsible for features in the optical spectra of supernovae is carried out. Six different compositions that could be encountered in supernovae are considered. For each composition, the LTE optical depth of one of the strongest optical lines of each ion is plotted against temperature. For each ion that can realistically be considered as a candidate to produce identifiable features in supernova spectra, a sample synthetic spectrum is displayed. The optical depth plots and the synthetic spectra can provide guidance to studies of line identifications in the optical spectra of all types of supernovae during their photospheric phases.

2.1 INTRODUCTION

Owing to the strong Doppler broadening and line blending in supernova spectra, making line identifications can be difficult. Although many of the major features in the optical spectra of supernovae have been identified, others still lack a secure identification. For example, some features that have occupied our attention recently are in the early spectra of the peculiar Type Ia SN 1991T (Fisher et al. 1999) and the early spectra of the peculiar Type Ic SN 1997ef (Deaton et al. 1998). Our difficulty in identifying some of the features in the spectra of these and other supernovae has motivated us to carry out a systematic survey of the ions that could produce features in the optical spectra of supernovae. Shortly after the appearance of the Type II SN 1987A in the LMC, such a survey was published by Branch (1987b), but only one composition was considered: hydrogen-rich, with a metallicity lower than solar by a factor of four. Here we consider six different compositions that could be encountered in supernovae.

In section 2, for each composition, LTE optical depths are calculated in the Sobolev approximation and plotted against temperature for one of the strongest optical lines of each ion. The LTE approximation has been shown to be useful for first-order interpretations of supernova spectra (e.g., Branch et al 1985; Jeffery & Branch 1990; Harkness 1991a,b; Jeffery et al 1991, 1992; Filippenko et al. 1992a; Kirshner et al. 1993). The optical depth plots of section 2 show which ions can be considered as candidates for line identifications, and at which temperatures. Then a synthetic optical spectrum for each candidate ion is displayed in section 3. These plots show the spectral signatures of each of the candidate ions.

2.2 LINE OPTICAL DEPTHS

2.2.1 Calculations

In the Sobolev approximation (Sobolev 1960, Castor 1970, Jeffery & Branch 1990), the optical depth of a line in a supernova that is expanding homologously with $v = r/t$ is

$$\tau = \left(\frac{\pi e^2}{mc}\right) f \lambda t n_l \left(1 - \left(\frac{g_l n_u}{g_u n_l}\right)\right) \tag{1}$$

where n_l and n_u are the number densities in the lower and upper levels of the transition, f is the oscillator strength, t is the time since explosion, and the other symbols have their usual meanings. The Sobolev line optical depth is inversely proportional to the velocity gradient, i.e, proportional to t, because as a photon propagates it redshifts with respect to the matter; the larger the velocity gradient, the sooner the photon redshifts out of resonance with the transition, and the smaller the line optical depth. A convenient numerical form of equation (1) is

$$\tau = 0.026 f \lambda_\mu t_d n_l \left(1 - \left(\frac{g_l n_u}{g_u n_l}\right)\right) \tag{2}$$

where λ_μ is in microns, t_d is in days, and n_l is in cm^{-3}.

In this chapter we evaluate all line optical depths at the layer in the supernova where the electron scattering optical depth, τ_{es}, reaches unity. When electron scattering is the dominant opacity source, this layer can be thought of, roughly, as the bottom of the line–forming layer (although thermalization of the continuum will take place at a deeper layer or, in SNe Ia, perhaps not at all), and only transitions that achieve optical depths on the order of unity or greater at $\tau_{es} = 1$ will be able to form conspicuous features in the spectrum. We also will encounter situations where the electron scattering opacity will be smaller than the combined opacity of numerous lines. Then, effectively, the bottom of the line forming layer will be at a shallower layer in the supernova, and only lines that have optical depths well in excess of unity at $\tau_{es} = 1$ will be able to produce identifiable spectral features.

If the electron density is taken to decrease outward as a power law of index n, the electron density at $\tau_{es} = 1$ is given by

$$n_e = (n - 1)/(\sigma_e R) \tag{3}$$

where σ_e is the Thomson cross section and R is the radius at which $\tau_{es} = 1$. We use $n = 7$ and a characteristic value of $R = 1.73 \times 10^{15}$ cm, which corresponds to $v_{phot} = 10,000$ km s^{-1} and $t = 20$ days. This gives $n_e = 5.2 \times 10^9$ cm^{-3}, which is used for all of the optical depth calculations of this chapter. A value of $t = 20$ days also is used in equation (2), except in section 2.7 where we discuss the time–dependent nickel–cobalt–iron composition that results from the radioactive decay of ^{56}Ni and ^{56}Co. The use of constant characteristic values of n_e and t is sufficient for our purposes because the limiting approximation of this work is that of LTE.

Table 1 lists the relative abundances of the elements for five of the six compositions that we consider. The entries are logarithms of the abundance by number. Only the relative abundances are relevant; the absolute numbers have no significance. The way in which we arrived at each of these compositions, and where in supernovae they might be encountered, will be discussed below as the line optical depths are presented for each composition. (The sixth composition that we consider is the time–dependent mixture of nickel, cobalt, and iron that results from an initially pure ^{56}Ni composition.) Given the electron density and a composition, the Saha ionization and Boltzmann excitation equations are used to calculate the atomic level populations as well as the total gas density that is needed to provide the specified electron density. Figure 1, which shows the total density plotted against temperature for each of the six compositions, will be helpful in understanding the optical depth plots. As temperature falls, and significant donors of free electrons recombine, the total density rises in order to achieve the specified electron density. For example, for the solar composition, the density rise at $T <\approx 6000$ K is caused by hydrogen recombination, and for

element	atomic weight	H–rich	He–rich	C/O–rich	C–burned	O–burned
H	1.0	12.00	—	—	—	—
He	4.0	10.99	11.54	—	1.90	1.85
Li	7.0	1.16	1.16	1.16	—	—
Be	9.0	1.15	1.15	1.15	—	—
B	11.0	2.60	2.60	2.60	—	—
C	12.0	8.60	8.60	10.77	9.02	6.43
N	14.0	8.00	8.00	8.00	—	—
O	16.0	8.93	8.93	10.65	11.84	7.45
F	18.0	4.56	4.56	4.56	—	—
Ne	20.0	8.09	8.09	8.09	8.11	3.91
Na	23.0	6.33	6.33	6.33	7.52	4.10
Mg	24.0	7.58	7.58	7.58	10.81	7.22
Al	27.0	6.47	6.47	6.47	—	—
Si	28.0	7.55	7.55	7.55	11.18	11.76
P	31.0	5.45	5.45	5.45	9.44	6.23
S	32.0	7.21	7.21	7.21	10.84	11.45
Cl	35.0	5.50	5.50	5.50	8.41	7.00
Ar	36.1	6.56	6.56	6.56	9.84	10.62
K	39.0	5.12	5.12	5.12	7.17	6.87
Ca	40.0	6.36	6.36	6.36	8.28	10.44
Sc	44.5	3.10	3.10	3.10	5.94	5.60
Ti	45.0	4.99	4.99	4.99	7.95	8.30
V	48.5	4.00	4.00	4.00	7.46	7.97
Cr	50.5	5.67	5.67	5.67	7.81	9.52
Mn	52.8	5.39	5.39	5.39	6.47	9.31
Fe	54.6	7.67	7.67	7.67	8.49	10.86
Co	56.0	4.92	4.92	4.92	8.65	6.29
Ni	56.8	6.52	6.52	6.52	8.80	9.53
Sr	87.6	3.02	3.02	3.02	—	—
Ba	137.3	2.10	2.10	2.10	—	—

Table 2.1: Atomic Abundances

fig1

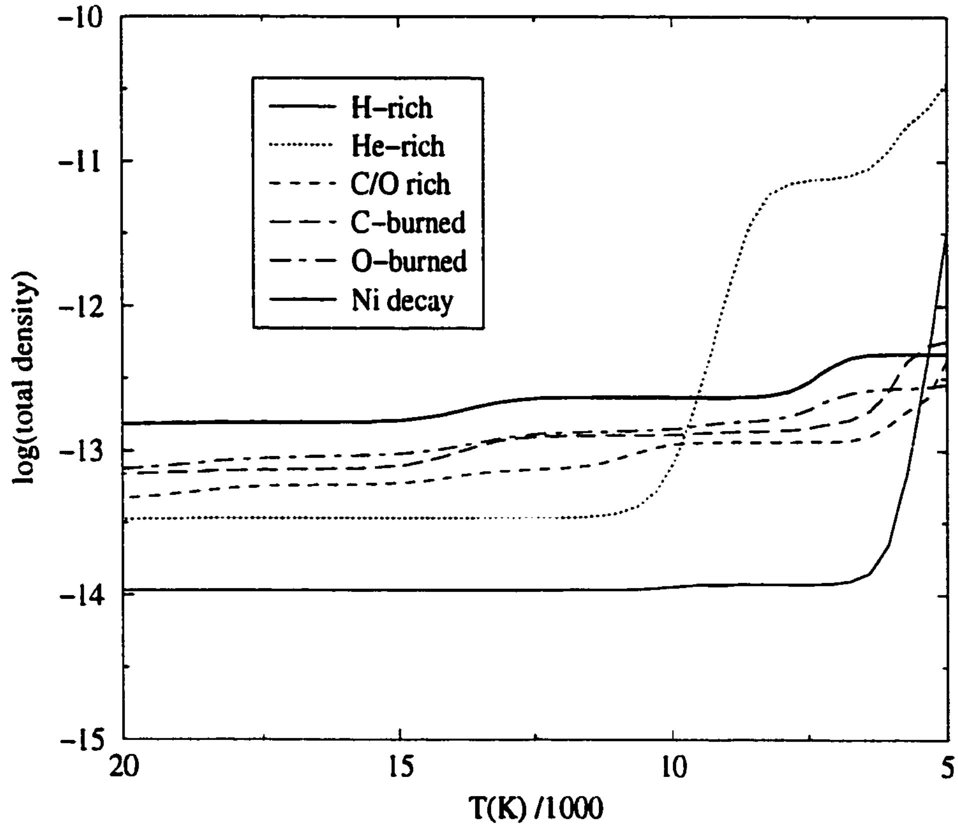

Figure 2.1: The log of the total density (gm cm^{-3}) at $\tau_{es} = 1$ is plotted against temperature for six different compositions.

the helium–rich composition the steep density rise at $T <\approx 10,000$ K is caused by helium recombination.

For each ion, the optical depth of a reference line is calculated as a function of temperature. One of the ion's strongest lines in the range $4000 < \lambda < 10,000$ Å is chosen to be the reference line. Note that for O III and O II we are using forbidden lines as the reference lines, because they are stronger than any of the permitted lines in the temperature range considered here. The optical depth plots show the reference lines that achieve $\tau > 0.001$ within the range $20,000 > T > 5,000$ K. These reference lines are listed in Table 2, along with their $\log(gf)$ values and excitation potentials. The entry following the wavelength tells in which optical depth plots the ion makes an appearance; for example, 234 means that the ion appears on the optical depth plots for the second, third, and fourth compositions that we consider.

In this chapter we make no allowance for nonthermal excitation and ionization. This is known to be significant for He I in the post–maximum spectra of Type Ib supernovae (Harkness et al. 1987; Lucy 1991) and may also be significant during certain phases of Type II (Jeffery & Branch 1990) and Type Ic supernovae (Clocchiatti et al. 1997 and references therein; Millard et al. 1999). Such effects are discussed briefly below, when they may be relevant.

2.2.2 Hydrogen–rich

The early spectra of Type II supernovae are formed in a hydrogen–rich composition, so we begin by considering the solar composition.

The optical depths are plotted in Figure 2. At high temperature no lines have $\tau > 1$, and only Hα has $\tau > 0.1$. As the temperature falls, $H\alpha$ becomes strong, followed by Ca II, Fe II, Ti II, and Sc II. Hydrogen is the main provider of free electrons throughout our temperature range, but at $T \simeq 6000$ K it begins to become mostly neutral so the density must rise (Figure 1) to provide the specified electron density. This is the cause of the increase of the optical depths of singly ionized species

ion	λ		log(gf)	χ (eV)	ion	λ		log(gf)	χ (eV)
H I	6563	1	0.71	10.21	K I	7665	12345	0.13	0.00
He I	5876	12	0.41	20.99	Ca I	4227	12345	0.26	0.00
He II	4686	12	1.18	48.43	Ca II	3934	12345	0.15	0.00
C I	9095	1234	0.07	7.49	Sc I	4024	1245	0.41	0.02
C II	4267	1234	0.77	18.07	Sc II	4247	12345	0.32	0.32
C III	4647	1234	0.08	29.57	Ti I	4533	12345	0.55	0.85
C IV	5801	3	-0.20	37.60	Ti II	4550	12345	-0.45	1.58
N I	8680	123	0.24	10.35	Ti IV	5399	45	0.16	26.37
N II	5680	123	0.28	18.51	V I	4379	12345	0.59	0.30
N III	4097	123	-0.02	27.47	V II	4006	12345	-0.76	1.82
O I	7772	12345	0.32	9.16	V III	4070	45	-2.04	7.86
[O II]	7321	234	-8.43	3.33	Cr I	4254	12345	-0.11	0.00
[O III]	4363	234	-8.34	2.52	Cr II	4242	12345	-0.59	3.87
Ne I	6402	23	0.36	16.64	Cr III	5640	45	-2.12	10.47
Na I	5890	1234	0.12	0.00	Cr IV	5940	5	-1.97	19.29
Mg I	5184	12345	-0.18	2.72	Mn I	4031	12345	-0.44	0.00
Mg II	4481	12345	0.74	8.87	Mn II	4205	12345	-3.58	1.81
Al I	8774	12	-0.02	4.02	Mn III	4470	5	-2.18	11.76
Al II	7042	123	0.35	11.33	Mn IV	4238	5	-2.32	18.96
Al III	5697	123	0.23	15.66	Fe I	4046	123456	0.28	1.48
Si I	7944	1245	-0.38	5.98	Fe II	5018	123456	-1.40	2.89
Si II	6347	12345	0.30	8.13	Fe III	4420	123456	-2.22	8.24
Si III	4553	12345	0.18	19.04	Fe IV	4005	23456	-1.87	23.64
Si IV	4089	12345	0.20	24.08	Co I	4121	12456	-0.60	0.92
P I	9797	124	0.22	6.99	Co II	4161	123456	-1.83	3.41
P II	6508	234	0.62	10.90	Co III	4433	46	-2.36	10.41
P III	4222	34	0.21	14.63	Co IV	4246	6	-4.20	16.48
P IV	4250	4	0.00	29.05	Ni I	5477	123456	-0.35	1.83
S I	9213	12345	0.42	6.53	Ni II	4067	123456	-1.84	4.03
S II	5454	12345	0.56	13.69	Ni III	4613	456	-2.89	12.15
S III	4254	12345	0.40	18.27	Ni IV	4316	6	-2.59	23.09
Cl I	8376	24	0.46	8.93	Sr II	4078	123	0.17	0.00
Cl II	4795	245	0.46	13.39	Ba II	4554	123	0.19	0.00
Ar I	8115	245	0.41	11.56					
Ar II	4348	2345	0.47	16.64					
Ar III	4171	45	-2.21	22.43					

Table 2.2: Reference Lines

such as Si II and Mg II at $T <\approx 6000$ K. At these low temperatures, lines of many neutral species achieve $\tau > 1$, as do the resonance lines of Sr II and Ba II.

Because hydrogen is the main source of free electrons, the effect of changing the metallicity is simple: the optical depths of all the heavy–element lines are proportional to the metallicity while the hydrogen and helium optical depths are unaffected. Lowering the hydrogen abundance in favor of helium would leave the hydrogen lines almost unaffected, because the total density would rise to give almost the same hydrogen density at the photosphere. The density rise would cause a strengthening of the metal lines, and helium lines would strengthen even more because of the increased helium abundance.

Most of the line optical depths are proportional to the square of the electron density. One factor of n_e comes just from the associated increase in the total density, while the other comes from the Saha equation. This is because the lines of interest generally come not from the most abundant ion, but from the one that is once less ionized. For hydrogen, for example, increasing the specified electron density would not only increase the total hydrogen density but also the fraction of hydrogen that is neutral, except for $T <\approx 6000$ K where most of the hydrogen already is neutral.

The LTE optical depths of Figure 2 are, at least qualitatively, nicely consistent with the observed evolution of the spectra of Type II supernovae. Before and around the time of maximum light, SNe II are hot and their spectra are continuous except perhaps for weak hydrogen lines. As SNe II cool the hydrogen lines strengthen, followed by lines of Ca II, Fe II, Ti II and Sc II, as predicted. The most obvious discrepancy between prediction and observation is that the Na I D lines are calculated to be only about as strong as the reference lines of a number of other neutral species, whereas in the spectra of SNe II the feature produced by the D lines is considerably stronger than the lines of other neutrals. The answer, presumably, lies in non–LTE effects. A detailed study of line identifications in SN 1987A was carried out by Jeffery & Branch (1990). In that particular case, too, the order of appearance of the lines was very much as discussed above. Lines that could be identified with confidence were

Fig 2

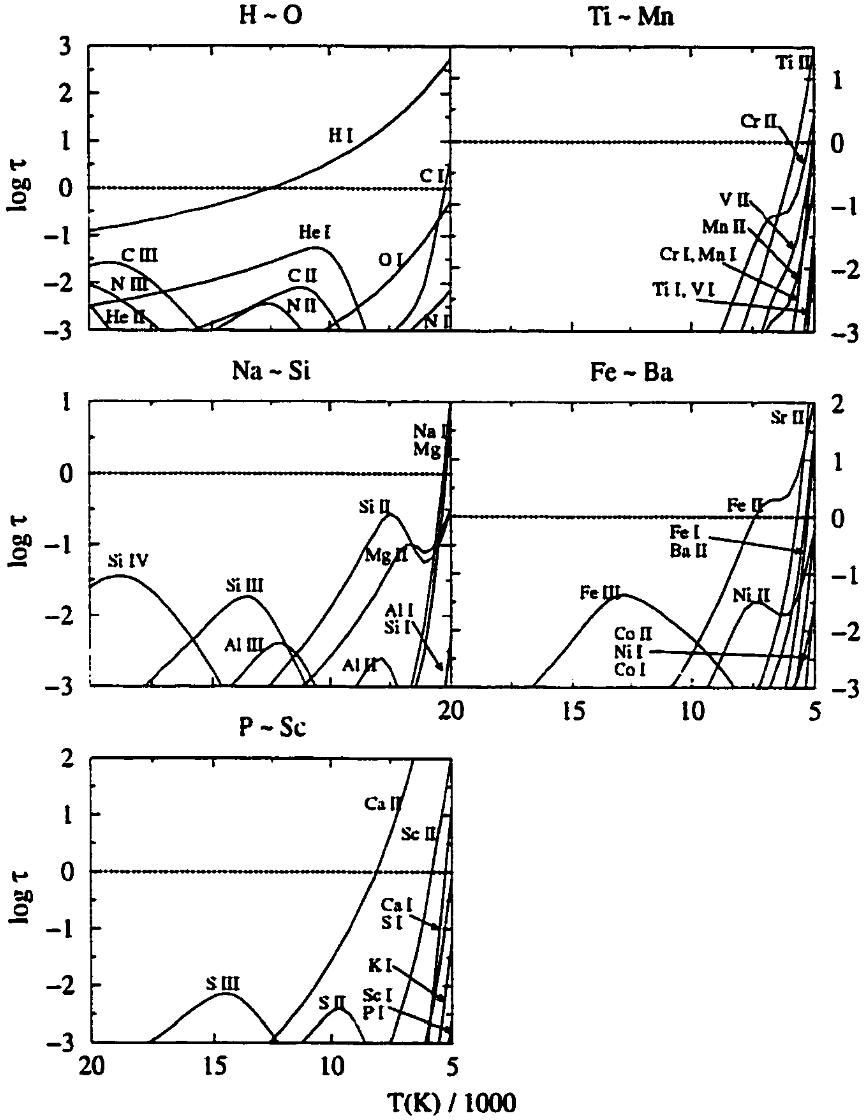

Figure 2.2: The log of the Sobolev LTE optical depth of ion reference lines, evaluated at $\tau_{es} = 1$, is plotted against temperature for the hydrogen–rich composition.

from H, He I, Na I, Ca II, Sc II, Fe II, and Ba II. The very early appearance of a weak He I $\lambda5876$ line possibly was due to an enhanced abundance of helium in the outer hydrogen-rich layers of SN 1987A, and the later (probable) appearance of the He I line is attributable to nonthermal excitation and ionization caused by the products of the radioactive decay of ^{56}Co. The appearance of conspicous Ba II lines probably was due to an overabundance of barium (Mazzali & Chugai 1995 and references therein).

The satisfactory agreement between calculated LTE optical depths and observation of SNe II suggests that the LTE optical depths presented below, for other compositions, also can be helpful for line identification studies.

2.2.3 Helium-Rich

The surface layers of SNe Ib are hydrogen-deficient and helium-rich, as may be the surface layers of SNe Ic. Such a composition also will be present, of course, beneath the outer hydrogen-rich layers of SNe II. We consider a helium-rich composition that is obtained by "burning" all of the hydrogen to helium. This increases the helium number abundance, relative to the heavier elements, by a factor of 3.55. (We make no allowance for conversion of carbon and oxygen into nitrogen by means of the CNO cycle.)

As can be seen in Figure 1, the density at the photosphere is higher in the helium-rich case than in the hydrogen-rich case, by a factor of about 3.1 when helium is singly ionized ($T >\approx 10,000$ K), but by a factor about 600 at $T \simeq 7500$ K, where helium is neutral. Figure 3 shows that at low temperature, oxygen, and then carbon, become the main sources of free electrons.

The line optical depths are shown in Figure 4. Apart from the absence of the hydrogen line and the strengthening of He I and He II due to the abundance change, the differences between the optical depths in the helium-rich and hydrogen-rich cases just reflect the difference in the density at $\tau_{es} = 1$, as a function of temperature. At high temperature no lines achieve $\tau > 1$, and the He I line just makes it at $T \simeq 8000$

Fig 3

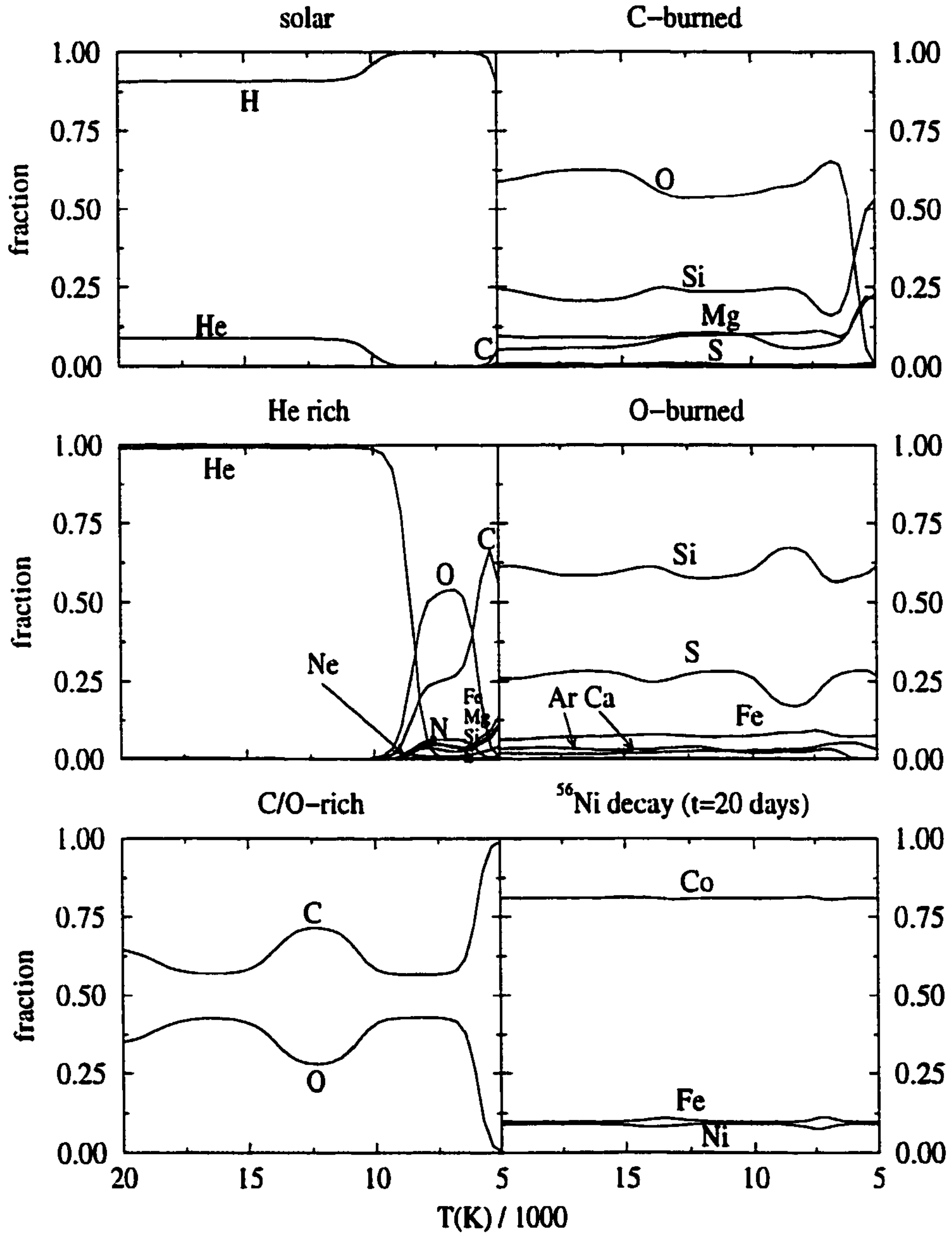

Figure 2.3: The fractional contribution of free electrons is plotted against temperature for six different compositions.

Fig 4

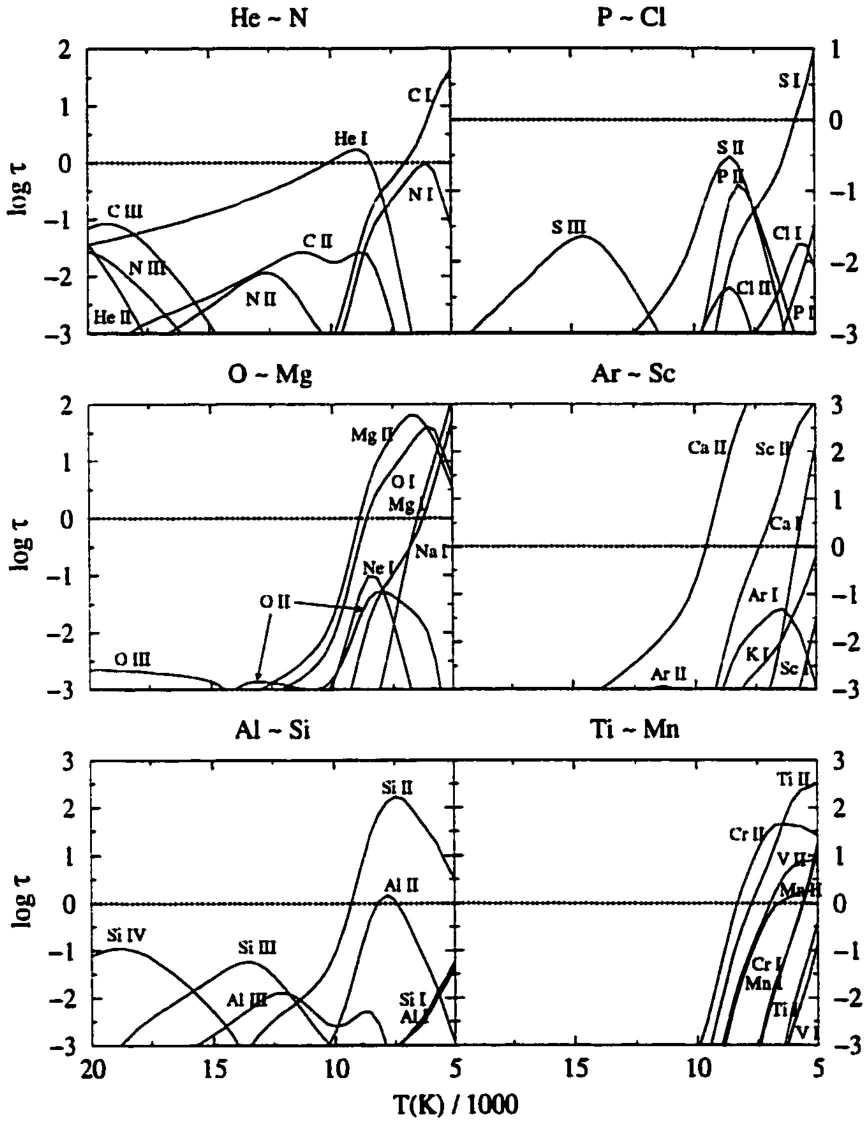

Figure 2.4: The log of the Sobolev LTE optical depth of ion reference lines, evaluated at $\tau_{es} = 1$, is plotted against temperature for the helium–rich composition.

Fig 4.2

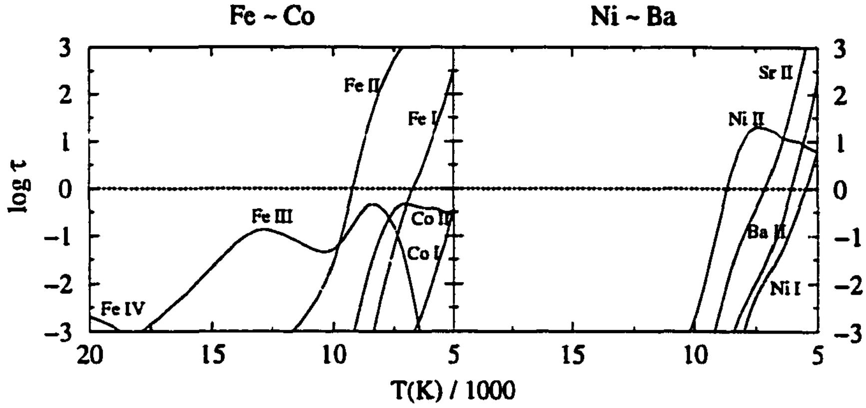
Fe ~ Co
Ni ~ Ba
log τ
Fe II
Fe I
Fe III
Co II
Co I
Fe IV
Sr II
Ni II
Ba II
Ni I
T(K) / 1000

K. Considering the limitations of the LTE approximation, this means that the absence of conspicuous He I lines, at any temperature, is not evidence against a helium-rich composition. For $T <\approx 10,000$ K, helium begins to recombine, the density rises sharply, the lines of heavy elements become much stronger at $\tau_{es} = 1$ than they were in the hydrogen-rich case, and line opacity dominates over electron scattering.

As is well known, the strong He I lines that are observed in the post-maximum light photospheric phases of SNe Ib require nonthermal excitation and ionization. Because the nonthermal effects increase the ionization of helium, whenever they occur they will cause the sharp density rise and the corresponding strengthening of the heavy element lines to shift to lower temperature than seen in Figure 4.

2.2.4 Carbon/Oxygen-Rich

The outermost layers of SNe Ia and SNe Ic may be carbon/oxygen-rich. For example, in the model W7 (Nomoto, Thielemann, & Yokoi 1984) the composition is C/O-rich down to 14,900 km s^{-1}. We consider a composition that is obtained by burning all of the helium into equal amounts of carbon and oxygen by mass. This raises the carbon and oxygen number abundances, relative to the heavy elements, by factors of 147 and 52, respectively, and makes carbon more abundant than oxygen by a factor of 1.3.

Carbon and oxygen are the principal sources of free electrons. Figure 1 shows that the density does not vary strongly with temperature. For $T >\approx 10,000$ K the density is somewhat higher than in the hydrogen and helium rich cases, but the density does not increase sharply at low temperature because carbon remains partially ionized down to 5000 K.

The line optical depths are shown in Figure 5. Now, for the first time, we see a line having $\tau > 1$ at high temperature — that of C III — and at intermediate temperature the C II line has $\tau > 1$. The forbidden reference lines of [O III] and [O II] have $\tau > 0.1$. At low temperature, the O I and C I lines are only about as strong as they were in the helium-rich case, because in both cases the free electrons

Fig 5

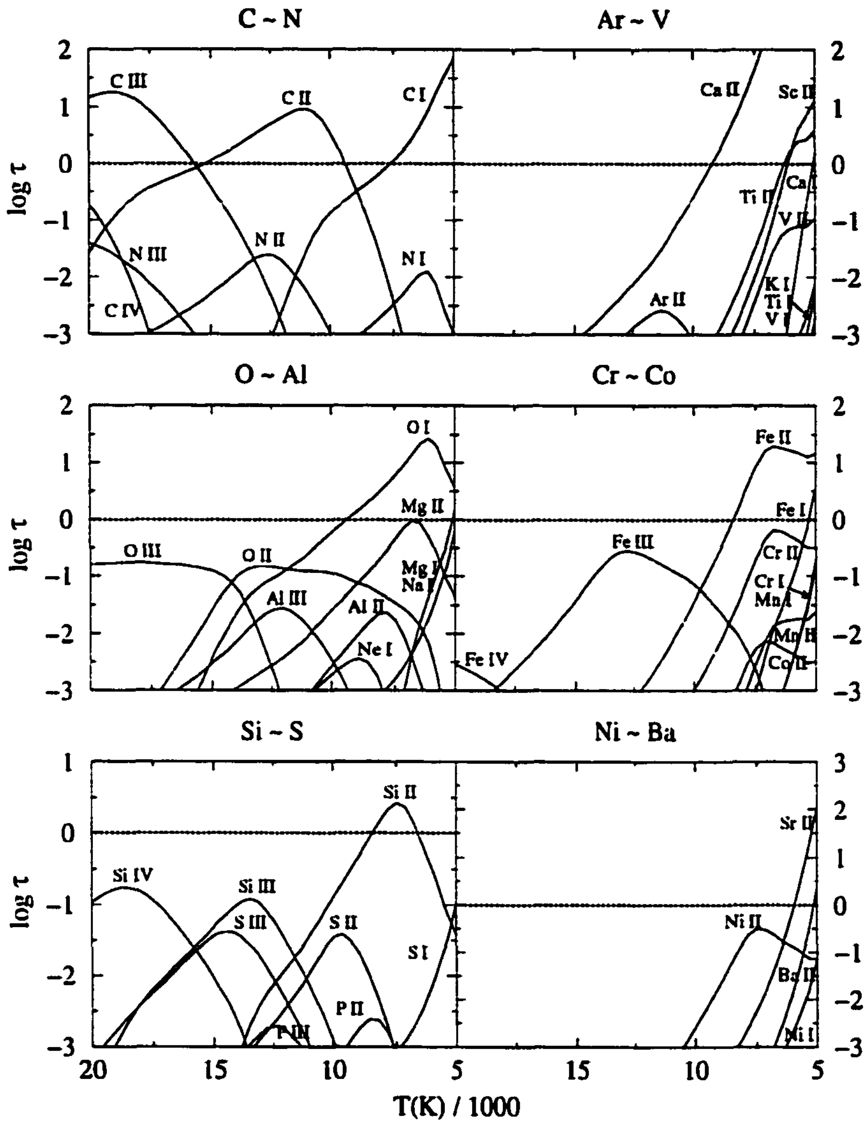

Figure 2.5: The log of the Sobolev LTE optical depth of ion reference lines, evaluated at $\tau_{es} = 1$, is plotted against temperature for the C/O–rich composition.

are mainly provided by carbon and oxygen. This means that, at least in LTE, the strength of the O I λ7773 line cannot discriminate between a helium–rich and a C/O–rich composition. At low temperature the lines of elements heavier than oxygen are stronger than they were in the hydrogen–rich case, but not nearly as strong as they were in the helium–rich case, because their abundances relative to the main providers of free electrons, carbon and oxygen, are now reduced.

2.2.5 Carbon–burned

Layers in which carbon has burned are expected to be encountered in the surface or subsurface layers of SNe Ia, and they are exposed above the photosphere before the time of maximum light. In model W7, the carbon–burned composition extends from 14,900 to about 13,000 km s^{-1}. For a carbon–burned zone we consider composition number 5 from Table 3 of Khokhlov, Müller, & Höflich (1993). Oxygen is the most abundant element, followed by silicon, sulfur, and magnesium. Oxygen is the main source of free electrons, except for $T <\approx 6000$ K where it recombines and silicon takes over. Figure 1 shows that the density runs somewhat higher than that of the C/O–rich composition.

The optical depths are plotted in Figure 6. At high and intermediate temperatures, lines of silicon and sulfur ions are strong, and it is interesting that lines of P III and P II also have $\tau > 1$. At $T <\approx 8000$ K lines of Si II, Ca II, and Mg II become very strong, and at $T <\approx 7000$ K lines of additional singly ionized and some neutral species also become strong. The O I line does not get much stronger than it was in the helium–rich and C/O–rich cases, so again the O I λ7773 line is not a good composition indicator.

2.2.6 Oxygen–burned

In model W7 a layer in which oxygen has burned extends from about 9000 to 13,000 km s^{-1}. We consider composition number 4 from Table 3 of Khokhlov et al. (1993).

Fig 6

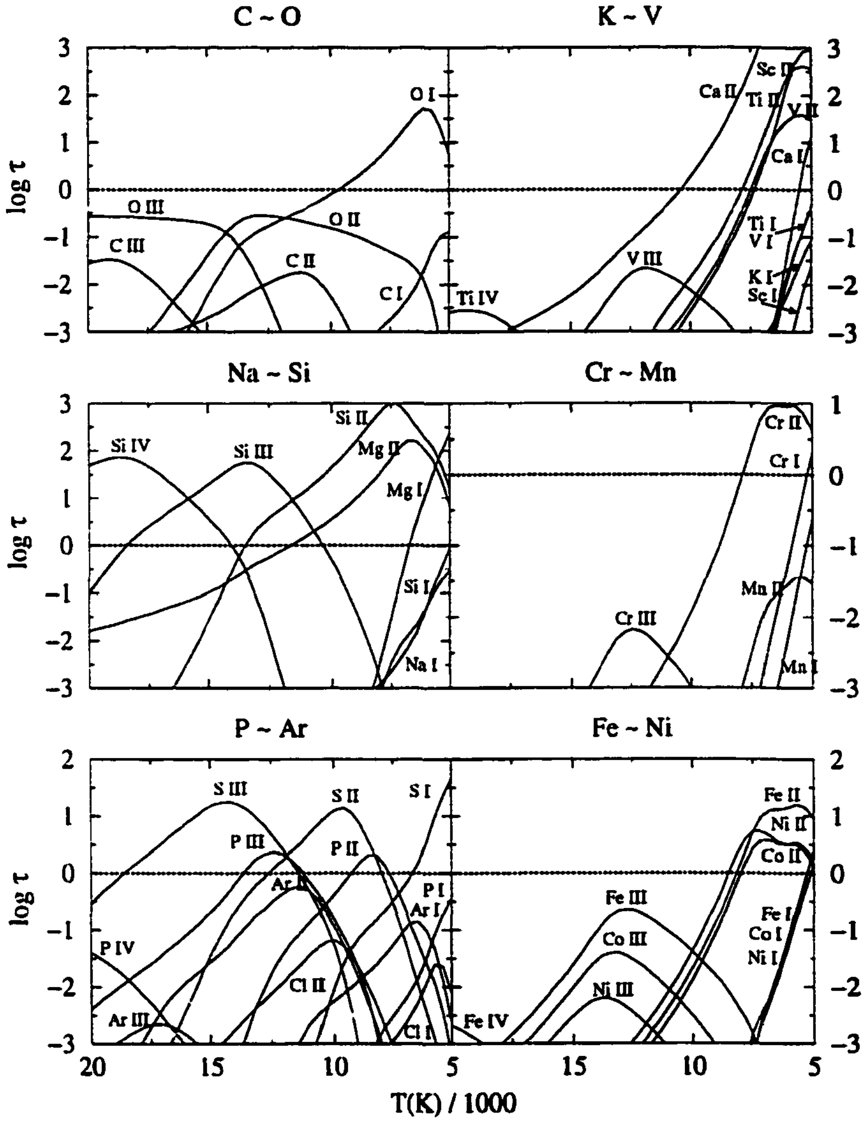

Figure 2.6: The log of the Sobolev LTE optical depth of ion reference lines, evaluated at $\tau_{es} = 1$, is plotted against temperature for the carbon–burned composition.

Fig 7

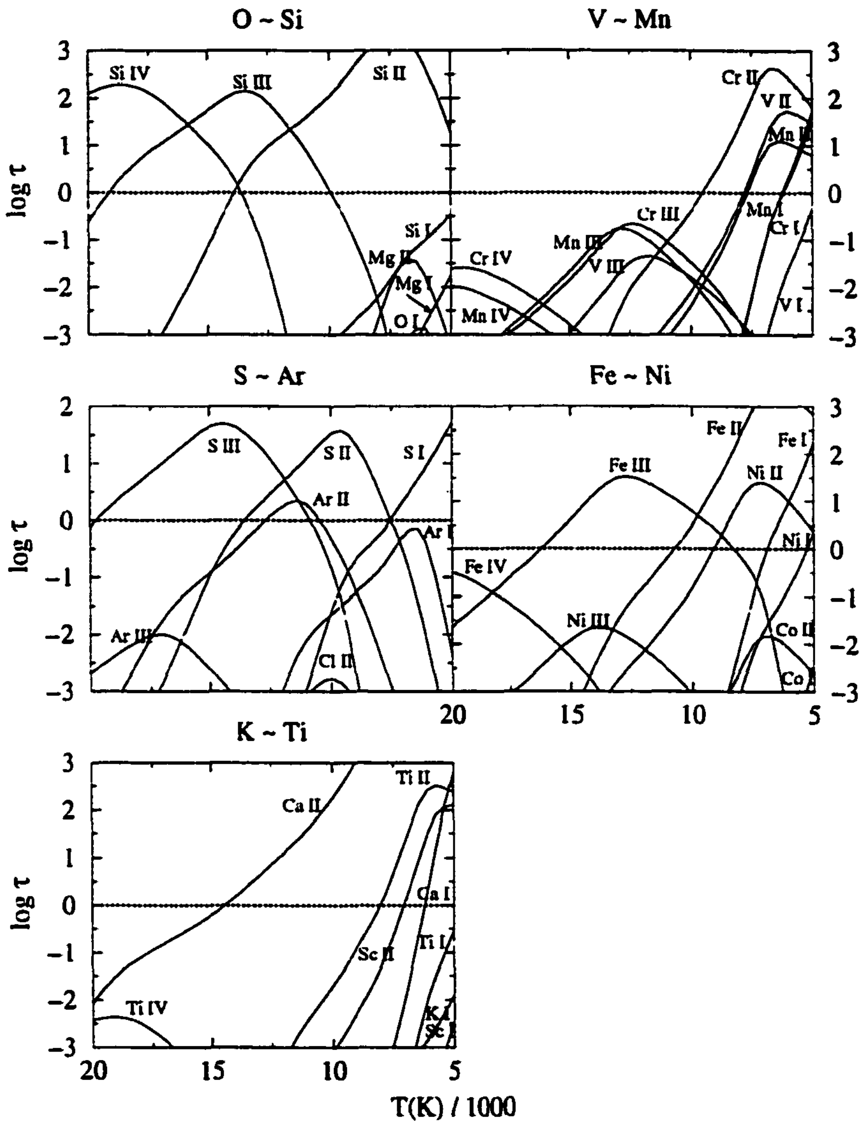

Figure 2.7: The log of the Sobolev LTE optical depth of ion reference lines, evaluated at $\tau_{es} = 1$, is plotted against temperature for the oxygen–burned composition.

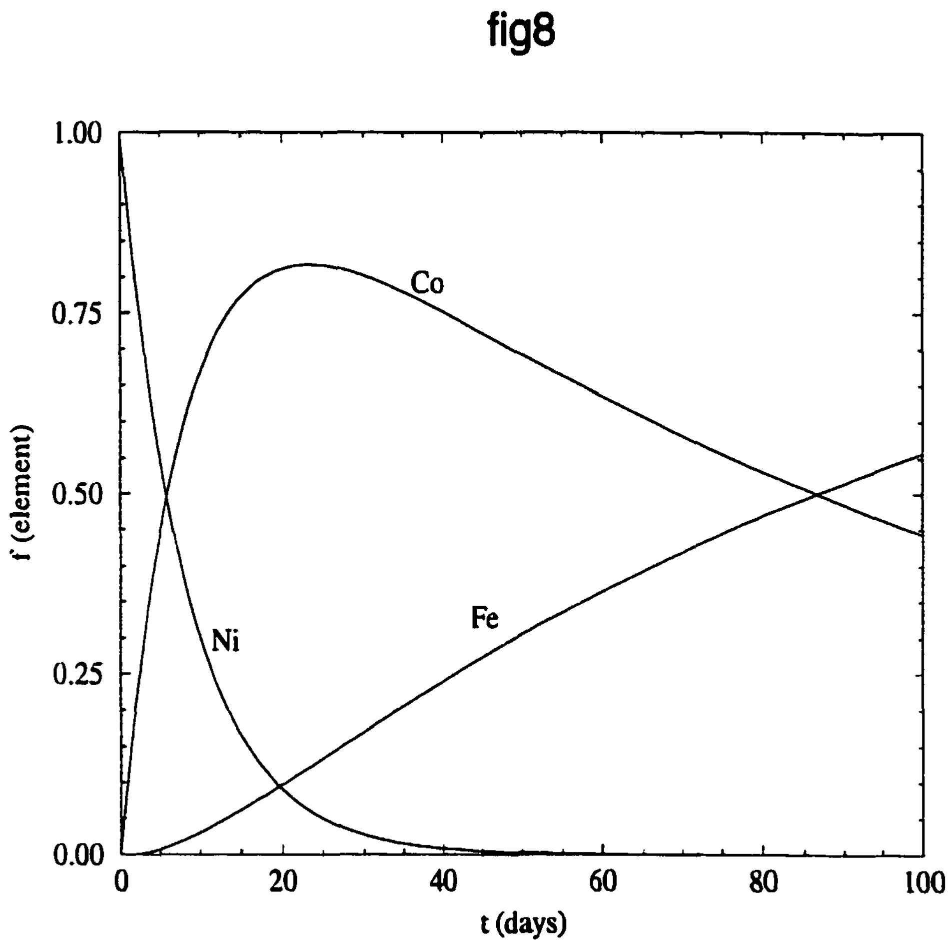

Figure 2.8: The fractional composition is plotted against time for the ^{56}Ni-decay composition.

The most abundant elements are silicon, sulfur, iron, argon, and calcium. Silicon is the main source of free electrons, and the density runs somewhat higher than in the carbon–burned case (Figure 1).

The optical depths are plotted in Figure 7. The main qualitative differences between these plots and those of the carbon–burned case are the disappearance of the oxygen and phosphorus lines, the weakening of Mg II, and the strengthening of Ca II, Fe III, and Fe II.

2.2.7 Nickel–decay

The sixth composition that we consider is the time dependent mixture of nickel, cobalt, and iron that results from the decay of ^{56}Ni through ^{56}Co to stable ^{56}Fe. This composition has been suggested to dominate the outermost layers of the peculiar Type Ia SN 1991T (Filippenko et al. 1992b, Ruiz–Lapuente et al. 1992), or at least to be an significant component of those layers (Jeffery et al. 1992, Mazzali et al. 1995, Fisher et al. 1999), and large amounts of ^{56}Ni are present beneath the oxygen–burned zone in normal SNe Ia. Figure 8 shows the time dependent fractional abundances of nickel, cobalt, and iron, assuming an initially pure ^{56}Ni composition and using half lives of 6 and 77 days for ^{56}Ni and ^{56}Co, respectively.

The density plotted in Figure 1 is for $t = 20$ days. It is only a very weak function of the time, owing to the similar ionization potentials of nickel, cobalt, and iron. The density runs somewhat higher than in the oxygen–burned case, and it does not vary strongly with temperature.

Figure 9 shows the line optical depths for three different times: $t = 5$ days, when the fractional concentrations of nickel, cobalt, and iron are 0.55, 0.45, and 7×10^{-3}, respectively; at $t = 20$ days (0.09, 0.81, 0.1); and $t = 80$ days (7×10^{-5}, 0.53, 0.47). At 5 and 20 days, lines of the doubly or (depending on temperature) singly ionized species of all three elements are candidates for producing spectral features. At 80 days nickel lines are no longer a consideration.

Fig 9

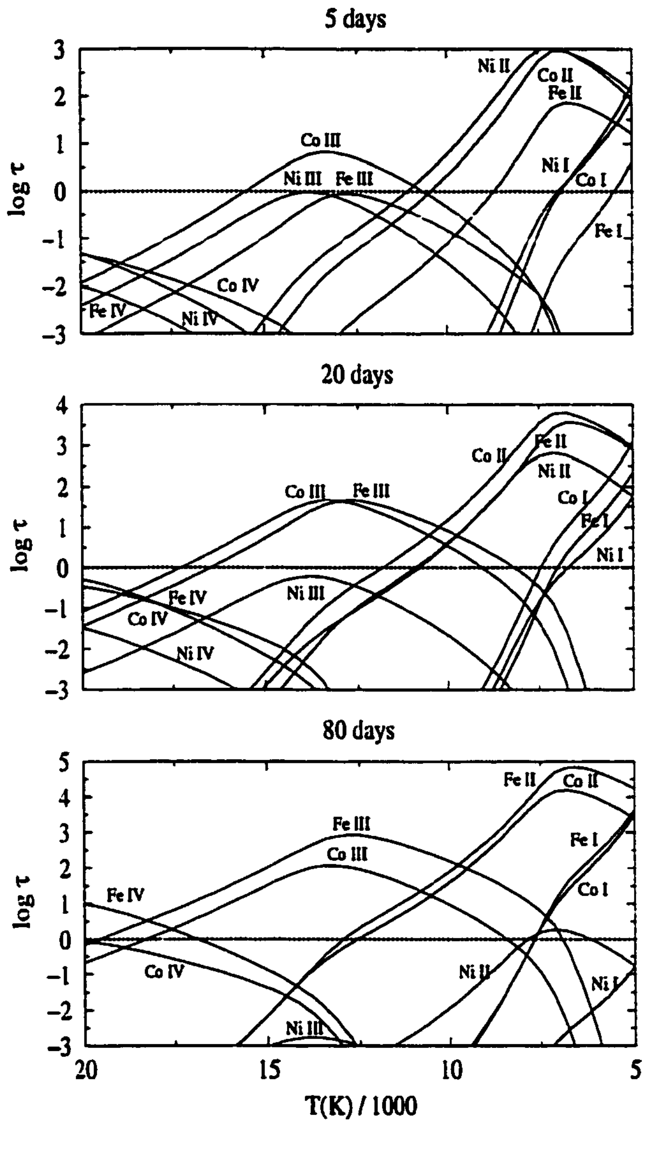

Figure 2.9: The log of the Sobolev LTE optical depth of ion reference lines, evaluated at $\tau_{es} = 1$, is plotted against temperature for the ^{56}Ni–decay composition at times of 5, 20, and 80 days.

2.3 SYNTHETIC SPECTRA

In Figure 10 a sample synthetic spectrum is displayed for every ion that we consider to be a realistic candidate for producing an individually recognizable feature in the optical spectrum of a supernova. Not every ion that is listed in Table 2 appears in Figure 10. An ion such as V I, for example, that appears on an optical depth plot only in situations where numerous other ions are much stronger, is not a realistic candidate for producing identifiable spectral features.

Although the reference lines were selected from lines that have $\lambda < 10,000$ Å, the synthetic spectra of Figure 10 extend to 12,000 Å. The purpose of this is to show the feature produced by λ10830 of He I, as well as features produced by other species such as Si I, which might produce the near infrared absorption feature that was observed in the spectrum of the Type Ic SN 1994I by Filippenko (1995). A discussion of the identification of this feature is presented by Millard et al. (1999).

The synthetic spectra are calculated with the parameterized supernova spectrum synthesis code SYNOW, which is an improved version of the code that has been used by in the past by, for example, Branch et al. (1985) and Filippenko et al. (1992a). The current version of SYNOW is described briefly by Fisher et al. (1997) and in detail by Fisher (2000). For the purposes of this spectrum atlas, we use the following parameters: the temperature of the blackbody continuum is 10,000 K; the line optical depths decrease outwards as a power law of index 7; the velocity at the photosphere is 5000 km s^{-1}; and the line forming region is truncated on the outside at a velocity of 30,000 km s^{-1}. The optical depth of the reference line at the photosphere ordinarily is taken to be 10, but for some ions it is raised or lowered in order to better illustrate the spectral signature of the ion. Different excitation temperatures are used for different ionization stages because, for example, lines of most neutral species have no chance of being seen unless the temperature is low. The excitation temperature is taken to be 5000 K for neutral species; 10,000 K for singly ionized; 15,000 K for doubly ionized; and 20,000 K for triply ionized.

Our intention here has been to show a synthetic spectrum for every ion that can realistically be considered as a candidate for producing an identifiable feature in the optical spectra of supernovae. Consequently the optical depth plots and synthetic spectra displayed in this chapter can be used as a guide to line identifications in the optical spectra of all types of supernovae in their photospheric phases.

Figures and electronic versions of figures 10 may be obtained at:
http://www.nhn.ou.edu/~baron/papers.html

2.4 Additional discussions

Figs. 11, 12, and 13 show how the optical depth plot is changed when some input parameters are varied. Fig. 11 shows that increasing metallicity by a factor of 2 will result in increasing optical depth of metals by a factor of 2. Fig. 12 shows that decreasing n_e will result in decreasing optical depth of each element. Fig. 13 shows how decreasing relative hydrogen abundance and increasing relative helium abundance affects the optical depth of other heavier elements. When hydrogen is more abundant, the optical depth plot looks like Fig. 2 (H–rich). But, as hydrogen becomes less abundant (helium is more abundant), the plot becomes looking more like Fig. 4 (He–rich). Notice emergence of O II and O III lines.

Fig 10

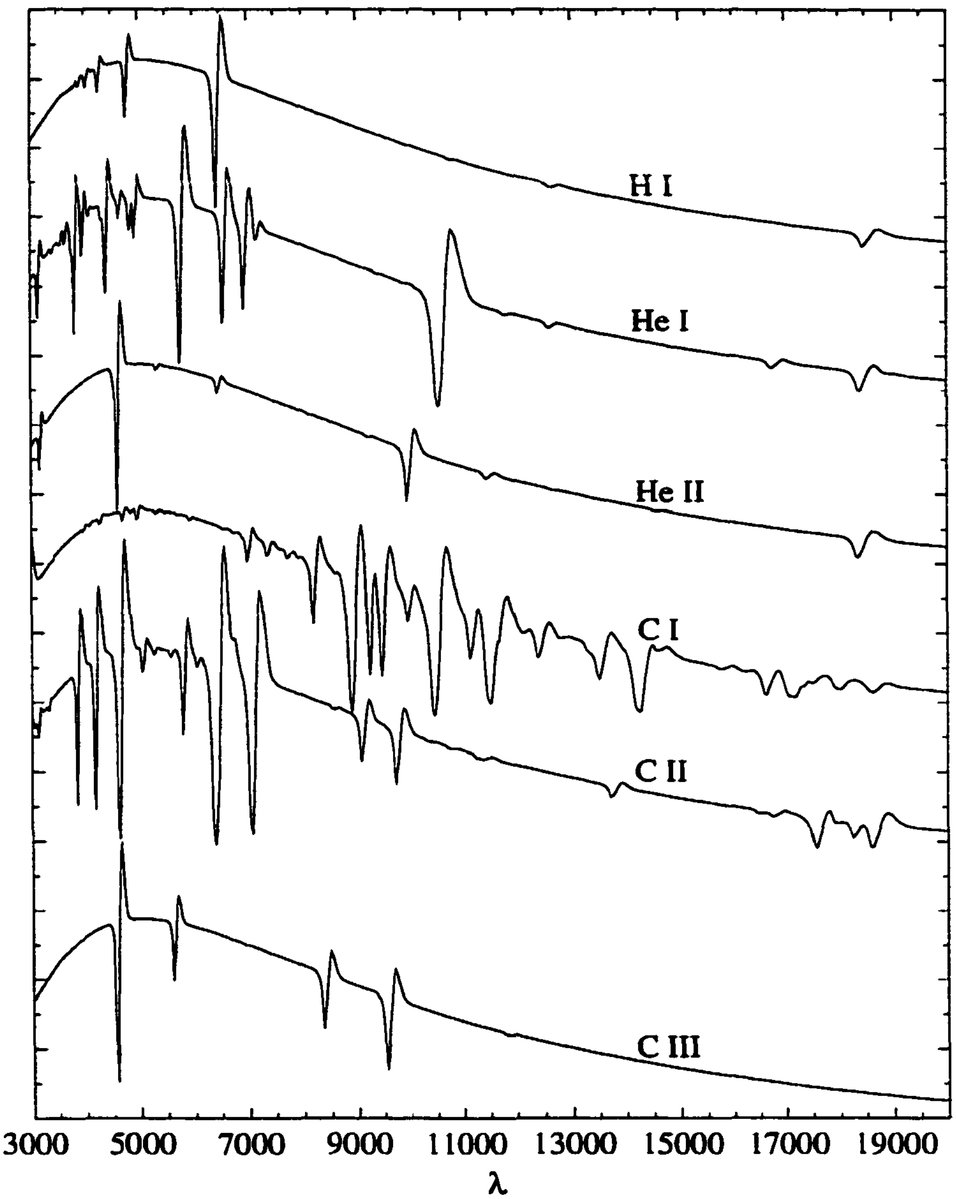

Figure 2.10: A synthetic spectrum is shown for each ion that can be regarded as a candidate for producing identifiable features in the photospheric–phase spectra of supernovae.

Fig 10.2

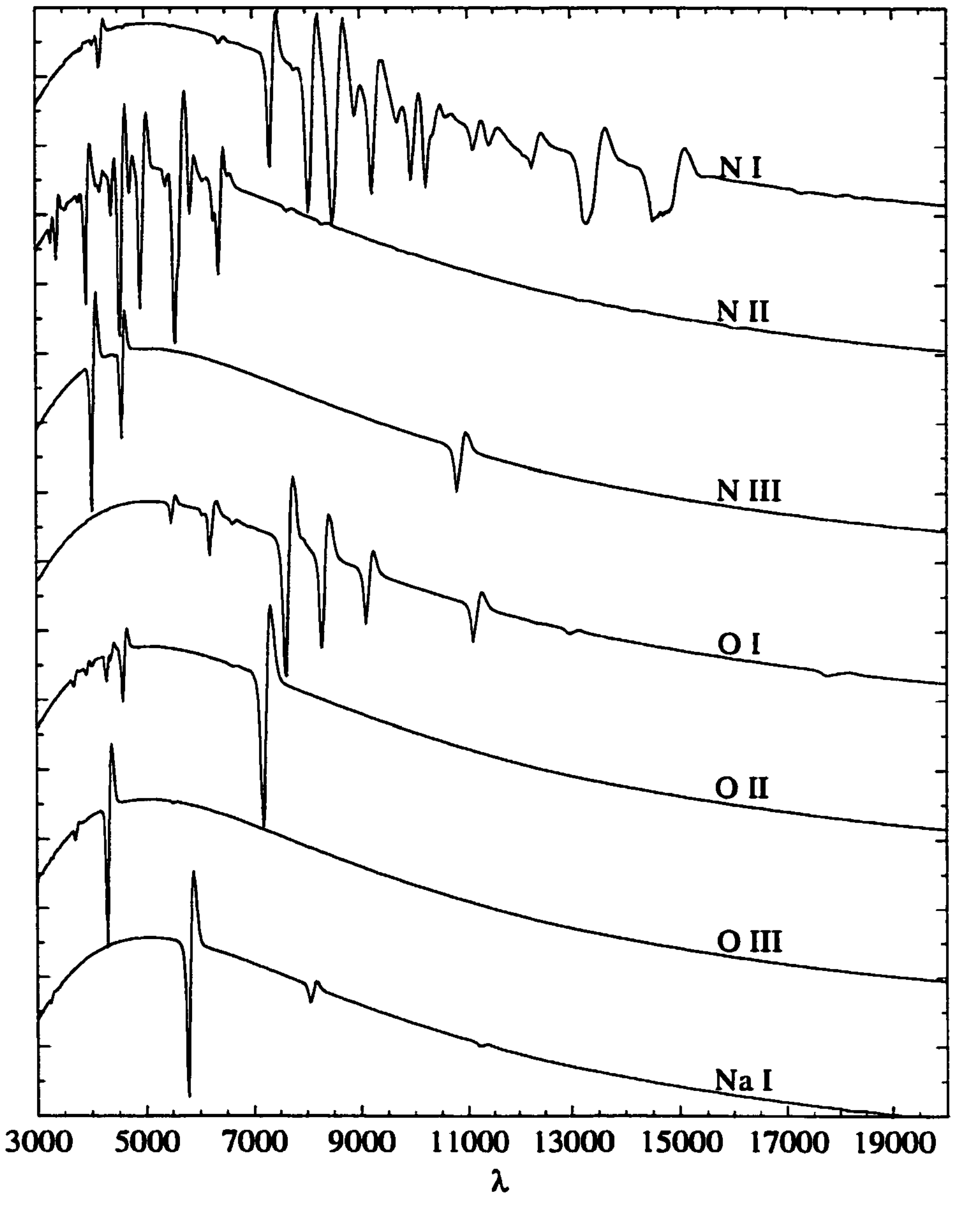

N I
N II
N III
O I
O II
O III
Na I
3000
5000
7000
9000
11000
13000
15000
17000
19000
λ

Fig 10.3

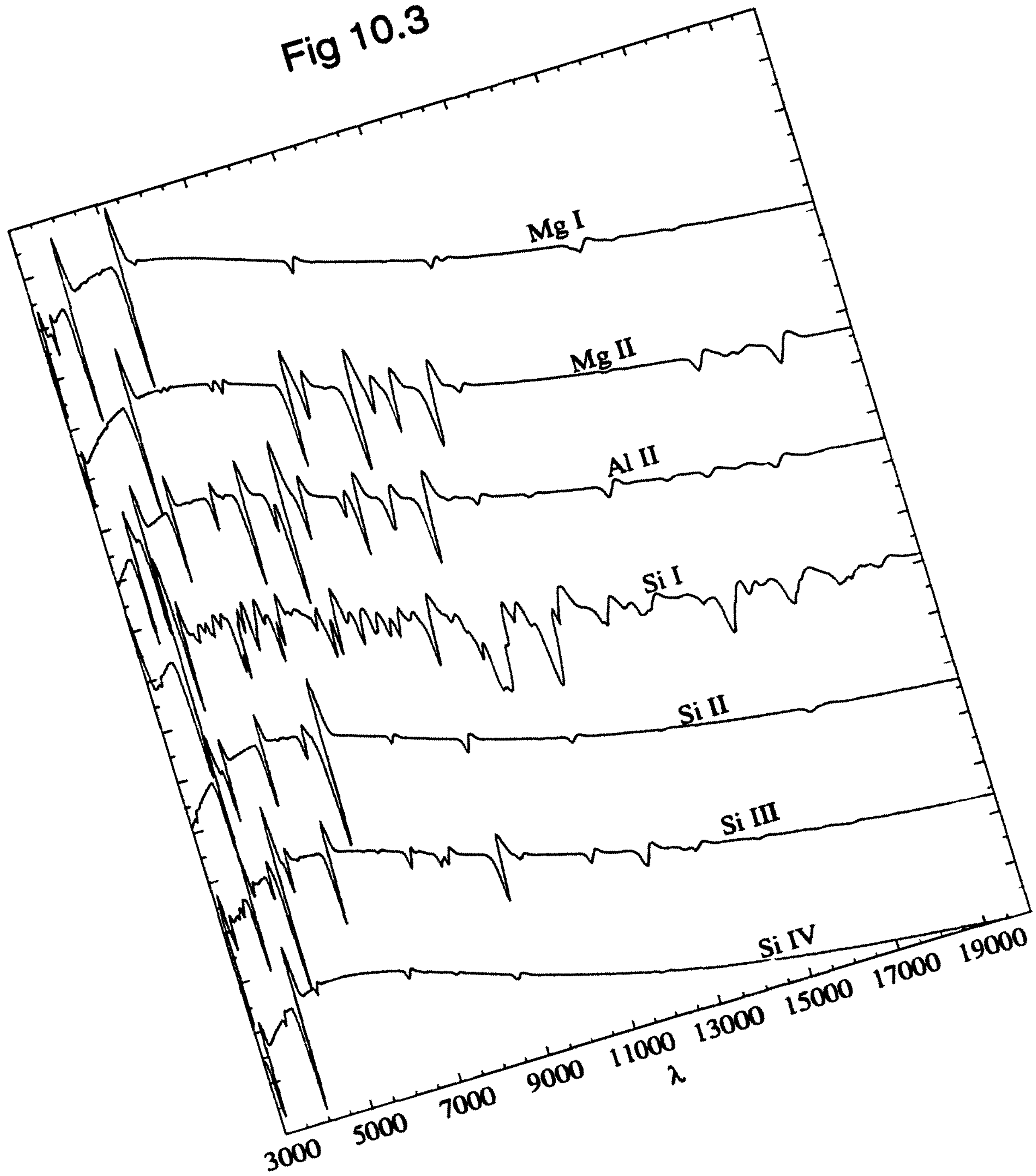

Mg I
Mg II
Al II
Si I
Si II
Si III
Si IV
3000
5000
7000
9000
11000
13000
15000
17000
19000
λ

Fig 10.4

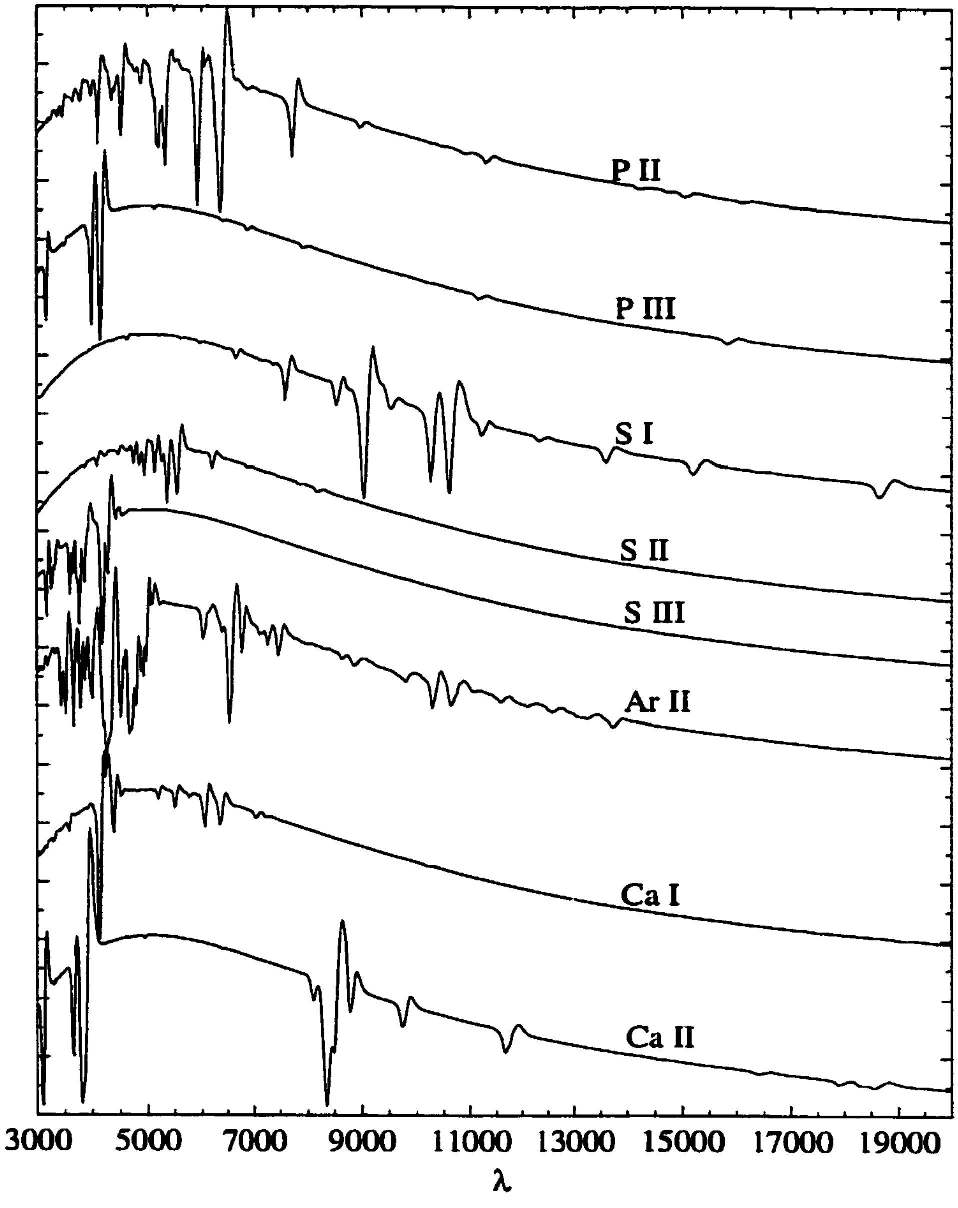
P II
P III
S I
S II
S III
Ar II
Ca I
Ca II
3000
5000
7000
9000
11000
13000
15000
17000
19000
λ

Fig 10.5

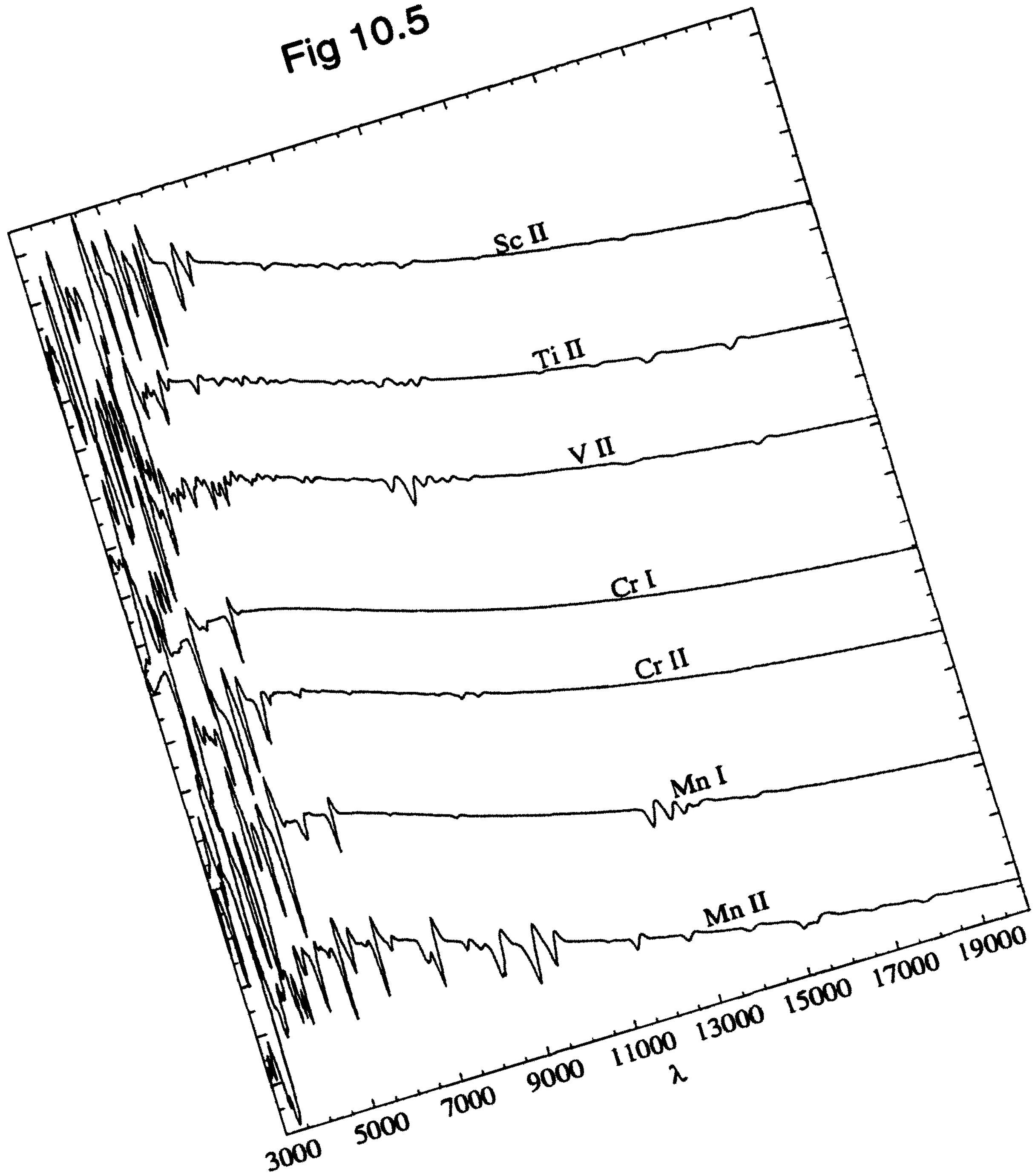
Sc II
Ti II
V II
Cr I
Cr II
Mn I
Mn II
3000
5000
7000
9000
11000
13000
15000
17000
19000
λ

Fig 10.6

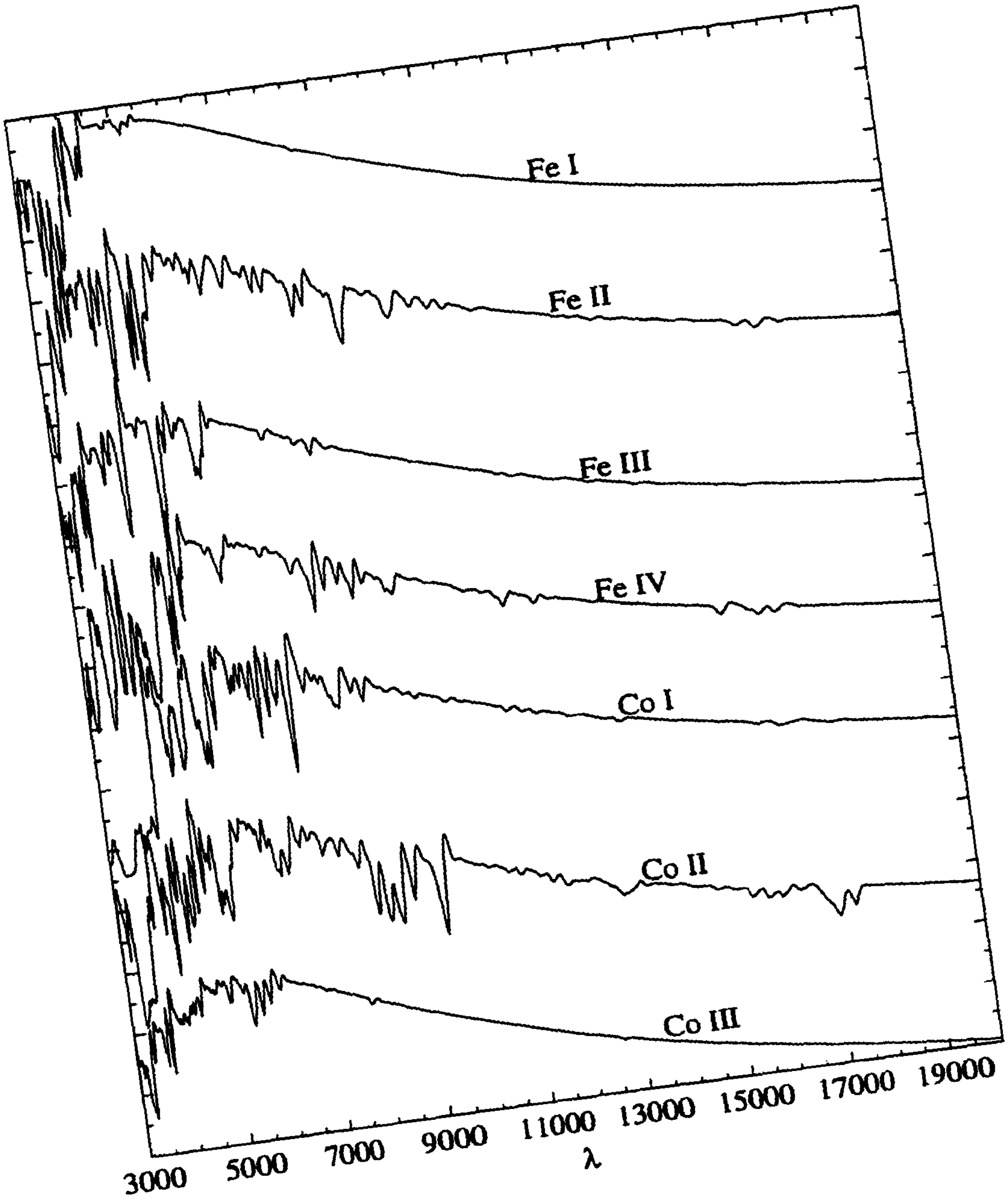

Fe I
Fe II
Fe III
Fe IV
Co I
Co II
Co III
3000
5000
7000
9000
11000
13000
15000
17000
19000
λ

Fig 10.7

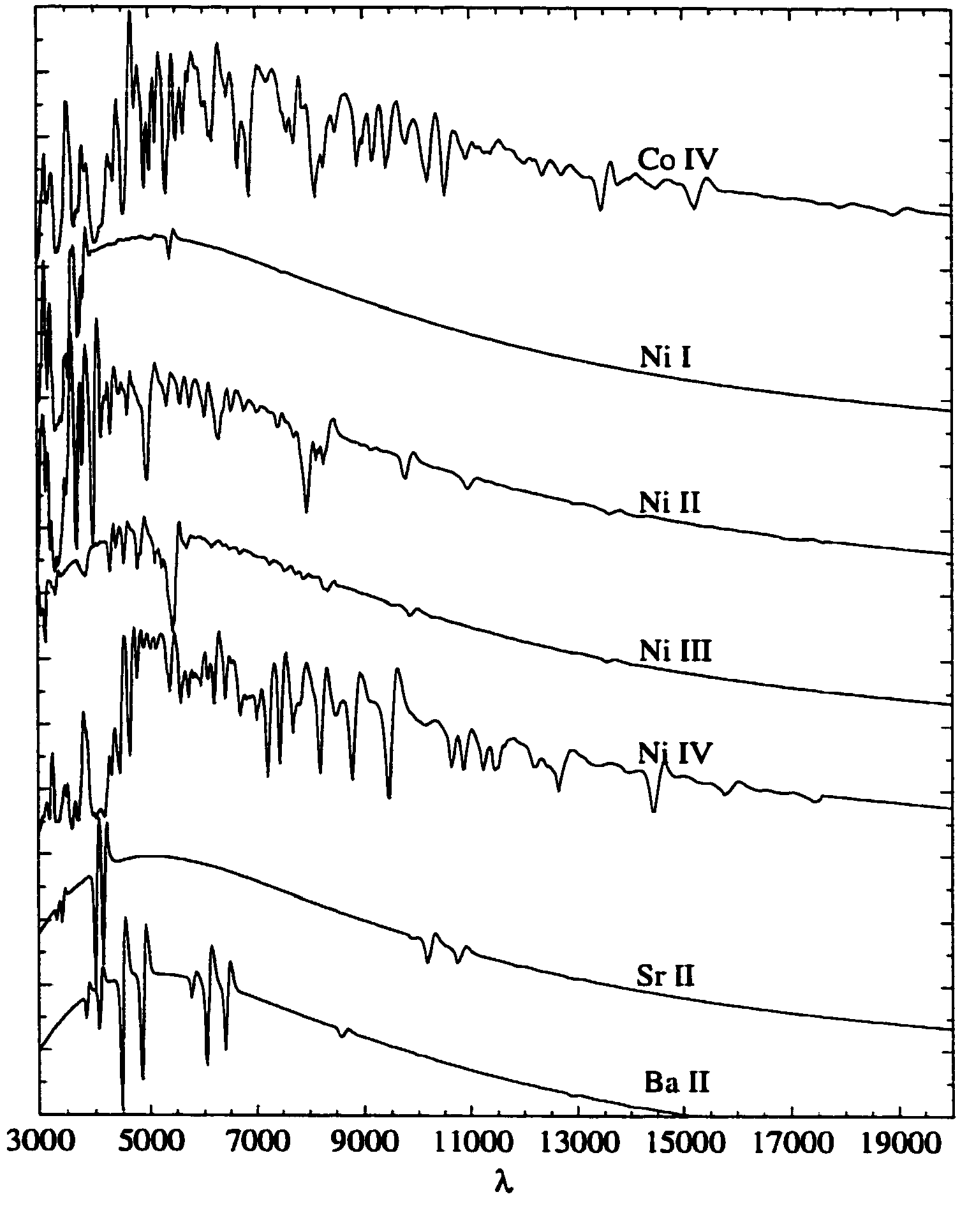

Co IV
Ni I
Ni II
Ni III
Ni IV
Sr II
Ba II
3000
5000
7000
9000
11000
13000
15000
17000
19000
λ

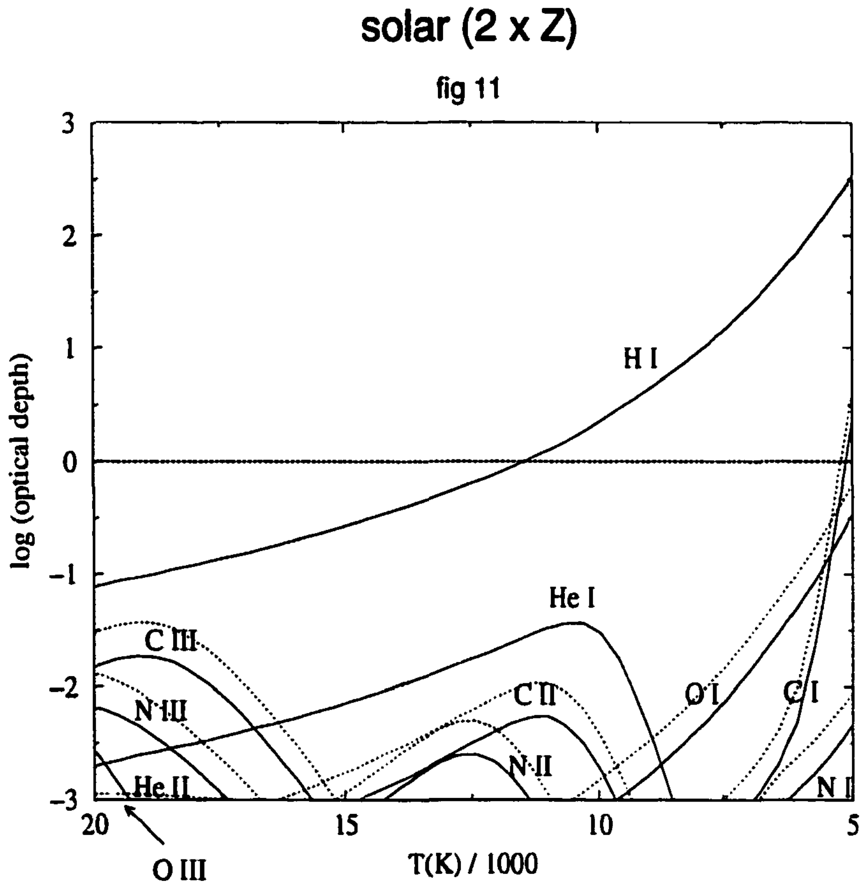

Figure 2.11: Like the first panel in Fig. 2 (solid line) with $\log(n_e) = 9.6$ and the abundance of metal (elements heavier than helium) is increased by a factor of 2 (dotted line).

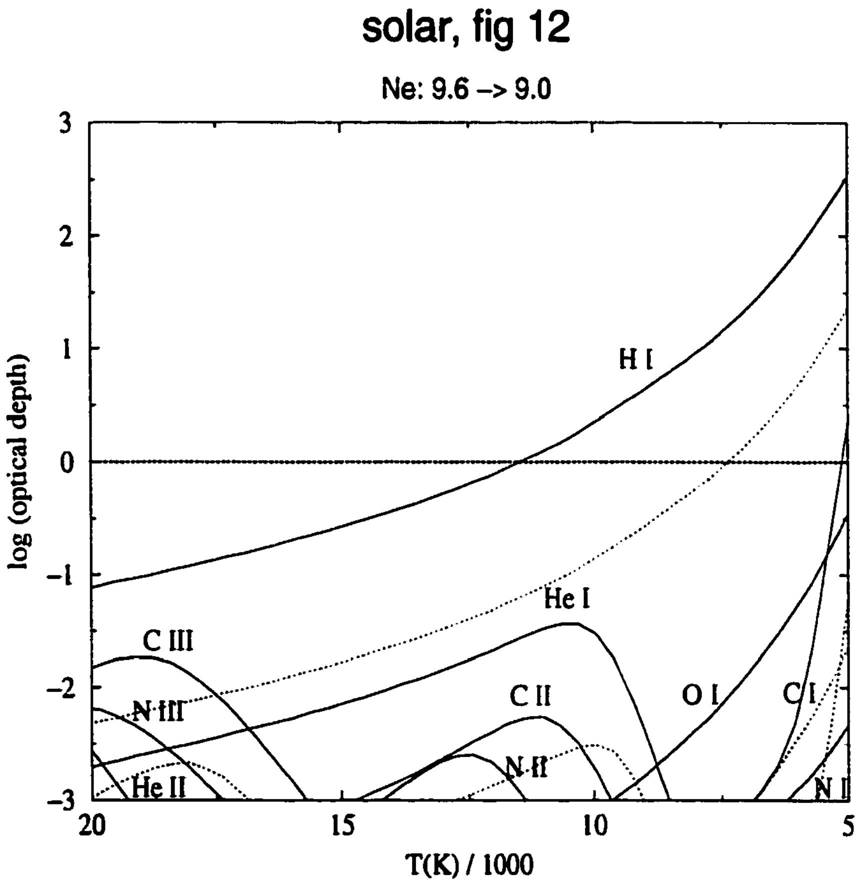

Figure 2.12: Like the first panel in Fig. 2, but in the cases of $\log(n_e)$ is 9.6 (solid line) and 9.0 (dotted line).

Fig 13

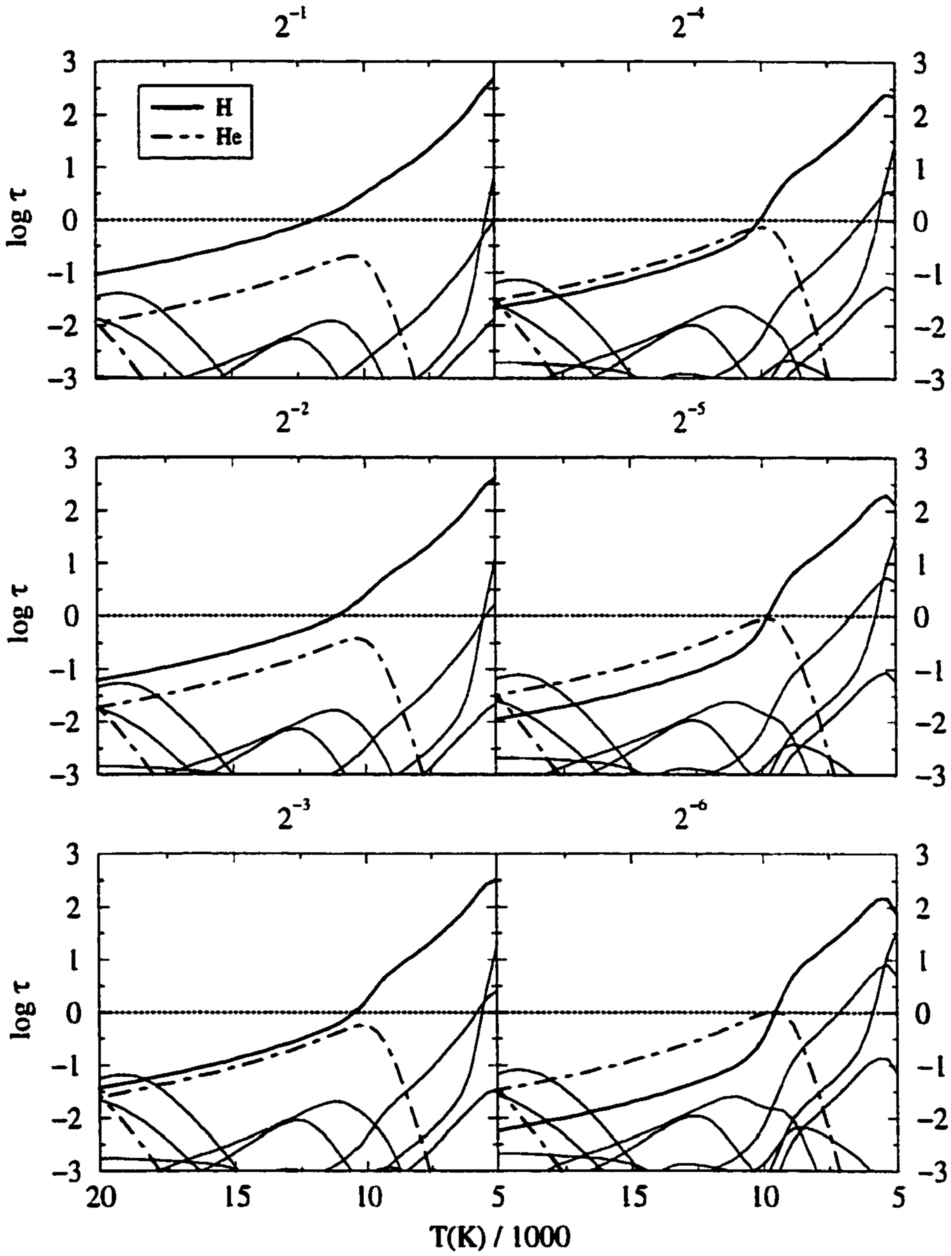

Figure 2.13: Like the first panel in Fig. 2, but relative hydrogen abundance is slowly decreased (by a factor of 2 each time) while relative helium abundance is slowly increased.

Chapter 3

Ion Signatures in Supernova Spectra II: Ultraviolet (UV) and Infrared (IR)

In this chapter, we shall present the optical depth plots for UV and IR reference lines. Just like the previous chapter, we shall consider six different compositions that may be seen in supernovae. To date, the amount of the observed UV and IR supernova spectra is very limited. But, in the near future, much more observed data shall be obtained. And, it is very important to analyze the UV and IR spectra to advance the knowledge about supernovae. In particular, understanding the UV spectra shall be very important to use the high redshift (high–z) SNe Ia for cosmology. In the optical spectra of these high–z SNe Ia, we shall see the spectral features normally seen in the UV spectra of the low redshift SNe Ia due to their very large value of the redshift. Before these high–z SNe Ia may be used for any cosmological application, their spectra must be understood well. Therefore, we shall present the optical depth plots for UV and IR reference lines here. These plots shall be very useful to understand the UV and IR spectra of all types of supernovae.

ion	λ	log(gf)	E_i (cm^{-1})	χ (eV), eV = cm^{-1}/8066	
H I	1215.7	-0.08	0.0	0.00	1
He I	2945.1	-1.95	159856.1	19.82	—
He II	1640.5	0.40	329185.1	40.81	—
C I	945.6	0.13	43.4	0.01	12345
C II	1037.0	-0.35	63.4	0.01	12345
C III	977.0	-0.16	0.0	0.00	12345
C IV	1548.2	-0.42	0.0	0.00	12345
N I	1199.6	-0.29	0.0	0.00	123
N II	916.7	-0.26	130.8	0.02	123
N III	991.6	-0.35	174.4	0.02	123
N IV	923.2	-0.07	67416.3	8.36	123
O I	1302.2	-0.62	0.0	0.00	12345
O II	1075.0	-5.07	26810.7	3.32	234
O III	2496.8	-0.14	20273.3	2.51	12345
O IV	1401.2	-5.66	385.9	0.05	34
F I	954.8	-0.51	0.0	0.00	123
F II	1747.4	-1.16	182864.4	22.67	—
F III	2600.1	0.59	349266.2	43.30	—
F IV	2042.5	-0.22	25234.4	3.13	—
Ne I	2983.5	-2.30	134041.8	16.62	—
Ne II	2956.6	-0.18	219130.8	27.17	—
Ne III	1814.6	-8.96	642.9	0.08	—
Ne IV	1601.5	-8.68	0.0	0.00	—
Na I	2852.8	-2.48	0.0	0.00	—
Na II	2842.6	-0.07	264924.3	32.84	—
Na III	2231.0	0.35	366154.4	45.39	—
Na IV	1522.7	-8.58	1106.6	0.14	—
Mg I	2852.1	0.27	0.0	0.00	12345
Mg II	2795.5	0.10	0.0	0.00	12345
Mg III	2065.6	0.29	425640.3	52.77	—
Mg IV	1683.0	0.30	543720.4	67.41	—
Al I	1936.5	0.60	112.1	0.01	123
Al II	1670.8	0.32	0.0	0.00	123
Al III	1854.7	0.06	0.0	0.00	123
Al IV	1557.3	0.26	616644.2	76.45	—
Si I	1258.8	0.35	223.2	0.03	12345
Si II	1194.5	0.82	287.2	0.04	12345
Si III	1206.5	0.23	0.0	0.00	12345
Si IV	1393.8	0.03	0.0	0.00	12345
P I	1679.7	0.12	0.0	0.00	12345
P II	1536.4	1.28	164.9	0.02	12345
P III	918.7	0.54	559.1	0.07	12345
P IV	950.7	0.27	0.0	0.00	12345
S I	1425.0	-0.12	0.0	0.00	12345
S II	947.0	-0.23	0.0	0.00	12345
S III	1201.0	-1.03	832.5	0.10	12345
S IV	1073.0	-0.83	951.1	0.12	12345

ion	λ	log(gf)	E_i (cm^{-1})	χ (eV), eV = cm^{-1}/8066	
Cl I	1167.1	-0.09	0.0	0.00	12345
Cl II	961.5	0.39	11653.6	1.44	12345
Cl III	1015.0	0.05	0.0	0.00	12345
Cl IV	985.0	0.36	1341.0	0.17	12345
Ar I	1048.2	-0.59	0.0	0.00	12345
Ar II	932.1	0.12	1431.6	0.18	12345
Ar III	1002.1	-2.42	14010.0	1.74	2345
Ar IV	1037.9	-3.11	21219.5	2.63	345
K I	2992.1	-4.54	0.0	0.00	—
K III	2993.3	0.22	207421.9	25.72	—
K IV	1029.7	-3.58	38546.3	4.78	—
Ca I	2050.4	-1.15	0.0	0.00	25
Ca II	1840.1	0.09	13710.9	1.70	12345
Ca III	2123.0	0.73	277022.4	34.34	—
Ca IV	2289.4	-2.07	335122.0	41.55	—
Sc I	1744.7	-0.22	168.3	0.02	—
Sc II	2553.1	0.06	177.8	0.02	12345
Sc III	1603.1	-0.29	197.6	0.02	2345
Sc IV	931.4	-1.00	271055.4	33.60	—
Ti I	2984.2	-0.12	170.1	0.02	—
Ti II	1906.5	0.16	393.4	0.05	12345
Ti III	1293.2	-0.08	420.4	0.05	12345
Ti IV	2068.2	0.03	80388.9	9.97	45
V I	2387.3	0.68	2112.3	0.26	—
V II	2924.9	0.47	3162.8	0.39	12345
V III	1149.9	0.07	583.8	0.07	2345
V IV	1939.1	0.46	96798.0	12.00	45
Cr I	2095.6	-0.55	0.0	0.00	25
Cr II	2056.3	0.03	0.0	0.00	12345
Cr III	924.0	-0.15	576.1	0.07	12345
Cr IV	1840.1	0.58	105105.7	13.03	45
Mn I	2795.6	0.57	0.0	0.00	12345
Mn II	2576.9	0.43	0.0	0.00	12345
Mn III	917.8	0.20	26824.4	3.33	12345
Mn IV	1742.1	0.61	112882.8	13.99	5
Fe I	2484.0	0.73	0.0	0.00	123456
Fe II	2382.8	0.56	0.0	0.00	123456
Fe III	1122.5	-0.15	0.0	0.00	123456
Fe IV	1631.1	0.57	128967.7	15.99	123456
Co I	2408.0	0.78	0.0	0.00	1246
Co II	2286.9	0.60	3350.6	0.42	123456
Co III	939.1	-0.05	0.0	0.00	123456
Co IV	1502.2	0.46	90554.4	11.23	46
Ni I	2320.7	0.74	0.0	0.00	123456
Ni II	2217.2	0.54	8393.9	1.04	123456
Ni III	979.6	-0.44	16661.6	2.07	123456
Ni IV	1398.2	0.58	110410.6	13.69	23456

ion	λ	log(gf)	E_i (cm^{-1})	χ (eV), eV = cm^{-1}/8066	
Sr I	2275.2	-1.50	0.0	0.00	—
Sr II	2165.9	0.40	14836.2	1.84	123
Ba I	2596.6	-1.45	0.0	0.00	—
Ba II	2304.3	1.20	4873.9	0.60	123

Table 3.1: Ultraviolet Reference Lines

ion	λ	log(gf)	E_i (cm^{-1})	χ (eV), eV = cm^{-1}/8066	
H I	18751.0	1.18	97492.3	12.09	1
He I	10830.3	-0.05	159856.1	19.82	12
He II	10123.6	1.52	411477.9	51.01	12
C I	10691.2	0.35	60393.1	7.49	12345
C II	18896.6	0.26	157234.1	19.49	1234
C III	11984.5	0.26	309457.2	38.37	1234
C IV	20796.1	-0.65	320081.7	39.68	1234
N I	14761.1	0.30	88107.3	10.92	123
N II	16260.6	0.45	196711.5	24.39	123
N III	10981.3	-1.32	221302.2	27.44	123
N IV	17746.5	-0.02	498045.5	61.75	—
O I	11286.9	0.50	88631.1	10.99	12345
O II	14013.5	0.53	238893.0	29.62	1234
O III	10324.6	0.38	357117.0	44.27	1234
O IV	13421.6	0.20	539368.0	66.87	—
F I	11560.3	0.12	116987.4	14.50	—
F II	12021.1	0.48	235150.6	29.15	—
F III	10158.0	-0.15	431432.3	53.49	—
Ne I	11180.6	0.06	149657.0	18.55	1234
Ne II	12868.6	-1.47	246394.1	30.55	3
Ne III	10841.0	-2.42	379834.0	47.09	—
Ne IV	11735.7	0.14	634413.0	78.65	—
Na I	11403.8	-0.18	16973.4	2.10	1234
Mg I	11828.2	-0.29	35051.3	4.35	12345
Mg II	10914.2	0.02	71490.2	8.86	12345
Mg III	21260.8	-1.31	582074.4	72.16	—
Al I	13123.4	0.27	25347.8	3.14	123
Al II	10079.1	-0.05	95549.4	11.85	123
Al III	12766.5	0.35	170637.3	21.16	123
Si I	12031.5	0.44	39955.1	4.95	12345
Si II	16906.8	0.35	97972.1	12.15	12345
Si III	12499.7	0.50	201599.5	24.99	12345
Si IV	24265.9	-0.15	250008.0	31.00	12345
P I	10584.5	0.48	56339.7	6.98	12345
P II	21253.5	1.41	105549.7	13.09	12345
P III	11344.0	0.42	176042.9	21.83	4
P IV	12861.4	-0.35	309111.4	38.32	4
S I	10824.1	-6.00	0.0	0.00	12345
S II	14505.3	-0.22	133814.8	16.59	12345
Cl I	15874.0	0.54	83894.0	10.40	12345
Cl II	11296.4	-1.56	119811.2	14.85	24
Cl III	10213.4	-1.05	196155.8	24.32	4
Ar I	13722.3	0.54	105462.8	13.07	12345
Ar II	10470.0	-0.38	149179.2	18.49	12345
Ar III	22602.2	-2.96	204727.5	25.38	45
K I	11772.8	0.51	13042.9	1.62	12345
K III	20167.0	-1.11	241667.0	29.96	—

ion	λ	log(gf)	E_i (cm^{-1})	χ (eV), eV = cm^{-1}/8066	
Ca I	19776.8	-0.83	20371.0	2.53	12345
Ca II	11839.0	0.30	52166.9	6.47	12345
Ca III	10220.1	0.71	367026.7	45.50	5
Sc I	22058.2	-0.76	11677.4	1.45	1245
Sc II	11142.0	0.61	57743.9	7.16	12345
Sc III	13467.9	0.24	148150.1	18.37	—
Sc IV	15239.7	-3.15	442046.0	54.80	—
Ti I	10399.6	-1.54	6843.0	0.85	12345
Ti II	10694.2	0.75	62595.0	7.76	12345
Ti III	10809.7	0.35	159269.5	19.75	45
Ti IV	11069.6	0.20	265847.4	32.96	45
V I	13791.5	-0.94	15063.0	1.87	1245
V II	10187.3	-1.39	30613.9	3.80	12345
V III	12164.9	0.43	174223.7	21.60	45
Cr I	11613.7	-0.01	26787.5	3.32	12345
Cr II	15369.7	0.40	87137.1	10.80	12345
Cr III	12983.8	-2.04	105626.9	13.10	2345
Cr IV	16665.6	-5.62	155354.4	19.26	—
Mn I	12903.3	-1.06	17052.3	2.11	12345
Mn II	15412.7	0.24	79569.3	9.86	12345
Mn III	20585.3	-3.22	116622.4	14.46	5
Fe I	11976.3	-1.48	17550.2	2.18	123456
Fe II	10504.4	-2.00	44753.8	5.55	123456
Fe III	12789.6	0.72	190918.2	23.67	123456
Fe IV	18680.8	-2.62	222840.6	27.63	123456
Co I	11321.4	-1.19	27497.1	3.41	1246
Co II	17776.6	-2.09	40695.6	5.05	123456
Co III	14640.2	-8.47	91715.1	11.37	6
Co IV	15410.2	-3.51	214059.3	26.54	6
Ni I	11199.8	-1.97	22102.3	2.74	123456
Ni II	18780.3	0.24	98822.5	12.25	123456
Ni III	10010.4	-2.50	121802.5	15.10	123456
Ni IV	14673.3	-3.69	179655.0	22.27	456
Sr II	10327.3	-0.35	14836.2	1.84	123
Ba I	14999.9	-0.30	11395.4	1.41	—
Ba II	13058.0	0.34	42355.2	5.25	123

Table 3.2: Infrared Reference Lines

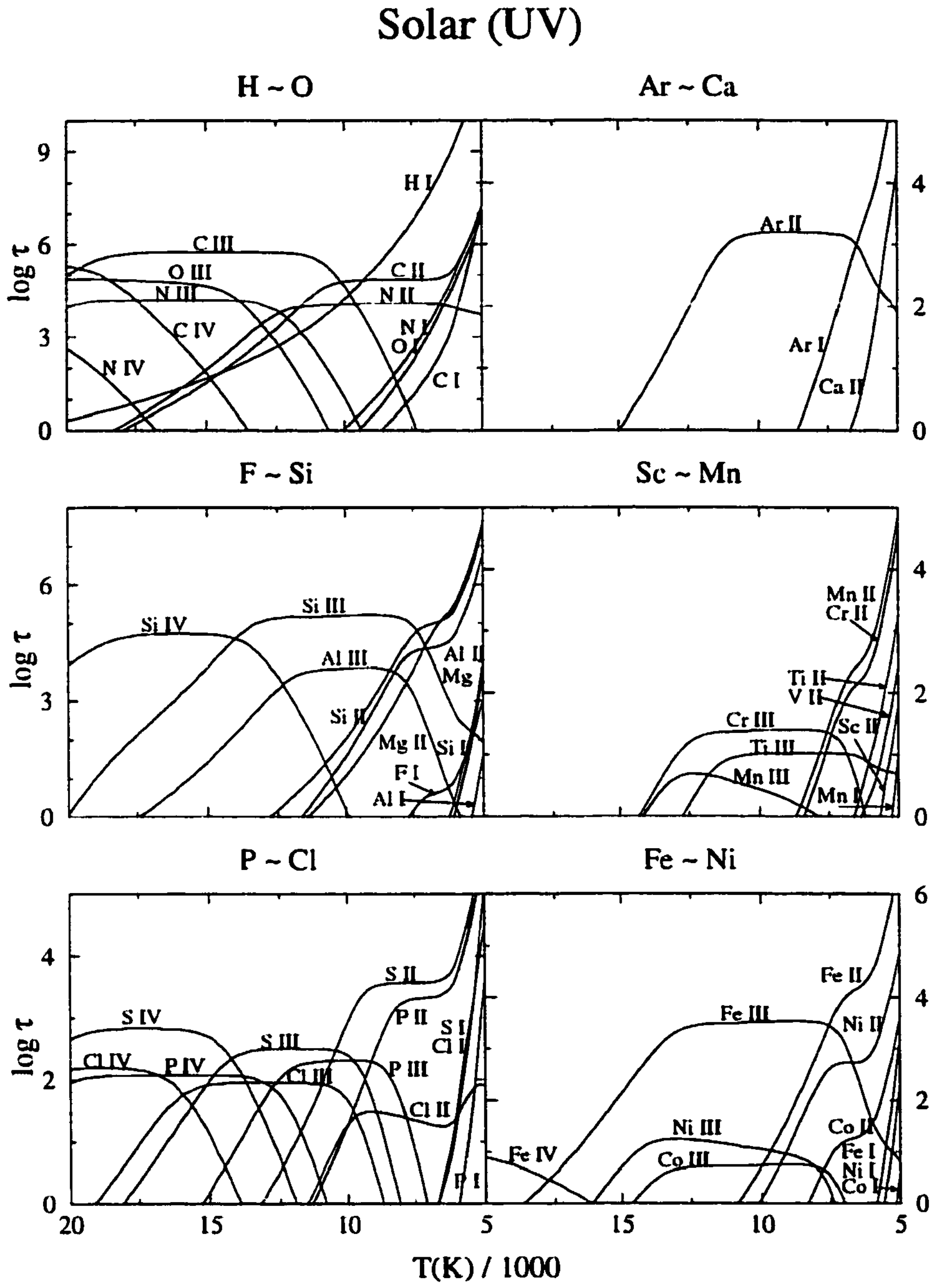

Figure 3.1: The log of the Sobolev LTE optical depth of UV ion reference lines, evaluated at $\tau_{es} = 1$, is plotted against temperature for the hydrogen-rich (solar) composition.

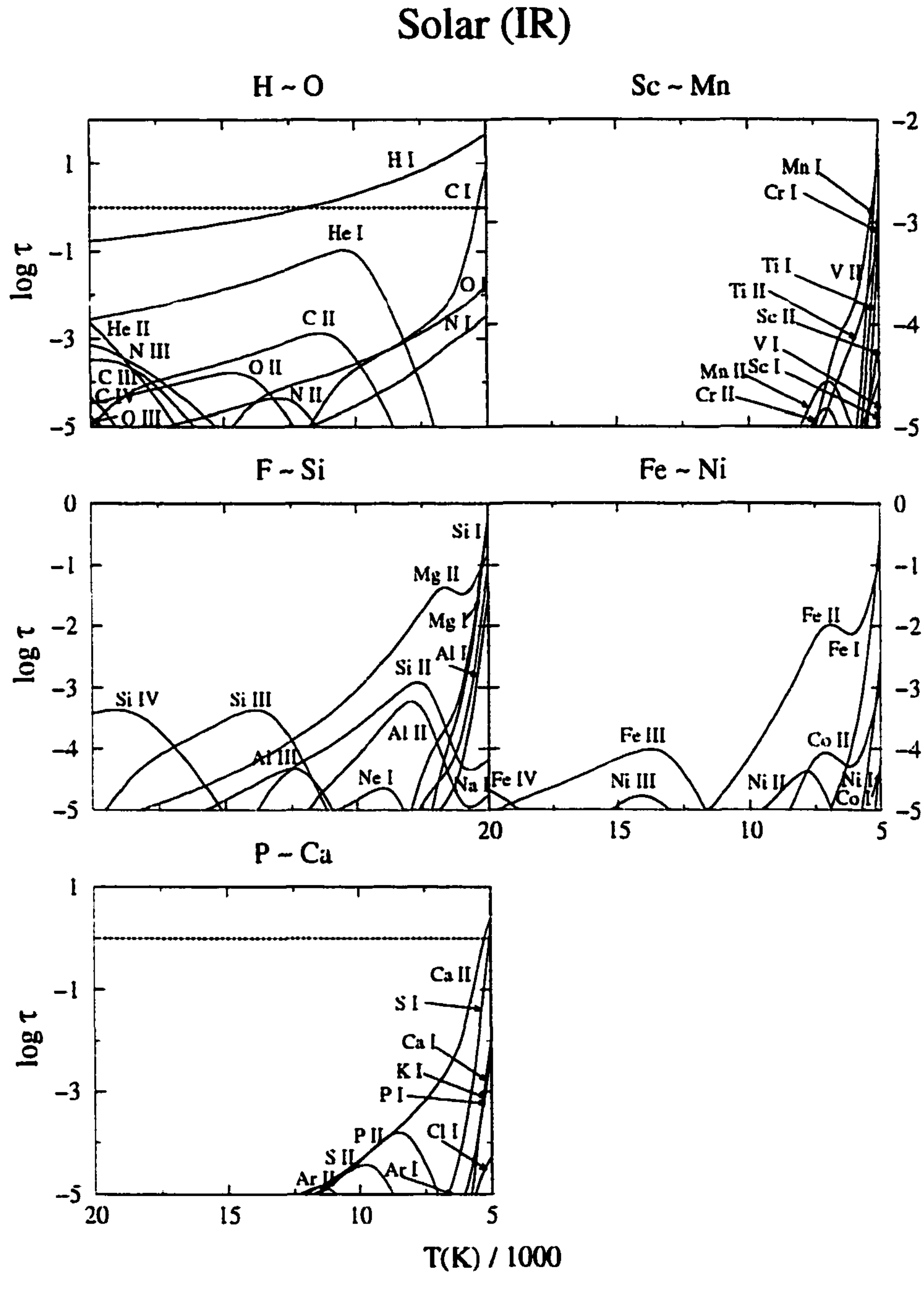

Figure 3.2: The log of the Sobolev LTE optical depth of IR ion reference lines, evaluated at $\tau_{es} = 1$, is plotted against temperature for the hydrogen-rich (solar) composition.

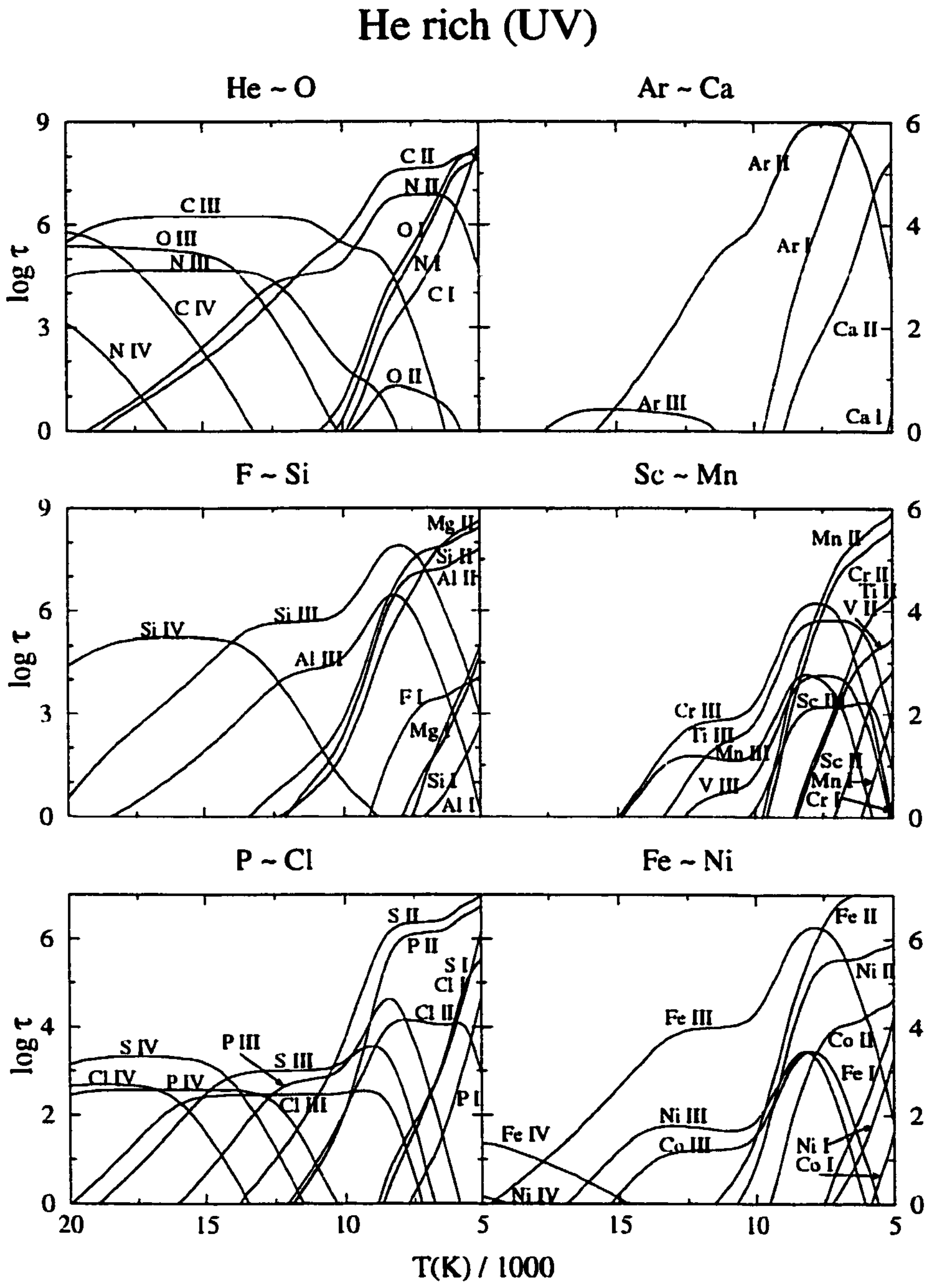

Figure 3.3: The log of the Sobolev LTE optical depth of UV ion reference lines, evaluated at $\tau_{es} = 1$, is plotted against temperature for the helium-rich composition.

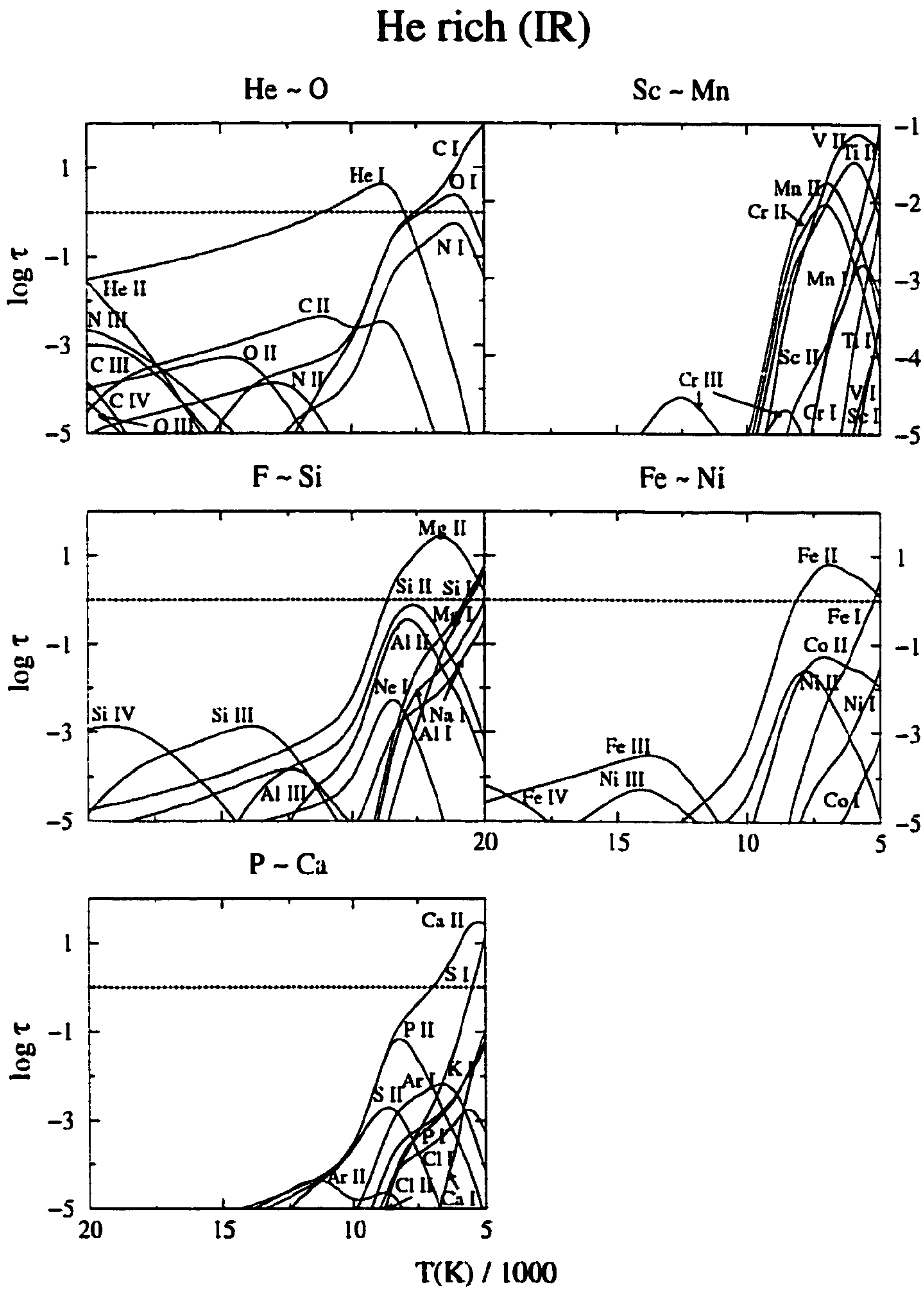

Figure 3.4: The log of the Sobolev LTE optical depth of IR ion reference lines, evaluated at $\tau_{es} = 1$, is plotted against temperature for the helium-rich composition.

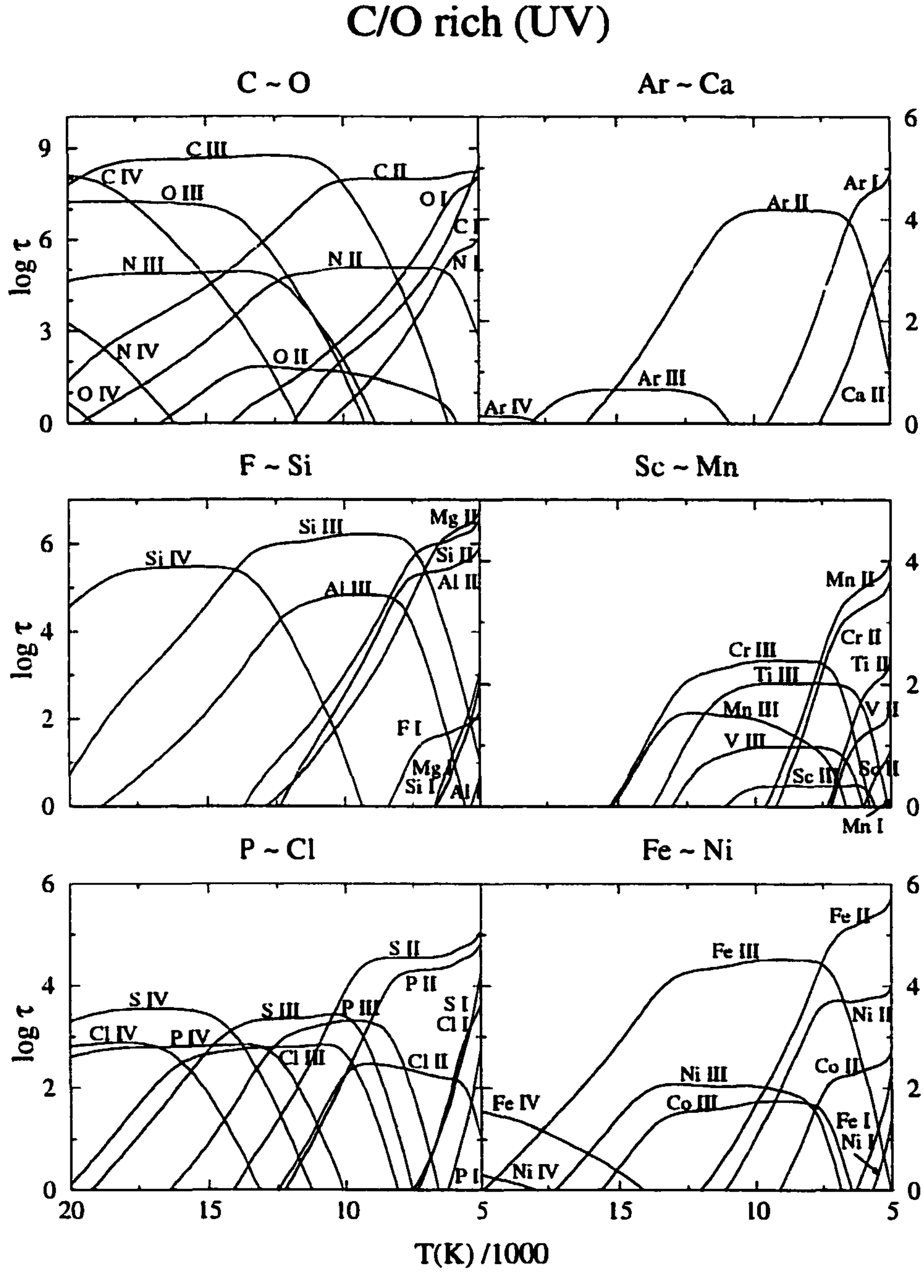

Figure 3.5: The log of the Sobolev LTE optical depth of UV ion reference lines, evaluated at $\tau_{es} = 1$, is plotted against temperature for the C/O-rich composition.

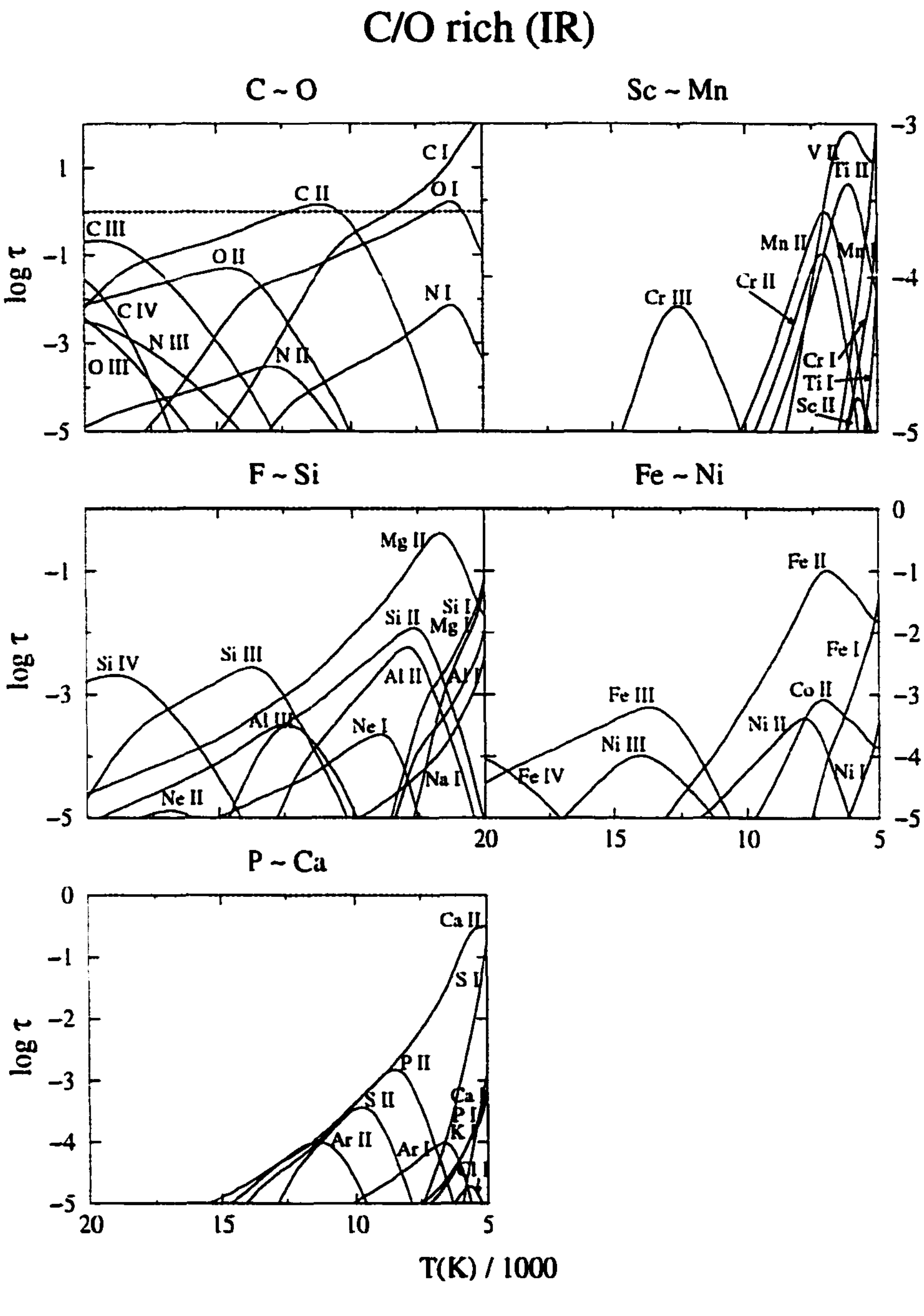

Figure 3.6: The log of the Sobolev LTE optical depth of IR ion reference lines, evaluated at $\tau_{es} = 1$, is plotted against temperature for the C/O–rich composition.

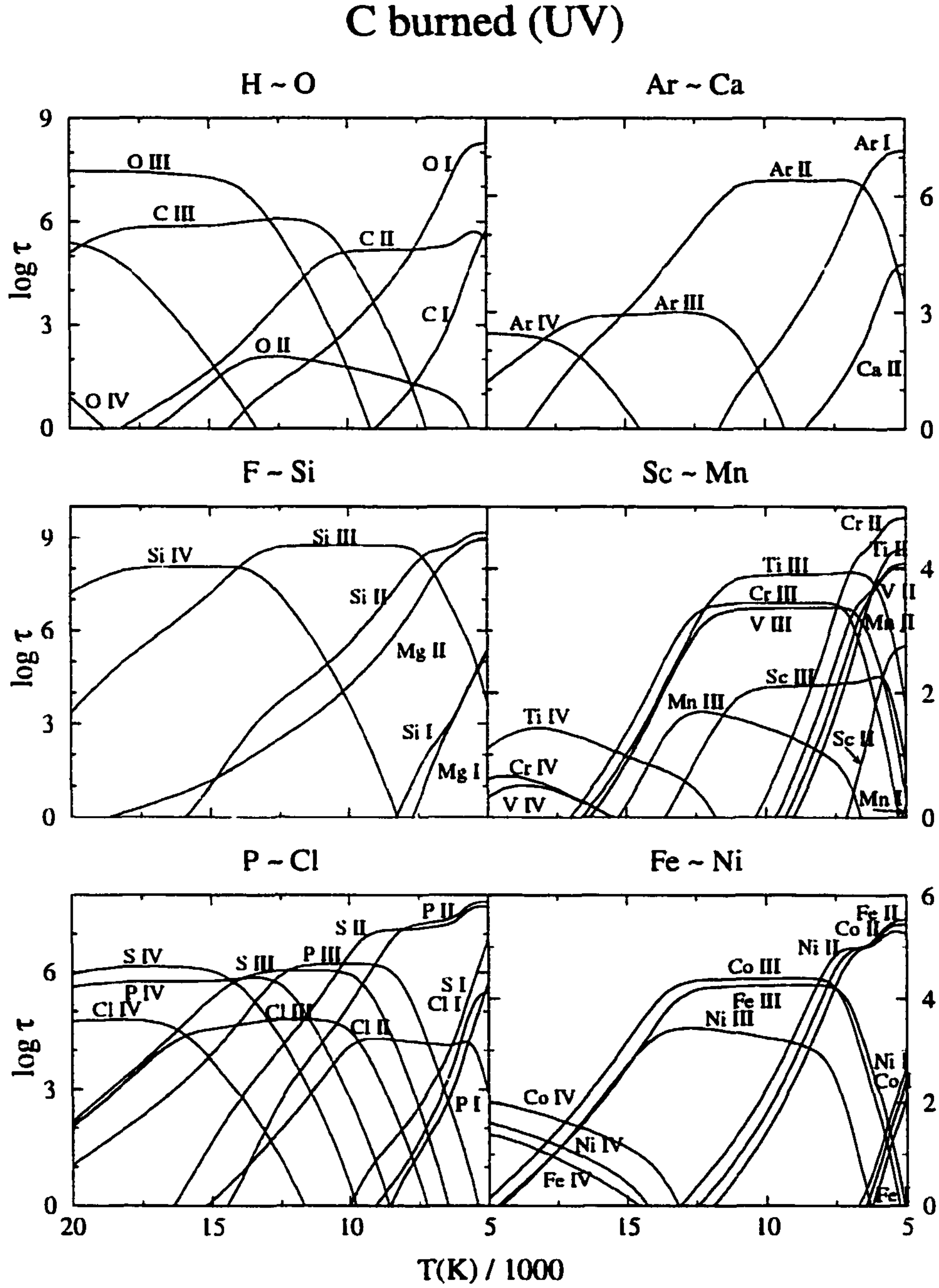

Figure 3.7: The log of the Sobolev LTE optical depth of UV ion reference lines, evaluated at $\tau_{es} = 1$, is plotted against temperature for the carbon–burned composition.

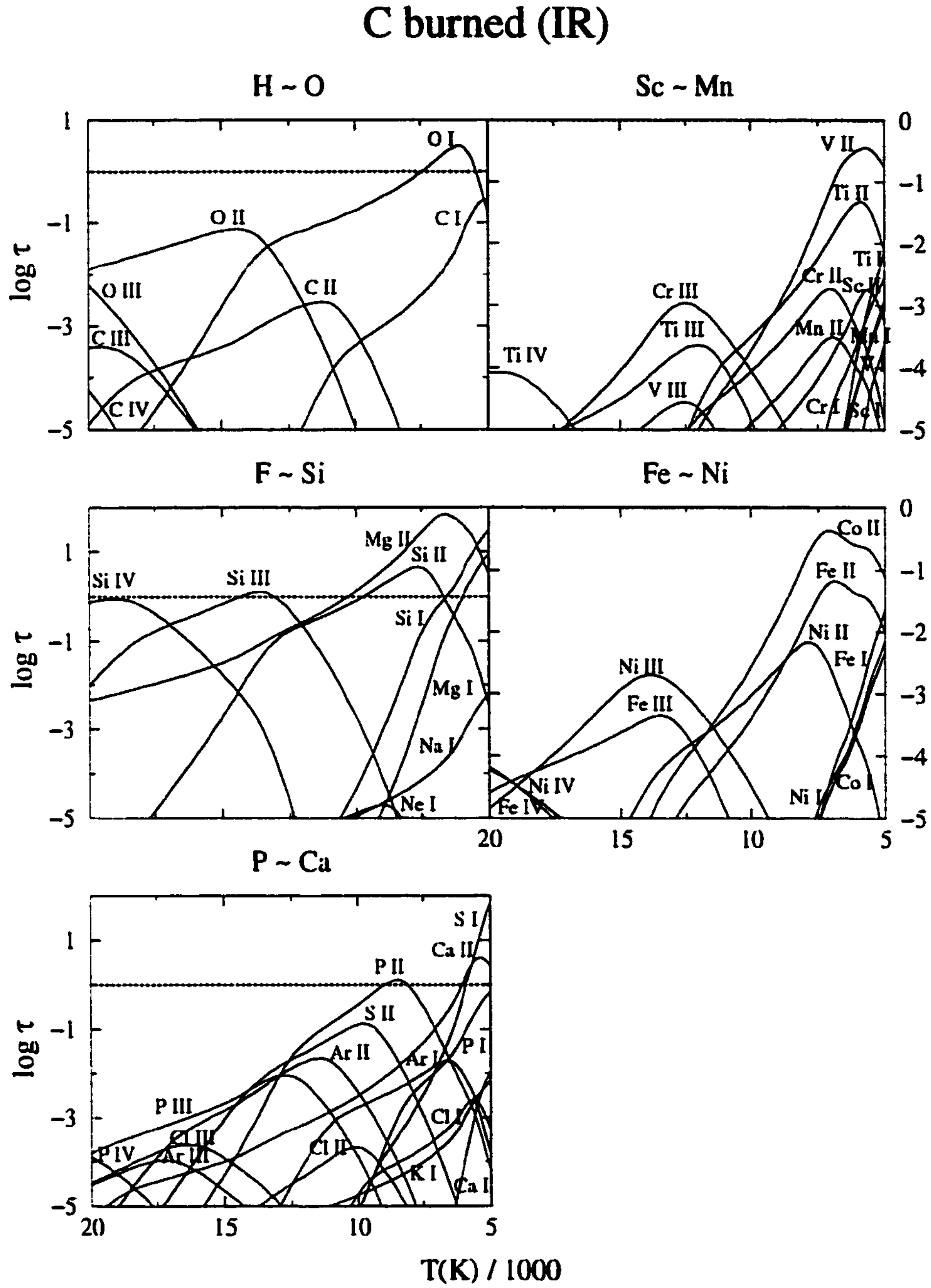

Figure 3.8: The log of the Sobolev LTE optical depth of IR ion reference lines, evaluated at $\tau_{es} = 1$, is plotted against temperature for the carbon–burned composition.

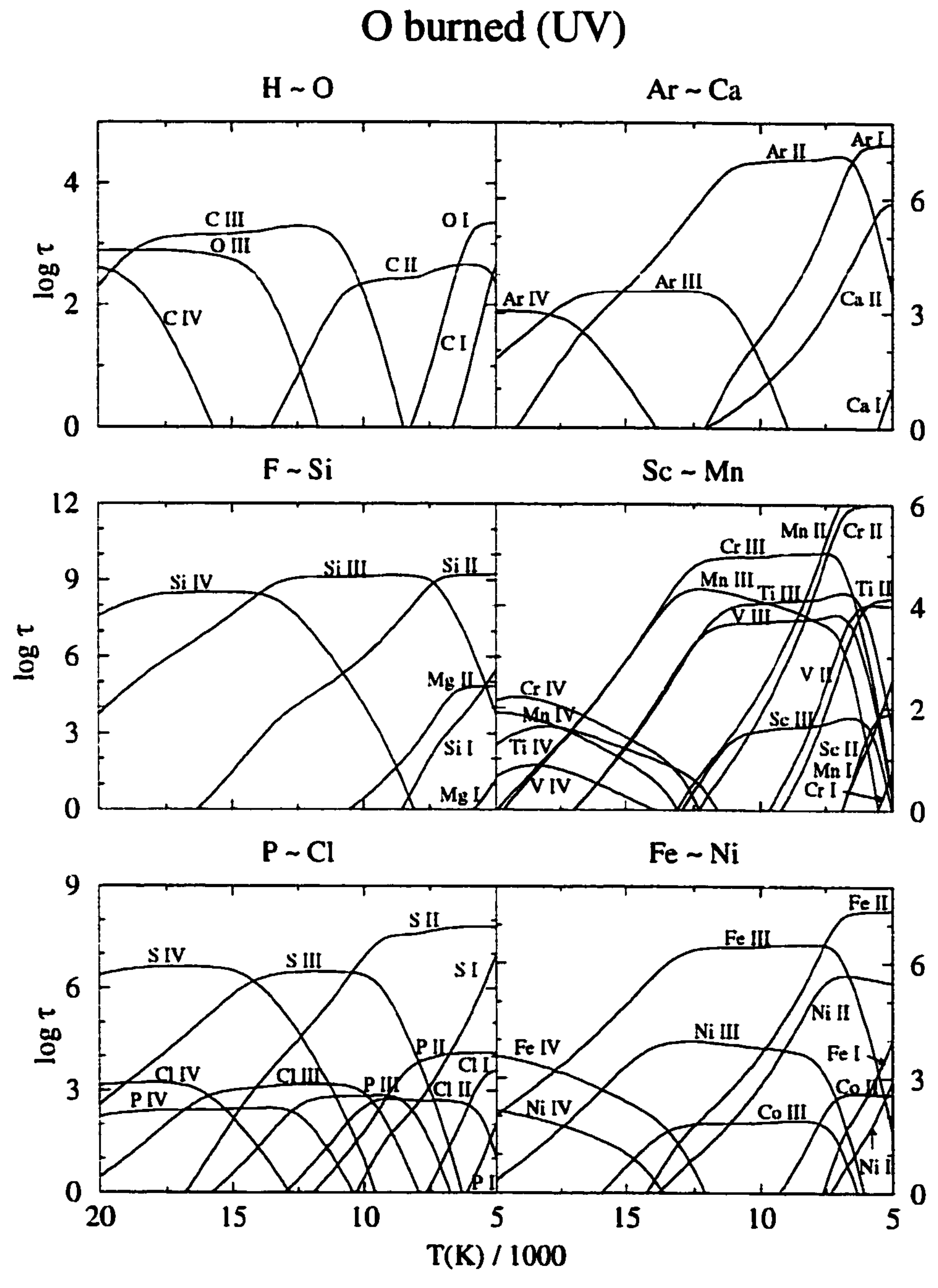

Figure 3.9: The log of the Sobolev LTE optical depth of UV ion reference lines, evaluated at $\tau_{es} = 1$, is plotted against temperature for the oxygen-burned composition.

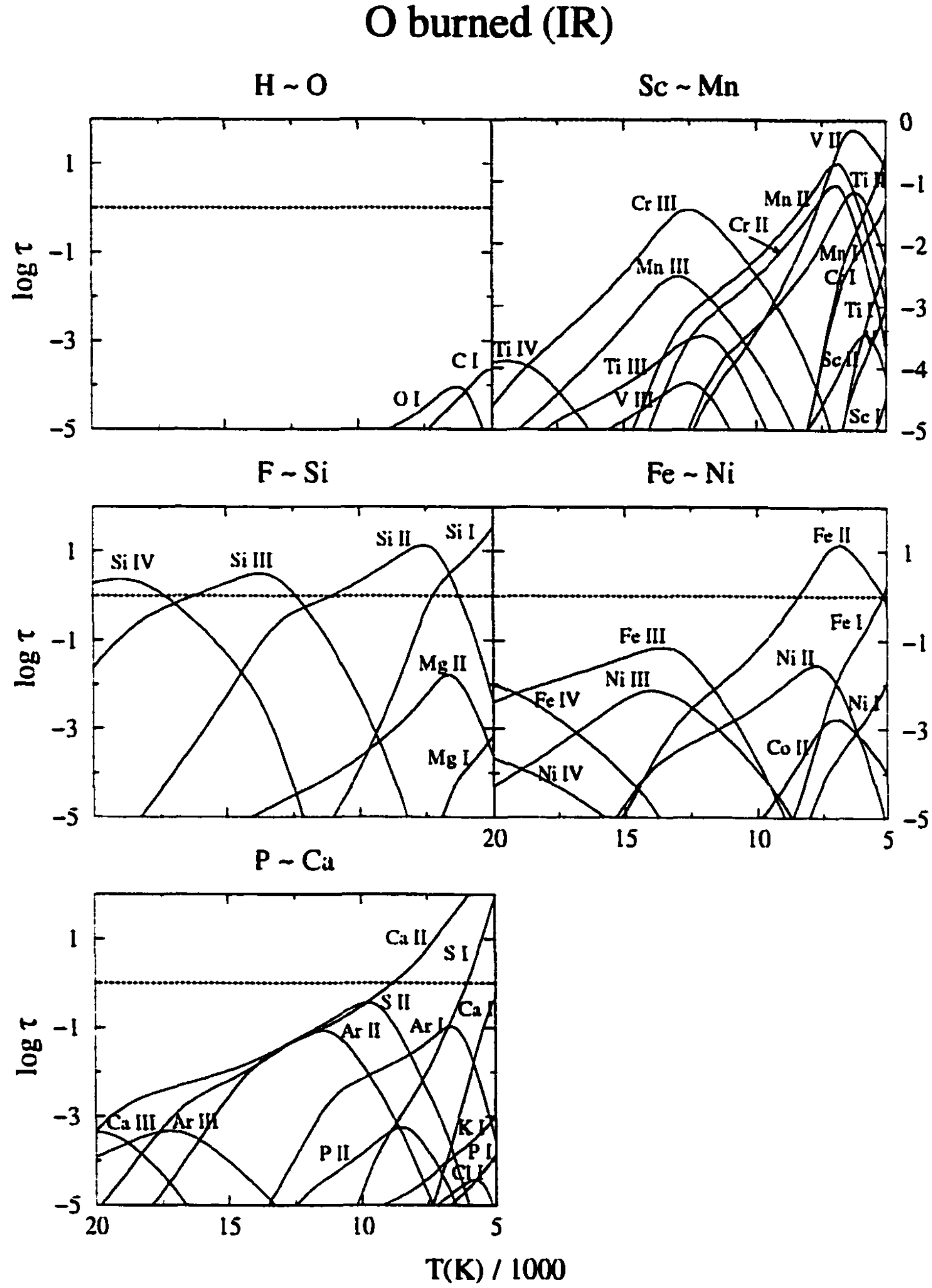

Figure 3.10: The log of the Sobolev LTE optical depth of IR ion reference lines, evaluated at $\tau_{es} = 1$, is plotted against temperature for the oxygen-burned composition.

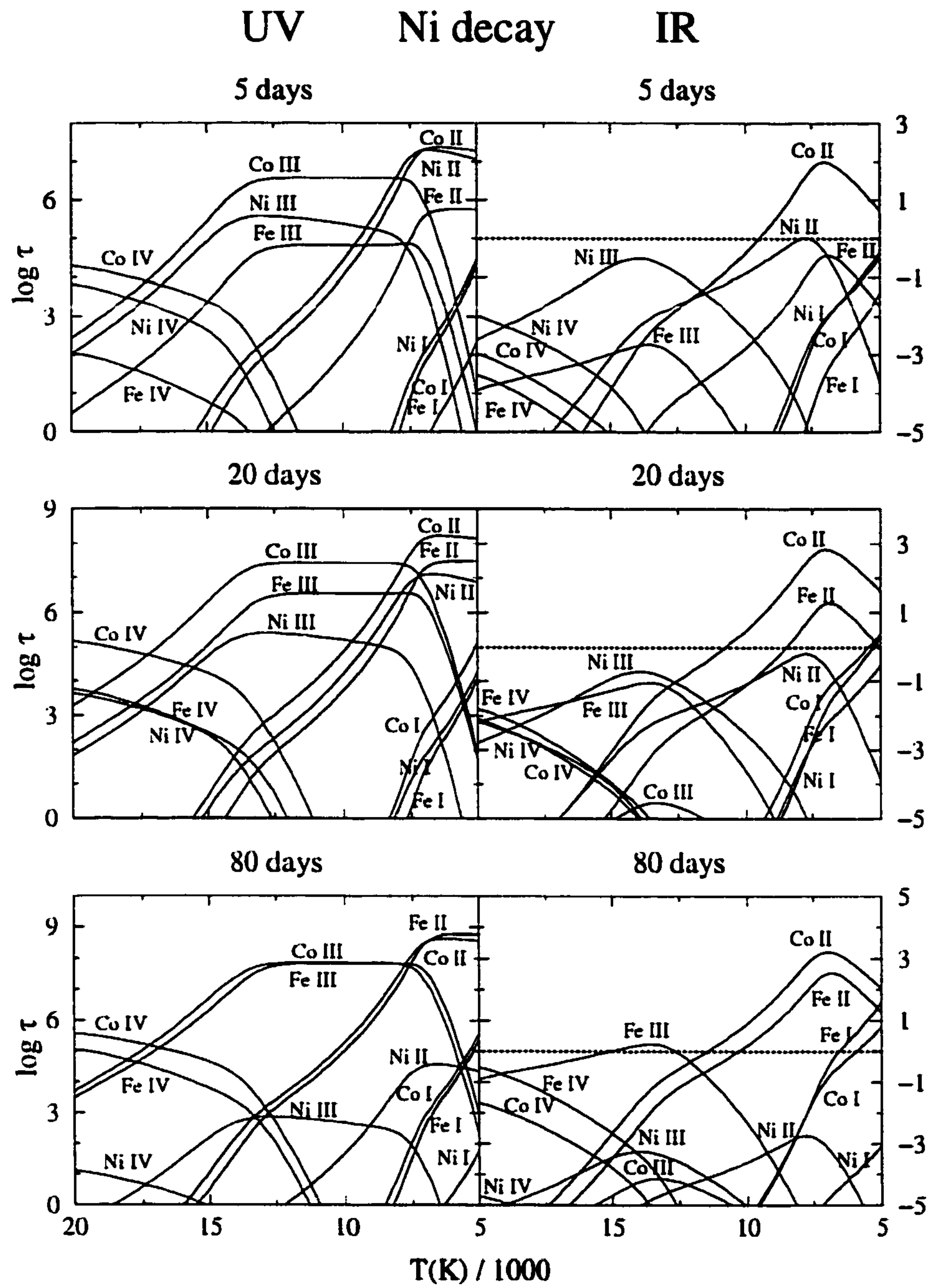

Figure 3.11: The log of the Sobolev LTE optical depth of UV and IR ion reference lines, evaluated at $\tau_{es} = 1$, is plotted against temperature for the ^{56}Ni decay composition.

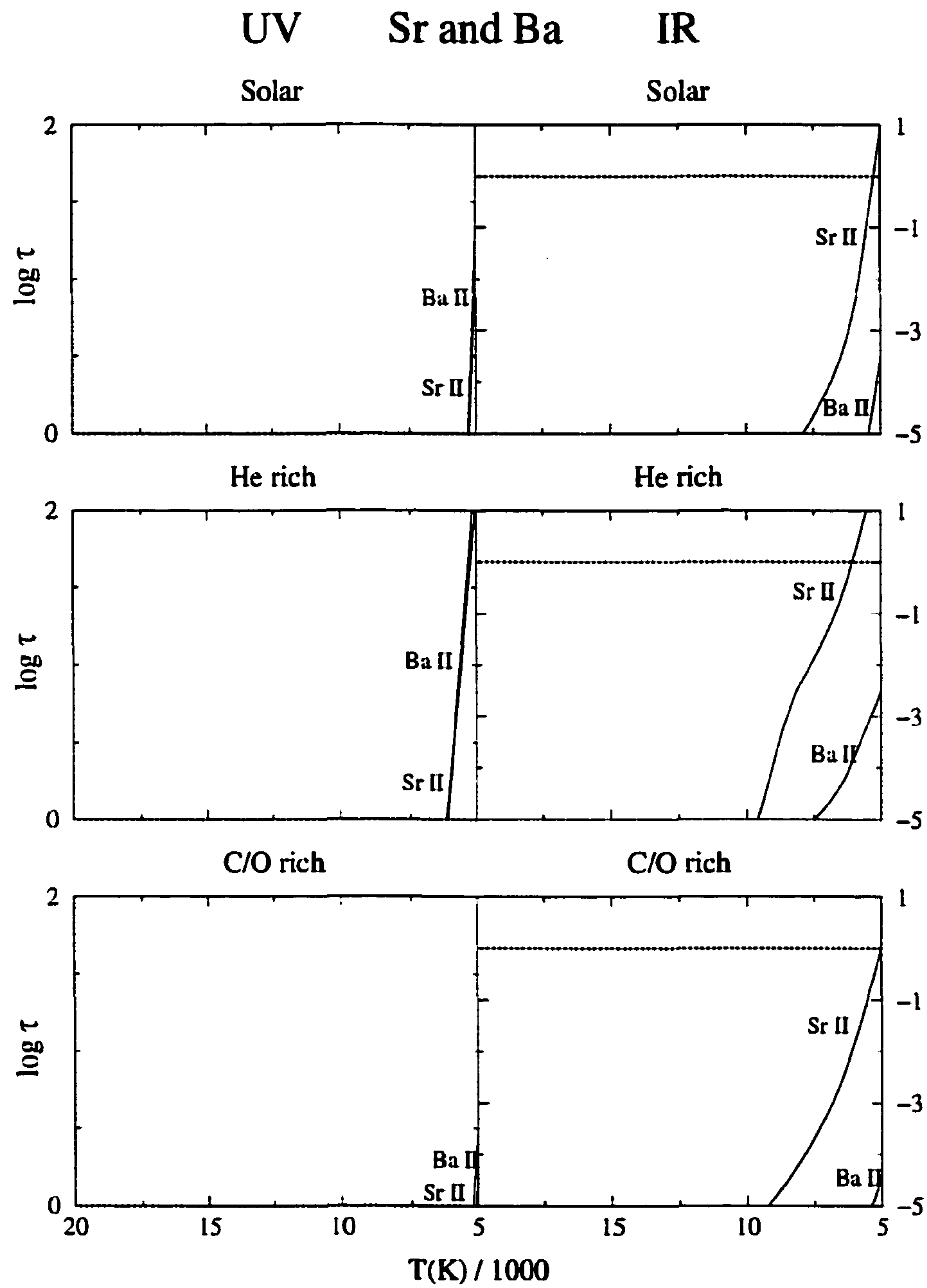

Figure 3.12: The log of the Sobolev LTE optical depth of UV and IR Sr and Ba reference lines, evaluated at $\tau_{es} = 1$, is plotted against temperature for 3 different compositions.

Chapter 4

On the High–Velocity Ejecta of the Type Ia Supernova 1994D

ABSTRACT

Synthetic spectra generated with the parameterized supernova synthetic–spectrum code SYNOW are compared to spectra of the Type Ia SN 1994D that were obtained before the time of maximum brightness. Evidence is found for the presence of two–component Fe II and Ca II features, forming in high velocity ($\geq 20,000$ km s^{-1}) and lower velocity ($\leq 16,000$ km s^{-1}) matter. Possible interpretations of these spectral splits, and implications for using early–time spectra of SNe Ia to probe the metallicity of the progenitor white dwarf and the nature of the nuclear burning front in the outer layers of the explosion, are discussed.

4.1 Introduction

SN 1994D, in the Virgo cluster galaxy NGC 4526, was discovered two weeks before the time of maximum brightness (Treffers et al. 1994) and became the best observed Type Ia supernova (Richmond et al. 1995; Patat et al. 1996; Meikle et al. 1996; Vacca & Leibundgut 1996; Filippenko 1997a,b). The high-quality early-time spectra of SN 1994D, beginning 12 days before maximum brightness, present us with an opportunity to look for spectral lines produced by "primordial" matter, i.e., heavy elements that were already present in the progenitor white dwarf before it exploded, as well as to probe the nature of the nuclear burning front in the outer layers of the ejected matter.

In this chapter we report some results of a "direct analysis" of photospheric-phase spectra of SN 1994D using the parameterized supernova spectrum-synthesis code SYNOW (Fisher et al. 1997, 1999; Millard et al. 1999; Fisher 2000). Here we concentrate mainly on spectra obtained before maximum light.

4.2 Previous Studies of SN 1994D Spectra

Numerous optical spectra of SN 1994D have been published by Patat et al. (1996), Meikle et al. (1996), and Filippenko (1997a,b). Patat et al. emphasized that in spite of some photometric peculiarities such as being unusually blue, SN 1994D had the spectral evolution of a normal SN Ia, especially like that of SN 1992A (Kirshner et al. 1993). Meikle et al. also emphasized the spectral resemblance to SN 1992A, and presented some near-infrared spectra.

Höflich (1995) calculated light curves and detailed non-local-thermodynamic-equilibrium (NLTE) spectra for a series of delayed-detonation hydrodynamical models and found that one particular model — M36, which contained 0.60 $M_{\odot}$ of freshly synthesized ^{56}Ni — gave a satisfactory representation of the light curves and spectra of SN 1994D. Synthetic spectra for model M36 were compared to observed SN 1994D spectra at epochs of $-10, -5, 0, 11$, and 14 days. (We cite spectrum epochs in days with respect to the date of maximum brightness in the B band, 1994 March 21 UT [Richmond et al. 1995].) The good agreement between the calculated and observed spectra and light curves indicated that the composition structure of SN 1994D resembled that of model M36 at least in a general way.

Patat et al. (1996) compared their observed -4 day spectrum to a Monte Carlo synthetic spectrum calculated for the carbon–deflagration model W7 (Nomoto, Thielemann, & Yokoi 1994), which has a composition in its outer layers that differs significantly from model that of M36. This calculated spectrum also agreed reasonably well with the observed spectrum.

Meikle et al. (1996) concentrated on identifying an infrared P Cygni feature that appeared in their pre–maximum–light spectra. They considered He I λ10830 and Mg II λ10926, and found that in parameterized synthetic spectra either transition could be made to give a reasonable fit, but then other transitions of these ions produced discrepancies elsewhere in the spectrum. Mazzali & Lucy (1998) also focused on identifying the infrared feature. They found that either He I or Mg II could be made to give a reasonable fit, but that neither could explain the rapid disappearance of the observed feature after the time of maximum brightness. Wheeler et al. (1998) favored the Mg II identification and concluded that within the context of delayed–detonation models the feature blueshift provides a sensitive diagnostic of the density at which the deflagration switches to a detonation.

4.3 Spectrum Synthesis Procedure

We have been using the fast, parameterized, supernova spectrum–synthesis code SYNOW to make a direct analysis of photospheric–phase spectra of SN 1994D. The goal has been to establish line identifications and intervals of ejection velocity within which the presence of lines of various ions are detected, without adopting any particular hydrodynamical model. In our work on SN 1994D we have made use of the results of Hatano et al. (1999a), who presented plots of LTE Sobolev line optical depths versus temperature for six different compositions that might be expected to be encountered in supernovae, and also presented SYNOW optical spectra for 45 individual ions that can be regarded as candidates for producing identifiable spectral features in supernovae. (Electronic data for the Hatano et al. [1999a] paper, now extended to include the near infrared, can be obtained at www.nhn.ou.edu/~baron/papers.html).

For comparison with each observed spectrum, we have calculated many synthetic spectra with various values of the fitting parameters. These include T_{bb}, the temperature of the underlying blackbody continuum; T_{exc}, the excitation temperature; and v_{phot}, the velocity of matter at the photosphere. For each ion that is introduced, the optical depth of a reference line also is a fitting parameter, with the optical depths of the other lines of the ion being calculated for LTE excitation at T_{exc}. We also can introduce restrictions on the velocity interval within which each ion is present; when the minimum velocity assigned to an ion is greater than the velocity at the photosphere, the line is said to be detached from the photosphere. The radial dependence of all of the line optical depths is taken to be exponential with e–folding velocity v_e = 3000 km s^{-1}, and the line source function is taken to be that of resonance scattering. All of the adopted fitting parameters are given in Tables 1-3. The most interesting parameters are v_{phot}, which as expected is found to decrease with time, and the individual ion velocity restrictions, which constrain the composition structure.

4.4 Results

4.4.1 Twelve Days Before Maximum

The -12 day observed spectrum appears in both the upper and lower panels of Figure 1. The upper panel also contains a SYNOW synthetic spectrum based on what could be called the conventional interpretation of early–time SN Ia spectra (Filippenko 1997b and references therein). The adopted value of v_{phot} is 15,000 km

ion	λ	τ	v_{min}	v_{max}	T_{exc}
Ca II	3934	500	...	40	10
Si II	6347	7	...	27	10
C II	4267	0.03	...	30	10
Ni II	4067	0.07	...	19	10
Co II	4161	0.1	...	19	10
Fe II	5018	0.8	...	17	10
S II	5454	3	...	15	10
Fe III	3013	1.2	18	19	10
Si III	4553	1	...	15	10
Mg II	4481	1	...	17	10
Na I	5890	0.3	...	24	10
Fe II	5018	1.5	22	29	10

Table 4.1: Fitting Parameters for figure 1

s^{-1}. The ions that are certainly required to account for certain spectral features are Ca II, Si II, S II, and Fe II. In an attempt to improve the fit we also have introduced weaker contributions from C II, Na I, Mg II, Si III, Fe III, Co II, and Ni II, some with minimum and maximum velocities as listed in Table 1. (Ions for which no minimum velocity is listed are undetached, i.e., their listed optical depths refer to the velocity at the photosphere, 15,000 km s^{-1}.) In spite of having a considerable number of free parameters at our disposal, we are left with two serious discrepancies: the observed absorption minima near 4300 and 4700 Å are not accounted for. (The discrepancy from 3900 Å to 4200 Å is not very troubling because SYNOW spectra often are underblanketed in the blue due to the lack of weak lines of unused ions.) We have been unable to remove the 4300 and 4700 Å discrepancies by introducing any additional ions that would be plausible under these circumstances, according to the LTE calculations of Hatano et al. (1999a).

The lower panel of Figure 1 shows what we consider to be the most plausible way to improve the fit. The only difference in the synthetic spectrum is that we have introduced a high-velocity Fe II component, from 22,000 km s^{-1} to 29,000 km s^{-1}. Note that this leaves a gap from 17,000 to 22,000 where the adopted Fe II optical depth is zero. Introducing the high-velocity component of Fe II accounts rather well for the 4300 and 4700 Å absorptions (and it also improves the 3900–4200 Å region).

For later reference we mention here that the apparent blue edge of the Ca II H&K absorption feature reaches to 40,000 km s^{-1} (or 32,000 km s^{-1} if formed by Si II λ3858, or 27,000 km s^{-1} if formed by Si III λ3801); the blue edge of the red Si II feature formed by λ6355 reaches to 25,000 km s^{-1}.

4.4.2 Eight and Two Days Before Maximum

In the upper panel of Figure 2 an observed −8 day spectrum is compared with a synthetic spectrum that has v_{phot} = 12,000 km s^{-1}. The other fitting parameters are listed in Table 2. Here, we use only a weak contribution from high-velocity Fe II, from 20,000 to 25,000 km s^{-1}, and without it the fit would be only slightly worse. But now, in this synthetic spectrum, we use two components of Ca II. A high-velocity (25,000 to 40,000 km s^{-1}) component of Ca II is the only plausible way we have found to account for the observed absorption from 7800 to 8000 Å. This feature is present in other spectra at similar epochs and therefore is definitely a real feature; we attribute it to the Ca II infrared triplet, forming in the high-velocity component.

In the lower panel of Figure 2 an observed −2 day spectrum is compared with a synthetic spectrum that has v_{phot} = 11,000 km s^{-1}. The other fitting parameters are listed in Table 3. In the synthetic spectrum we still are using two components of Ca II, one extending from the photosphere to 16,000 km s^{-1}, and the other from 20,000 to 23,000 km s^{-1}. This two-component calcium leads to good agreement with the observed "split" of the Ca II H&K feature. Other ways to account for the H&K split might be to invoke Si II λ3858 or Si III λ3801 (Kirshner et al. 1993; Höflich 1995; Nugent et al. 1997; Lentz et al. 2000a) but at this epoch of SN 1994D we find that in LTE, at least, other Si II or Si III lines would have to be made too strong compared

Fig 1

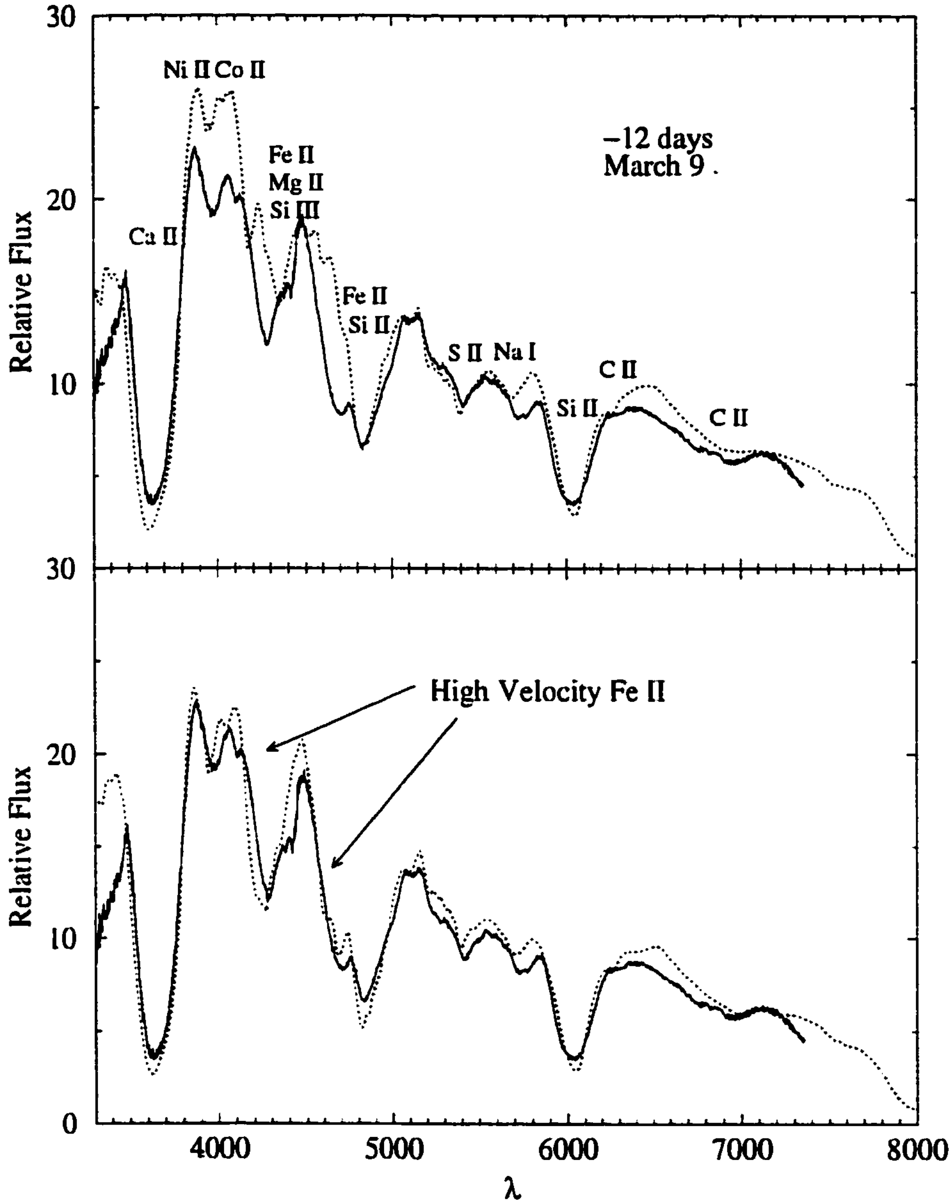

Figure 4.1: A −12 day observed spectrum in F_λ (Filippenko 1997a,b) is compared with synthetic spectra that have v_{phot} = 15,000 km s^{-1}. In the upper panel, ions that contribute features in the synthetic spectrum are labeled. In the lower panel a second, high-velocity component of Fe II is added. In this and subsequent figures, the spectra are in the SN 1994D rest frame.

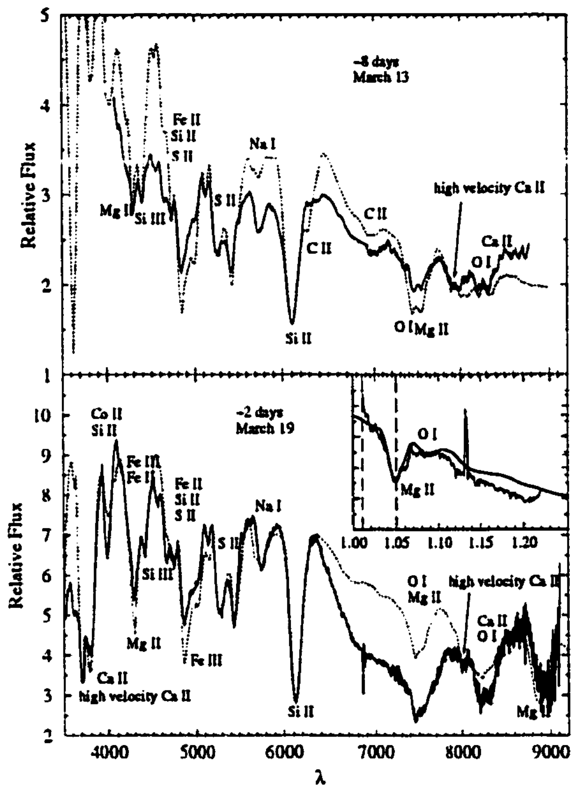

Figure 4.2: In the upper panel, a −8 day observed spectrum in F_ν (Patat et al. 1996) is compared to a synthetic spectrum that has v_{phot} = 12,000 km s^{-1}. In the lower panel, a −2 day observed spectrum in F_ν (Patat et al. 1996) is compared to a synthetic spectrum that has v_{phot} = 11,000 km s^{-1}. In the inset of the lower panel a −2 day near-infrared spectrum (Meikle et al. 1996) is compared with an extension of the optical synthetic spectrum, except that the O I reference-line optical depth has been reduced by a factor of three. (The narrow spike near 1.13 μm is an artifact.)

ion	λ	τ	v_{min}	v_{max}	T_{exc}
Ca II	3934	15	...	13	10
Ca II	3934	3	25	40	10
Si II	6347	1.2	...	20	15
C II	4267	0.02	14	30	10
O I	7772	0.35	14	20	10
Fe II	5018	1.2	...	16	10
S II	5454	2	...	14.5	15
Fe III	3013	0.4	14	20	10
Si III	4553	2.8	...	14	10
Mg II	4481	1	14	17	10
Na I	5890	0.2	...	20	10
Fe II	5018	0.2	20	25	10

Table 4.2: Fitting Parameters for figure 2 (top)

ion	λ	τ	v_{min}	v_{max}	T_{exc}
Ca II	3934	8	...	16	10
Ca II	3934	2.5	20	23	10
O I	7772	0.3	13	30	10
Si II	6347	1.7	...	16	10
Ni II	4067	0.2	...	20	10
Co II	4161	0.5	...	20	10
Fe II	5018	0.8	...	13	10
S II	5454	1.5	...	13	10
Fe III	3013	0.3	...	20	10
Si III	4553	0.3	...	14	10
Mg II	4481	0.6	13	17	10
Na I	5890	0.3	...	17	10
Fe II	5018	0.3	20	25	10

Table 4.3: Fitting Parameters for figure 2 (bottom)

with the observations. Our main reason for preferring the two-component Ca II at this epoch, however, is that it can account for the observed absorption near 8000 Å. (As we will discuss later, we find strong support for this interpretation in Figure 4 of Meikle & Hernandez (1999), which compares spectra of SNe 1981B, 1994D, and 1998bu. In SNe 1994D and 1998bu both the H&K and the infrared-triplet absorption features are split, while in SN 1981B neither is split.)

At present we have no explanation for the general difference between the levels of the observed and synthetic spectra from 6500 to 7900 Å, other than to note that we are inputting a simple blackbody continuum from the photosphere.

The inset in the lower panel of Figure 2 compares the observed spectrum near the 1.05 μm IR absorption to a synthetic spectrum that is an extension of the optical synthetic spectrum. We see that at this epoch Mg II, with the same reference-line optical depth we use to fit the optical features, accounts nicely for the IR absorption. Thus we, like Wheeler et al. (1998), favor the Mg II identification for the infrared absorption. The inset also illustrates the possibility that O I may be affecting the spectrum near 1.08 μm; here, in order not to mutilate the Mg II feature, we have had to reduce the O I reference-line optical depth by a factor of three compared to the value we used for the optical spectrum, which we would have to attribute to NLTE effects.

4.4.3 Evolution of the Ca II H&K Feature

Figure 3 shows the evolution of the Ca II H&K feature. If, as we suspect, the whole profile at -12 and -11 days is dominated by Ca II, then *some* Ca II must be present throughout the interval 15,000 - 40,000 km s^{-1}. At later times, from 21 to 74 days, the Ca II absorption forms only at velocities less than about 15,000 km s^{-1}. (The weak absorption near 3650 Å is probably produced by an iron-peak ion rather than by Ca II.) However, between -9 and -3 days the profile undergoes a complex evolution. While the highest-velocity absorption ($> 22,000$ km s^{-1}) fades away, and the low–

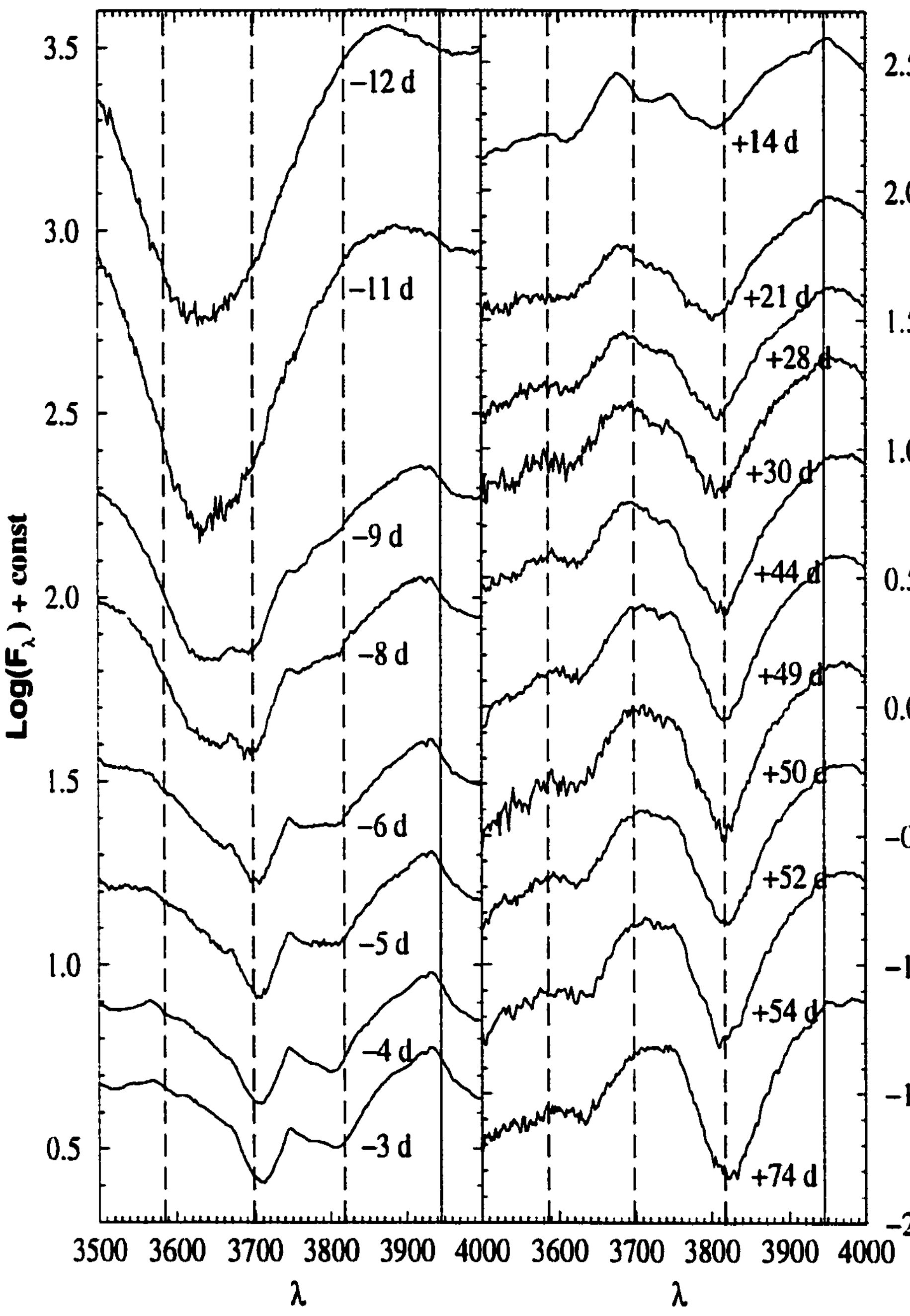

Figure 4.3: Observed spectra in the region of the Ca II H&K feature (Filippenko 1997a,b). The solid vertical line corresponds to 3945 Å (the gf-weighted rest wavelength of Ca II H&K) and the dashed vertical lines are blueshifted by 10,000, 20,000, and 30,000 km s^{-1}.

velocity absorption ($< 15,000$ km s^{-1}) develops, a dip appears near 19,000 km s^{-1} and a peak develops near 16,000 km s^{-1}. The 19,000 km s^{-1} dip is the bluer component of the split discussed above for -2 days. As explained in the previous section we suspect that the 19,000 km s^{-1} minimum is caused by Ca II (rather than by Si II or Si III) mainly because of the Ca II IR triplet. If this is so, then at these phases there must be a local minimum in the Ca II radial optical depth profile around 16,000 km s^{-1}. This is not necessarily inconsistent with the smooth H&K profiles at -12 and -11 days if at those early times the line optical depth was high throughout the 15,000 to 40,000 km s^{-1} interval.

4.5 Discussion

Assuming that our line identifications are correct, what is the cause of this complex spectral behavior? One part that seems clear is that all of the matter detected at velocities lower than about 16,000 km s^{-1} represents freshly synthesized material. And the highest-velocity matter — calcium up to 40,000 km s^{-1}, iron up to 30,000 km s^{-1}, and silicon up to 25,000 km s^{-1}(from the blue edge of the red Si II line), is likely to be primordial. This would be consistent with the predictions of Hatano et al. (1999a), for a composition in which hydrogen and helium have been burned to carbon and oxygen and the mass fractions of heavier elements are just solar; in this case the ions that are most likely to produce detectable spectral features from the primordial abundances are just the three that do appear to be detected at high velocity — Ca II, Fe II, and Si II.

However, what is the cause of the optical-depth minima of Ca II and Fe II, somewhere around 16,000 km s^{-1}? One possibility is that the ionization and excitation structure is such that the Ca II and Fe II lines, which decrease in strength with increasing temperature, have optical-depth minima around 16,000 km s^{-1}. Some weak support for this comes from the fact that in the -12 day spectrum we found Fe III lines, forming just between 19,000 and 20,000 km s^{-1}, to be helpful in fitting the spectrum. In addition, in detailed atmosphere calculations for model W7 with various primordial metallicities, Lentz et al. (2000a) find a temperature maximum for low metallicity (see also Höflich 1995). SN 1994D had an unusually negative value of $U - B$ for a Type Ia supernova, which could be an indication of low metallicity.

Another possibility is that there is a local minimum in the radial density profile around 16,000 km s^{-1}. Delayed-detonation models have smoothly decreasing densities in their outer layers, and deflagration models tend to have only low-amplitude density peaks and dips. Pulsating-detonation and tamped-detonation models have more pronounced density minima, but at least in published models they occur at velocities that are lower than 16,000 km s^{-1} (Khoklov, Müller, & Höflich 1993).

A third possibility is a nuclear explanation. Detailed nucleosynthesis calculations in delayed-detonation models recently have been carried out by Iwamoto et al. (1999). As we will discuss more thoroughly later, the composition structures of some of their models are generally consistent with most of the constraints that we have inferred for SN 1994D. In their model CS15DD1, for example, the fractional abundances of freshly synthesized silicon, sulfur, calcium, and iron begin to drop sharply above about 15,000 km s^{-1}, consistent with what we find for SN 1994D. It is interesting that in CS15DD1 the fractional abundances of sulfur and argon have pronounced minima around 16,000 km s^{-1}. Perhaps a delayed-detonation model could be constructed to have a minimum in the fractional abundance of freshly synthesized calcium around 16,000 km s^{-1}, although it seems unlikely that such could be the case for iron. It should be noted that the synthesis of calcium and iron depends on the initial metallicity (Höflich et al. 1998). Iwamoto et al. did not include primordial metals in their models. Perhaps when primordial metals are included, models will be found in which both calcium and iron have fractional abundance minima near 16,000 km s^{-1}, if nuclear reactions can reduce the levels of calcium and iron below the primordial levels at this velocity. These possibilities appear to be plausible and they are being investigated (F.-K. Thielemann, personal communication).

4.6 Conclusion

Based on our interpretation of the pre–maximum-brightness spectra of SN 1994D, it appears that given high-quality spectra obtained at sufficiently early times, it should be possible to probe the primordial composition of the SN Ia progenitor (see also Lentz et al. 2000a). This will be important in connection with using high-redshift SNe Ia as distance indicators for cosmology (Branch 1998; Perlmutter et al. 1998; Riess et al. 1998), for testing the predicted dependence of hydrodynamical models on primordial composition (Höflich et al 1998), and for testing the prediction that low metallicity inhibits the ability of white dwarfs to produce SNe Ia (Kobayashi et al. 1998). It also appears that early spectra of SNe Ia can be used to place useful constraints on the nature of the nuclear burning front in the outer layers of the ejected matter.

Transforming the present somewhat qualitative indications into reliable quantitative results will require (1) further parameterized spectrum calculations, as part of a detailed comparative study of early-time spectra of SNe Ia (Hatano et al., in preparation); (2) detailed NLTE calculations for SN Ia hydrodynamical models before the time of maximum light (Nugent et al. 1997; Höflich et al. 1998; Lentz et al. 2000a); (3) further detailed calculations of nucleosynthesis in parameterized hydrodynamical explosion models (Iwamoto et al. 1999); and (4) many more high-quality observed spectra of SNe Ia before the time of maximum brightness.

We conclude this chapter by showing early-time spectra of SN 1999aa to emphasize that the split of Ca II H&K line is produced by high-velocity calcium, not by Si II nor Si III. Fig. 4 shows the log of SN 1999aa spectra with Synow spectra, at 10 days before maximum brightness (top) and near maximum brightness (bottom). A detailed analysis of these fits will be presented later. This is a hot, peculiar SN Ia like SN 1991T and SN 1997br. The upper panel shows that only high-velocity calcium produces H&K and infrared triplet lines. But, the lower panel shows that low-velocity calcium also produces H&K and infrared triplet lines, in addition to high-velocity

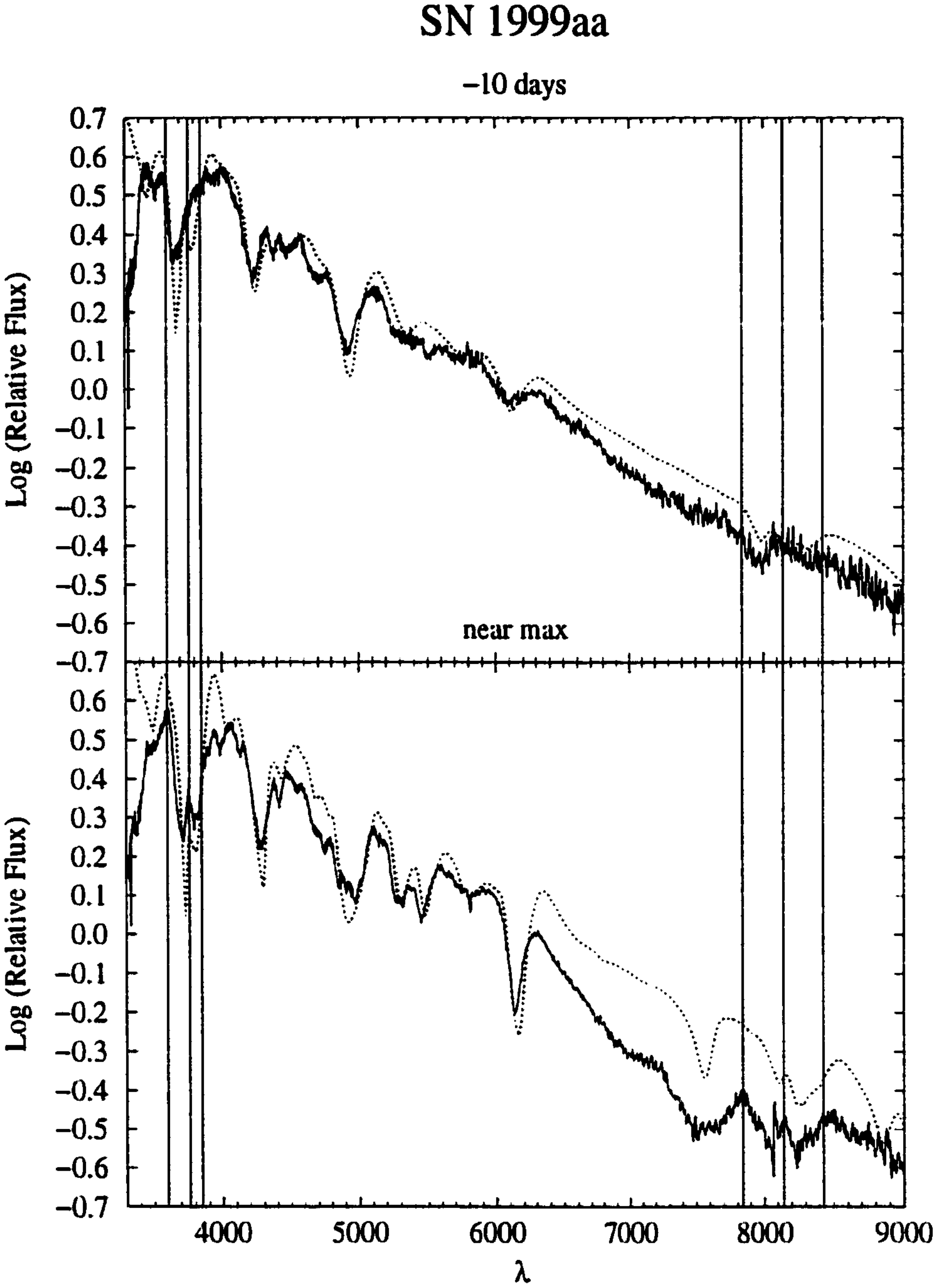

Figure 4.4: Observed spectra (solid lines) are provided by Alex Filippenko (publications in preparation), about 10 days before maximum brightness and near maximum brightness. The dotted lines are Synow spectra. The vertical lines clarify the split of Ca II lines (H&K and infrared triplet).

component. While the red Si II line near 6150 Å becomes much stronger by near maximum, the strength of high–velocity Ca II lines stays about the same. Therefore, the high–velocity component of Ca II H&K split is produced by high–velocity calcium, not by Si II nor Si III.

We are grateful to Dean Richardson and Thomas Vaughan for assistance, to Friedel Thielemann for discussions of nucleosynthesis in hydrodynamical models, and to Alex Filippenko, Ferdinando Patat and Peter Meikle for making their observed spectra available in electronic form.

Chapter 5

On the Spectrum of the Peculiar Type Ia Supernova 1997br and the Nature of SN 1991T-like Events

ABSTRACT

In a recent paper (Fisher et al. 1999) we discussed the optical spectra and the nature of the peculiar Type Ia SN 1991T. Since then, Li et al. (1999) have presented extensive observational data on the peculiar Type Ia SN 1997br, another SN 1991T-like event. Here we present some results of a direct analysis of the spectra of SN 1997br, and further discuss the nature of SN 1991T-like events. The issues of whether or not they are a discrete subgroup of SNe Ia, and the extent to which their spectra could be consistent with standard, Chandrasekhar-mass, delayed-detonation hydrodynamical models, are discussed.

5.1 Introduction

SN 1991T was a well observed and spectroscopically peculiar Type Ia supernova (Filippenko et al. 1992b; Phillips et al. 1992; Ruiz–Lapuente et al. 1992; Jeffery et al. 1992; Mazzali, Danziger, & Turatto 1995). The most striking observational peculiarity was that before and around the time of maximum brightness its optical spectra showed conspicuous lines of Fe III rather than the usual SN Ia lines such as Si II, S II, and Ca II. In SN 1991T, the deep red Si II absorption that is characteristic of normal SNe Ia finally did develop after maximum light, but it never reached its usual strength.

Recently we (Fisher et al. 1999 ≡ FBHB) presented some results of a "direct" analysis of optical photospheric–phase spectra of SN 1991T based on the parameterized supernova synthetic–spectrum code SYNOW. We studied line identifications and tried to establish some constraints on the composition structure of the ejected matter, and we concluded that the composition structure of SN 1991T was unlike that of any published hydrodynamical model for SNe Ia. We also found that SN 1991T probably was too luminous to have been produced by a Chandrasekhar-mass explosion, so we suggested that it may have been a substantially super–Chandrasekhar explosion that resulted from the merger of two white dwarfs.

Li et al. (1999) have presented extensive photometric and spectroscopic observations of another peculiar Type Ia event, SN 1997br. They show that SN 1997br closely resembled SN 1991T, both photometrically and spectroscopically. By carefully comparing the observational data on these two events, Li et al. also were able to establish that they showed small but real differences: in SN 1997br, the red Si II absorption was present for an even more limited period of time than it was in SN 1991T, and the post–maximum–light transition to a spectrum dominated by Fe II lines occurred earlier. In this chapter, we report some results of a direct analysis of spectra of SN 1997br, and further discuss the nature of SN 1991T–like events.

5.2 Procedure and Results

We have used SYNOW to study line identifications and the velocity intervals in which the presence of lines of various ions can be detected. Our spectrum synthesis procedure was similar to that described in FBHB, so it will not be discussed in detail here. The basic assumptions are spherical symmetry, a sharp photosphere, the Sobolev approximation, a resonance–scattering line source function, and exponential radial optical–depth profiles. A strength of this kind of analysis is that it is possible to calculate a large number of synthetic spectra for comparison with observed spectra, adjust the input parameters to obtain a good fit, and extract some constraints on the composition structure in an empirical spirit. A weakness is that level populations are not obtained from a solution of rate equations, so reliable quantitative abundances can not be derived.

For each synthetic spectrum, the adjustable parameters are the temperature of the blackbody continuum T_{bb}, the excitation temperature T_{exc} (in this chapter, T_{exc} is simply equated to T_{bb} at each epoch), the velocity at the photosphere v_{phot}, maximum and minimum velocities that can be imposed on any ion, and the optical depth at the photosphere of a "reference line" for each ion. When the minimum velocity of an ion exceeds the velocity at the photosphere the ion is said to be detached; otherwise the minimum velocity is the same as the velocity of the photosphere. As in FBHB, the radial dependence of the line optical depths is taken to be exponential with an e–folding velocity v_e = 3000 km s^{-1} (with one exception to be mentioned below). The most interesting parameters are the velocity parameters. Further details of the spectrum–synthesis procedure are described by FBHB. A detailed description of the SYNOW code is in Fisher (2000).

We have studied spectra of SN 1997br at 14 epochs ranging from −9 to +67 days. (Epochs are in days with respect to the date of maximum brightness in the B band, April 20, 1997 [Li et al. 1999].) The spectra have been de–redshifted to the supernova rest frame and corrected for interstellar extinction using $E(B-V) = 0.35$ as estimated

epoch	ion	λ	τ	v_{min}	v_{max}	T_{exc}
-9	Fe III	4420	0.7	...	20.5	14
	Ni III	4613	0.1	...	20.5	14
-7	Si III	4553	0.5	...	15.5	13
	Fe III	4420	0.8	...	20.5	13
	Ni III	4613	0.1	...	20.5	13
-4	Si II	6347	0.5	...	15.5	13
	Si III	4553	0.5	...	15.5	13
	Ca II	3934	2	...	50	13
	Fe III	4420	0.8	...	20.5	13
	Ni III	4613	0.1	...	20.5	13

Table 5.1: Fitting Parameters for Figure 1

by Li et al. For comparison with each observed spectrum we have calculated a large number of synthetic spectra with various values of the fitting parameters. As usual when introducing ions into SYNOW calculations, we have been guided by the LTE optical-depth calculations of Hatano et al. (1999a). Here, as examples, we present comparisons of synthetic spectra with observed spectra for five of the epochs we have studied.

5.2.1 Pre–maximum

Fig. 1 shows comparisons of −9, −7, and −4 day observed spectra with synthetic spectra. (Table 1 lists the optical depths of the reference lines and other information.) The synthetic spectrum for −9 days (top panel) has v_{phot}=13,500 km s^{-1}, T_{bb} = 14,000 K, and lines of only Fe III and Ni III. Fe III lines were first identified in SN 1991T by Filippenko et al. (1992b) and Ruiz–Lapuente et al. (1992), and they obviously also are present in SN 1997br. The presence of Ni III lines, first identified in SN 1991T by Ruiz–Lapuente et al. (1992), is an important issue (see below);

Fig 1

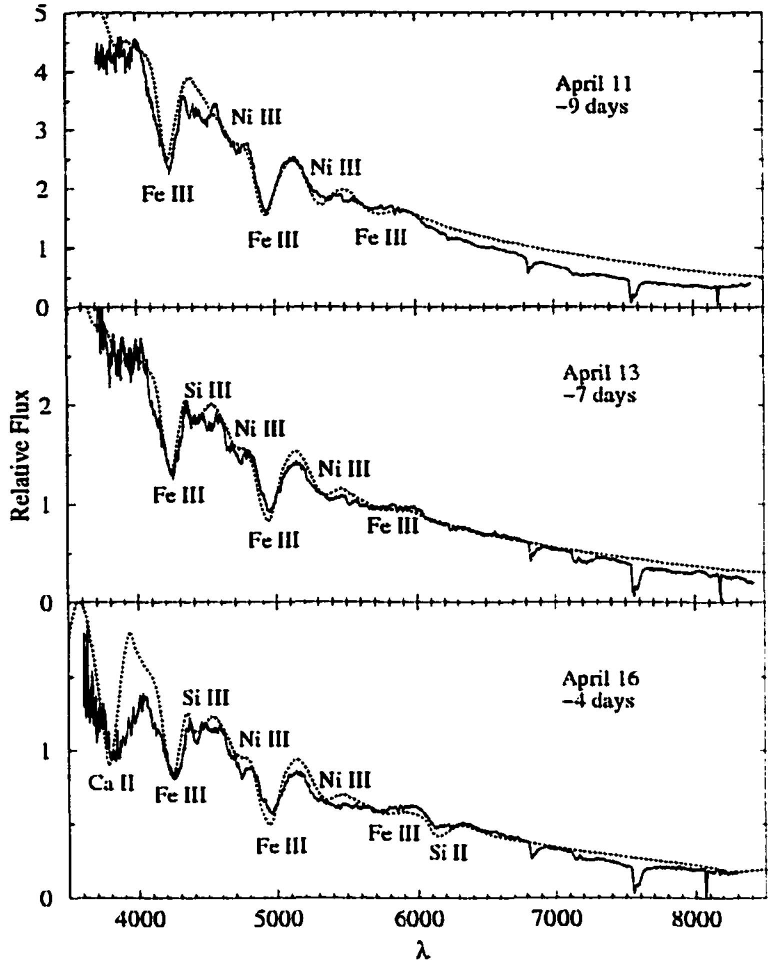

Figure 5.1: Spectra of SN 1997br obtained by Li et al. (1999) at epochs of −9, −7, and −4 days are compared to synthetic spectra. Ions responsible for features in the synthetic spectra are marked. The parameters of the synthetic spectra are given in the text and in Table 1. Wavelengths are in the rest frame of SN 1997br and relative fluxes are per unit wavelength interval. Narrow absorptions near 6800, 7200, and 7600 Å are telluric.

we consider Ni III lines to almost certainly be present in SN 1997br. A maximum velocity of 20,500 km s^{-1} has been imposed on the Fe III lines to improve the fit. (The same maximum velocity has been imposed on Ni III but its lines are too weak for this maximum velocity to make any difference.)

The synthetic spectrum for −7 days (middle panel of Fig. 1) is much like that for −9 days (v_{phot}has been reduced to 12,500 km s^{-1}, T_{bb} has been reduced to 13,000 K) but now Si III lines also have been introduced. Si III λ4560, first identified in SN 1991T by Jeffery et al. (1992), can account for the weak absorption near 4400 Å, and we consider its presence in the observed spectrum of SN 1997br to be probable. A maximum velocity of 15,500 km s^{-1} has been imposed on Si III to improve the fit. At present we are uncertain about the identification of the neighboring weak absorption near 4500 Å. C III λλ4649, 4663 is a possibility but in SYNOW spectra the predicted absorption is bluer than the observed one. He II λ4686 would give a better fit.

By −4 days (bottom panel of Fig. 1) the observed spectrum is still quite peculiar, but some of the regular SN Ia features have begun to develop. In the synthetic spectrum we have introduced weak lines of Ca II and Si II (the latter with a maximum velocity of 15,500 km s^{-1}, as for Si III lines). At present the discrepancy near 4000 Å is unexplained. Li et al. (1999) estimate that the apparent blue edge of the Si II absorption near 6100 Å corresponds to a velocity of 18,000 km s^{-1}, and they note that in the classical model W7 of Nomoto, Thielemann, & Yokoi (1984), synthesized silicon extends only up to 15,000 km s^{-1}. However, Fig. 1 suggests that the maximum velocity of the Si II line is uncertain in SN 1991T–like events, because it appears to be affected by the presence of the Fe III lines that produce a bump in the synthetic spectrum just short of 6000 Å. The Fe III emission could mask the blue edge of the Si II absorption and cause an underestimate of the Si II maximum velocity; on the other hand the downward slope of the red side of the Fe III emission could be mistaken for an extended blue edge of the Si II absorption, causing an overestimate of the Si II maximum velocity.

epoch	ion	λ	τ	v_{min}	v_{max}	T_{exc}
+8	O I	7772	0.2	...	50	10
	Na I	5890	0.4	...	50	10
	Mg II	4481	1.5	...	20.5	10
	Si II	6347	0.7	...	15.5	10
	S II	5454	0.5	...	13.5	10
	Ca II	3934	10	...	50	10
	Fe II	5018	1	...	50	10
+38	O II	7321	0.7	...	30.5	7
	Na I	5890	0.5	8.5	50	7
	Ca II	3934	500	...	50	7
	Fe II	5018	50	...	12.5	7
	Fe II	5018	1	12.5	50	7
	Co II	4161	50	...	12.5	7
	Co II	4161	1	12.5	50	7

Table 5.2: Fitting Parameters for Figure 2

5.2.2 Post–maximum

Li et al. (1999) did not obtain spectra of SN 1997br between −4 and +8 days because of poor weather and the brightness of the moon. Fig. 2 shows comparisons of +8 and +38 day observed spectra with synthetic spectra. (Optical depths of the reference lines are listed in Table 2.) By +8 days (upper panel) the observed spectrum looks only moderately peculiar. The synthetic spectrum has v_{phot}=10,500 km s^{-1}and T_{bb} = 10,000 K, and it contains just the usual post-maximum-brightness SN Ia ions: O I, Na I, Mg II, Si II, S II, and Fe II. Maximum velocities of 20,500, 15,500, and 13,500 km s^{-1} have been imposed on Mg II, Si II, and S II, respectively, to improve the fit. (Fig. 3 of FBHB, for SN 1991T at +6 days, shows how the fit deteriorates when the maximum velocities of Si II and S II are removed.) There is an unexplained discrepancy near 4100 Å, and as usual in post–maximum–brightness

Fig 2

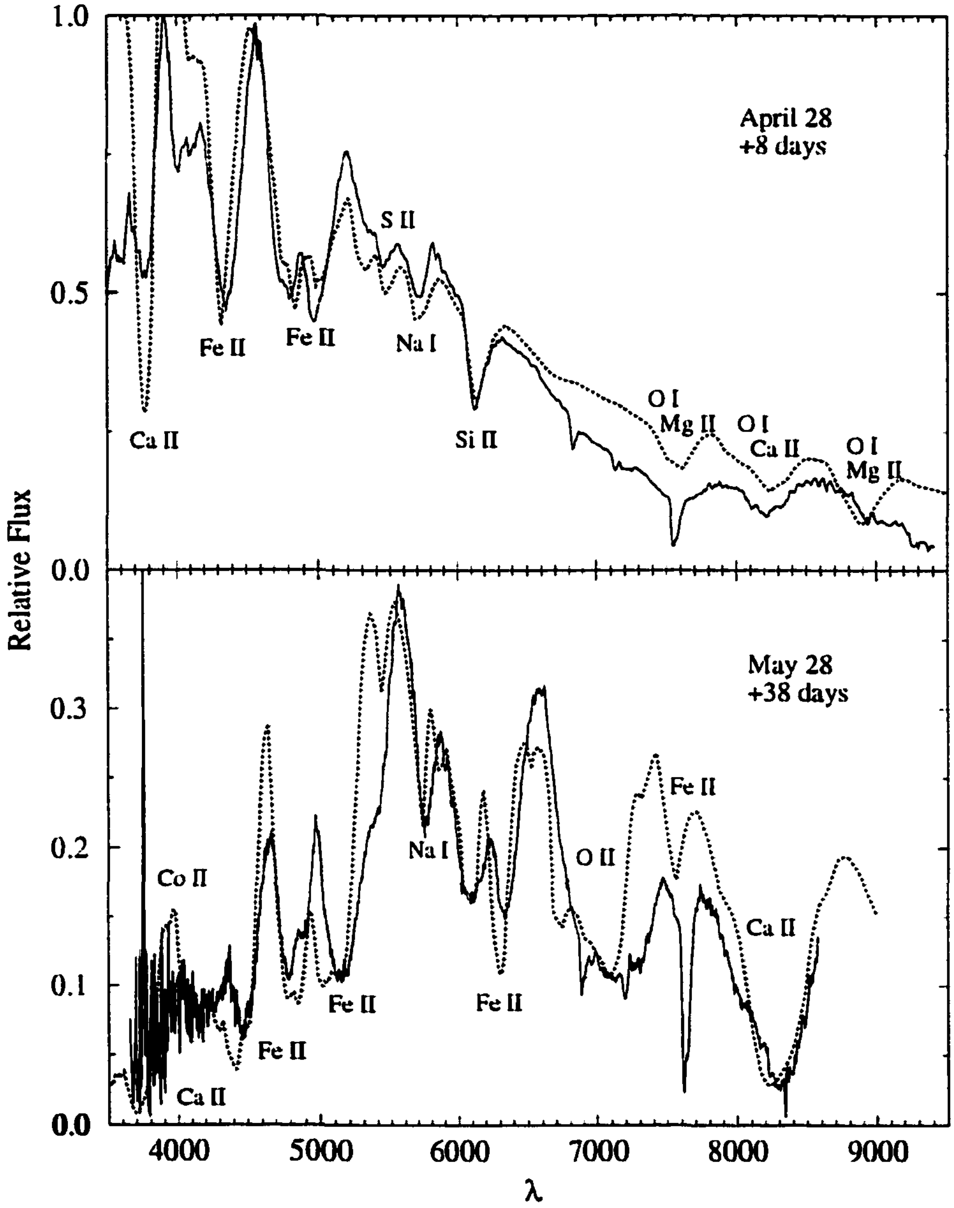

Figure 5.2: Like Fig. 1, but for epochs of +8 and +38 days. Parameters of the synthetic spectra are given in the text and in Table 2.

v_{disc}	τ_{in}	τ_{out}
8,000	50	3.8
10,000	50	2
12,000	50	1
14,000	50	0.5
16,000	50	0.25

Table 5.3: Parameters for Iron Core (Figure 3)

SNe Ia (e.g., Hatano et al. 1999b), our assumed blackbody continuum makes the synthetic spectrum brighter than the observed spectrum from about 6500 to 8000 Å.

By +38 days (lower panel of Fig. 2) the observed spectrum looks much like that of a normal SN Ia. The synthetic spectrum has v_{phot}=6500 km s^{-1} and T_{bb} = 7000 K, and it contains lines of Na I, O II, Ca II, Fe II, and Co II. There is a discrepancy near 5300 Å that can be reduced by increasing the optical depths of the Fe II lines, but then other discrepancies are produced elsewhere in the spectrum. Lines of O II have been introduced, with a shallow radial optical-depth gradient (v_e = 20,000 km s^{-1}, an arbitrary high value), so that [O II] $\lambda\lambda$7320,7330 can account for most of the broad absorption around 7000 Å. However, with our $v_{phot}$of 6500 km s^{-1}, [O II] cannot account for the red edge of this absorption. As we (FBHB; Hatano et al. 1999b; Millard et al. 1999) have discussed elsewhere, the [O II] lines are spectroscopically attractive for fitting post-maximum spectra of SNe Ia and Ic, but rough estimates of the mass of oxygen and the kinetic energy that it carries are uncomfortably high — at least for SNe Ia, which have stringent kinetic energy limits if they are thermonuclear disruptions of white dwarfs.

In the synthetic spectrum for +38 days we have introduced an abrupt decrease in the Fe II and Co II optical depths, by a factor of 6.7, at 12,500 km s^{-1}. (This is why Fe II and Co II each appear twice in Table 2.) For SN 1991T, FBHB introduced a similar discontinuity, but at 10,000 km s^{-1}. Fig. 3 shows the extent to which the synthetic spectrum depends on the velocity at which the optical-depth discontinuity

Fig 3

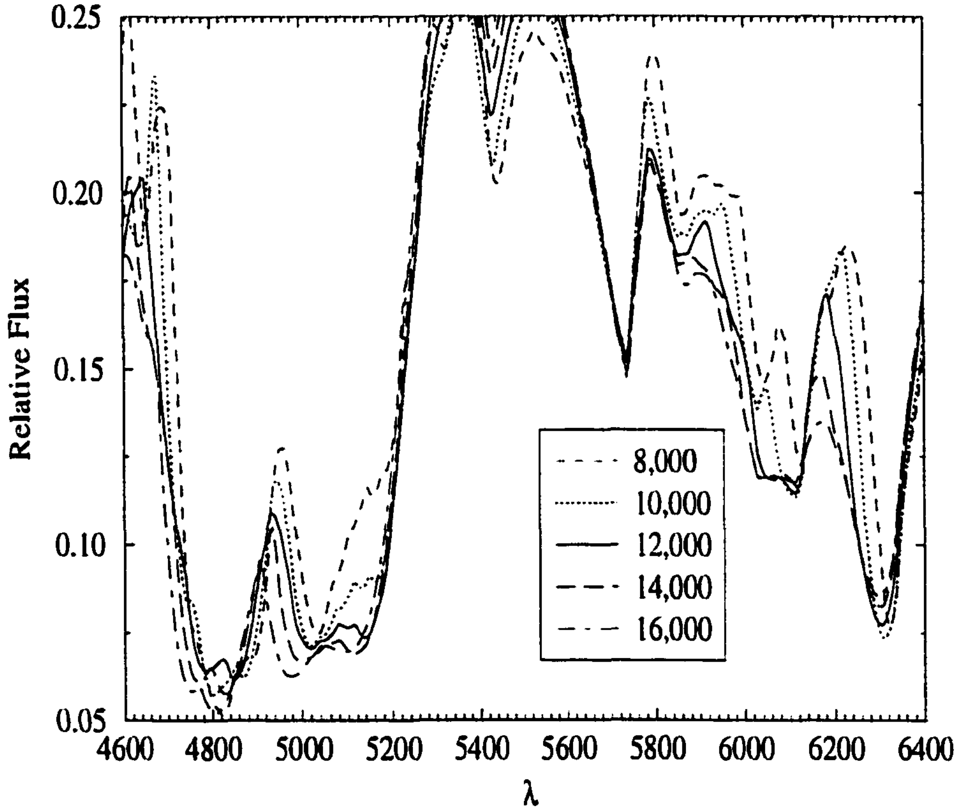

Figure 5.3: Synthetic spectra like that of the lower panel of Fig. 2, except that the Fe II and Co II optical-depth discontinuities are placed at five different velocities. Parameters for the synthetic spectra are given in the text and in Table 3.

is placed. The optical depths used for both the Fe II Co II reference lines in the spectra of Fig. 3 are listed in Table 3. The parameter τ_{in}, the optical depth at the photospheric velocity of 6500 km s^{-1}, was held fixed at 50, while τ_{out}, the optical depth at the velocity of the discontinuity, was chosen such that the optical-depth discontinuity always was a factor of 6.7.

5.3 Discussion

As expected from the close similarity of the observed spectra of SNe 1997br and 1991T (Li et al. 1999), our interpretation of the spectra of SN 1997br is similar to that of FBHB for SN 1991T. In general our results are consistent with SN 1997br being a slightly stronger version of SN 1991T, as Li et al. suggested. For example, we place the outer edge of the iron core at 12,500 km s^{-1} in SN 1997br, while we had it at 10,000 km s^{-1} in SN 1991T. The difference between these two velocities is not very well determined but it does appear to be significant.

An important question about SN 1991T-like events is whether or not they are a discrete subgroup of SNe Ia that is physically distinct from normal SNe Ia. For example, SN 1991T-like events could be substantially super-Chandrasekhar mergers in double-degenerate progenitor binary systems, as suggested by FBHB, while normal SNe Ia could be explosions of Chandrasekhar-mass white dwarfs in single degenerate systems, or double-degenerate mergers near the Chandrasekhar mass. Or, SN 1991T-like events could be "late detonations" that synthesize ^{56}Ni in high-velocity layers (Yamaoka et al. 1992) while normal SNe Ia are standard deflagrations or delayed detonations that don't synthesize any ^{56}Ni in their outer layers.

One of the reasons FBHB suggested that SN 1991T was a substantially super-Chandraskhar merger product was that it appeared to have been too luminous for a Chandrasekhar-mass ejection. FBHB assumed a distance to SN 1991T of 16.4 Mpc. More recently Sparks et al. (1999), on the basis of a simple model of the evolution of the SN 1991T light echo discovered by Schmidt et al. (1994), derive an upper limit of 15 Mpc. If correct, this would ease the problem of the apparent overluminosity of SN 1991T. Li et al. (1999) discuss the absolute magnitude of SN 1997br, and they conclude that it too may have been somewhat more luminous than normal SNe Ia. The conclusion is uncertain, however, because SN 1997br had to be corrected for a substantial amount of extinction ($A_B = 1.4$ mag) and, being an apparent member of a galaxy group that has a mean recession velocity of only 1583 km s^{-1}, it isn't really in the Hubble flow.

One of the reasons that FBHB concluded that the composition structure of SN 1991T was unlike that of any published SN Ia hydrodynamical model was the inferred presence of C II lines down to a velocity at least as low as 15,000 km s^{-1}, together with the inferred presence of Ni III lines at velocities that extended beyond 15,000 km s^{-1}. No SN Ia hydrodynamical model has carbon and freshly synthesized nickel coexisting in velocity space. FBHB noted that the presence of an absorption feature near 6300 Å, tentatively attributed to C II λ6580, could be seen in practically all spectra of SN 1991T that were obtained earlier than −6 days. In SN 1997br, however, we see no convincing evidence of this feature even in the −9 day spectrum. It may be that SN 1997br, being more powerful than SN 1991T, ejected carbon only at higher velocities than in SN 1991T, so that the C II line could have been detected only at epochs earlier than −9 days. On the other hand, it remains possible that the 6300 Å minimum in SN 1991T is not really produced by C II. This is a very good example of the importance of observing SN Ia spectra as soon after explosion as possible; at best, the C II lines will be weak and fading rapidly, so the earlier the spectrum is observed, the better will be the chance of firmly establishing the presence, and the minimum velocity, of ejected carbon.

Do the conspicuous spectral differences between SN 1991T-like events and normal SNe Ia indicate that the former comprise a distinct subgroup? The presence of Fe III lines in the early-time spectra, at the expense of the usual Si II, S II, and Ca II lines, does not in itself establish that the composition of the outer layers of SN 1991T-like events is fundamentally different from that of normal SNe Ia. If SN 1991T-like events are just more powerful versions of normal SNe Ia, that synthesize more ^{56}Ni, then they are expected to be hotter than normal SNe Ia at each epoch, and it has been demonstrated (Jeffery et al. 1992; Nugent et al. 1995a; Mazzali et al. 1995) that high temperature can account for at least some of the spectral peculiarities of SN 1991T-like events. This is because of the strong dependence of the line optical depths on temperature, in the range of interest. For example, Fig. 5 of Hatano et al. (1999a) shows that (in LTE) as the temperature rises from 10,000 to 12,500 K, the ratio of the Fe III and Fe II reference-line optical depths increases by a factor of about 160, and that of Si III and Si II increases by a factor of about 800. Thus there could be a temperature threshold, just below which SNe Ia look normal, perhaps like SN 1990N, and just above which they develop Fe III features and look like SN 1991T. (Similarly, there may be a low-temperature threshold, just above which SNe Ia look normal, perhaps like SN 1992A, and just below which they develop Ti II lines and look peculiar, like SN 1986G.)

If we temporarily disregard the tentative evidence for low-velocity carbon in SN 1991T, and the apparently high luminosity of SN 1991T, then we should consider whether the composition structure of SN 1991T-like events could be consistent with standard delayed-detonation models. In this chapter we found it helpful to introduce a discontinuity in the Fe II and Co II optical depths at 12,500 km s^{-1}, which we associate with the outer edge of the iron-peak core. During the pre-maximum phases we see lines of Fe III and Ni III forming above 12,500 km s^{-1}, but *not* lines of Co III. The latter would be expected if the Ni III lines were produced by freshly synthesized ^{56}Ni (see Fig. 9 of Hatano et al. 1999a), but if they are included they spoil the fit. This suggests that the iron and nickel that produced the Fe HI and Ni III lines actually were stable ^{54}Fe and stable ^{58}Ni, synthesized during silicon burning, rather than ^{56}Ni and ^{56}Fe as has been assumed in previous discussions of SN 1991T. This would be consistent with the absence of Co III lines (Fig. 7 of Hatano et al. 1999a). Then later, after maximum brightness, when the photosphere had retreated inside the iron-peak core, the Co II and Fe II lines were produced by ^{56}Co and ^{56}Fe from the decay of ^{56}Ni, at velocities lower than 12,500 km s^{-1}.

An example of a Chandrasekhar–mass, delayed–detonation model that could possibly apply to SN 1991T–like events can be suggested. Iwamoto et al. (1999) present and discuss several delayed–detonation models, including CS15DD1, CS15DD2, and CS15DD3, in which the deflagration–detonation transition occurs at densities of 1.7×10^7, 2.2×10^7, and 3.0×10^7 g cm^{-3} and the ejected masses of ^{56}Ni are 0.56, 0.74, and 0.83 $M_\odot$, respectively. On the basis of nucleosynthesis constraints, Iwamoto et al. prefer a model closer to CS15DD2 than to CS15DD1 for the typical SN Ia; on the basis of spectra, Hatano et al. (1999b) discuss model CS15DD1 as a possible approximate representation of the normal Type Ia SN 1994D. On the basis of nucleosynthesis, model CS15DD3 was disfavored for normal SNe Ia by Iwamoto et al. There is no strong nucleosynthesis argument against model CS15DD3 as a representation of SN 1991T–like events, however, because they are relatively rare.

In Fig. 4, for model CS15DD3, the densities (not the mass fractions, which are usually plotted) of selected, spectroscopically interesting isotopes are plotted against velocity. In the upper panel the densities are on a log scale so that all of the important isotopes can easily be seen on one plot. In the bottom panel the densities are plotted on a linear scale, to show clearly how the densities of silicon and sulphur are rather strongly peaked, near 13,000 km s^{-1} in the model. In Fig. 4, allowance has been made for the decay of ^{56}Ni and ^{56}Co for 12 days; i.e., this plot corresponds to an epoch between -8 and -10 days if the SN 1997br rise time to maximum light was between 20 and 22 days.

In model CS15DD3, the outer edge of the iron–peak core is around 12,000 km s^{-1}, consistent within our errors with the 12,500 km s^{-1} that we infer for SN 1997br from spectroscopy. Stable ^{54}Fe and ^{58}Ni extend outwards to higher velocities, and coexist with silicon and sulphur. This too is qualitatively consistent with our interpretation of the spectra discussed above. A possible problem, though, is that in this particular model the ^{58}Ni may not extend sufficiently farther out in velocity space than the ^{56}Co from ^{56}Ni decay, i.e., the model as it stands probably can not account for Ni III

Fig 4

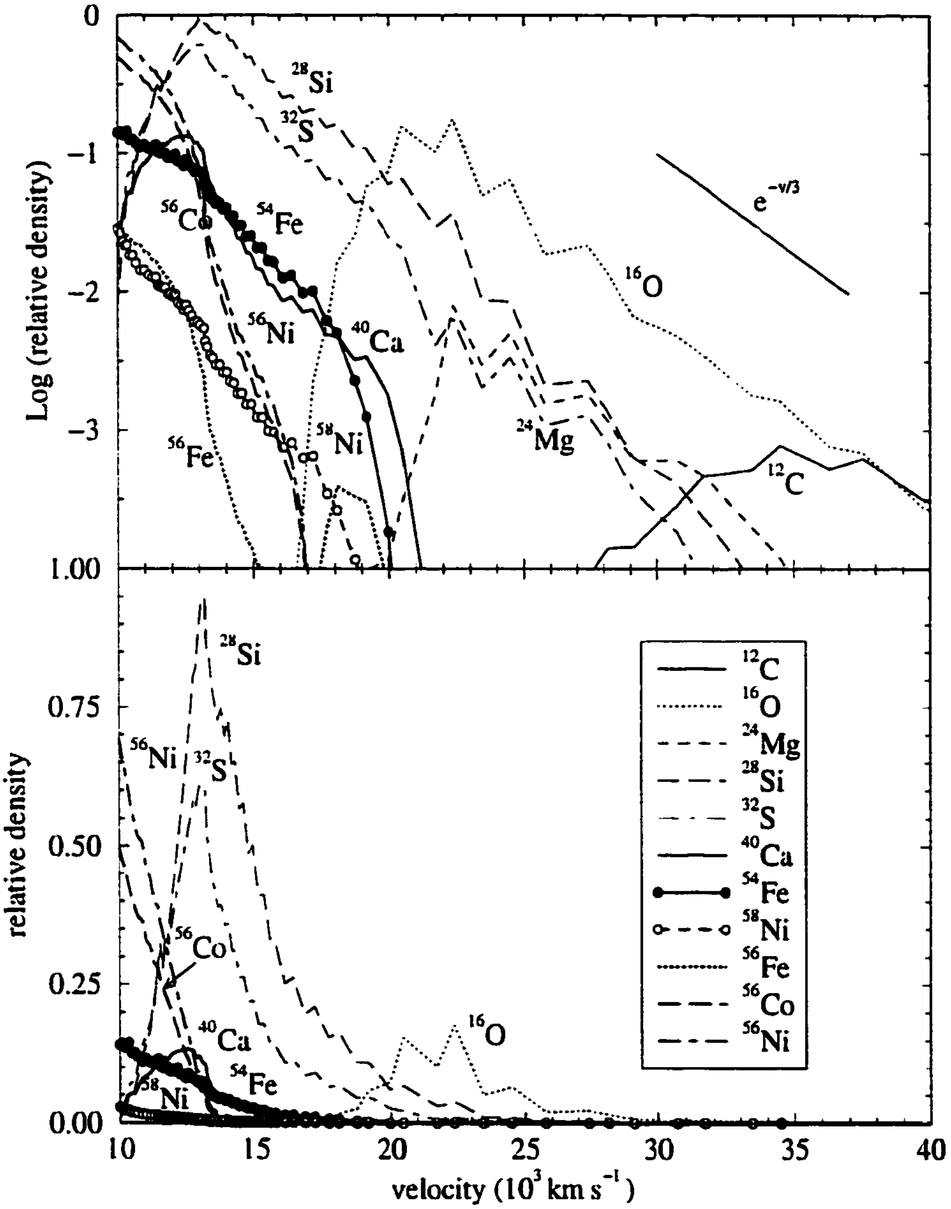

Figure 5.4: The relative densities of selected isotopes in the outer layers of the Chandrasekhar-mass, delayed-detonation model C15DD3 (Iwamoto et al. 1999) are plotted against velocity, for 12 days after explosion, on both logarithmic (upper panel) and linear (lower panel) scales. The straight line in the upper panel corresponds to $v_e = 3000$ km s^{-1}.

lines without Co III lines in the pre-maximum spectra. It should be mentioned, however, that a higher assumed metallicity for the white dwarf progenitor would lead to higher abundances of ^{54}Fe and ^{58}Ni in the high-velocity layers (Höflich, Wheeler, & Thielemann 1998).

It has been shown (Höflich 1995; Nugent et al. 1995a,b, 1998; Wheeler et al. 1998) that detailed NLTE spectra calculated for certain SN Ia hydrodynamical models that eject about 0.6 $M_\odot$ of ^{56}Ni resemble the observed spectra of normal SNe Ia. Such detailed spectrum calculations should now be carried out for more powerful models such as CS15DD3, for comparison with the observed spectra of SN 1991T-like events. Hydrodynamical models like CS15DD3, but with higher initial metallicity, also should be constructed. (In addition to causing the synthesis of more ^{54}Fe and ^{58}Ni, the higher metallicity also would have a direct effect on the spectra of the models, especially before the time of maximum-brightness [Höflich et al. 1998; Lentz et al. 2000a].)

In addition to the evidence for slowly moving carbon in SN 1991T, and the apparent overluminosity of SN 1991T, there is another line of evidence that is difficult to interpret in the paradigm that SN 1991T-like events are just the hot end of a continuous sequence of SNe Ia. Fig. 5 shows the blueshift of the red Si II absorption feature plotted against epoch for SNe 1991T, 1997br, and several other well observed SNe Ia. The two events that have the lowest blueshifts in post-maximum brightness spectra, SNe 1986G and 1991bg, were peculiar weak events; all of the others apart from SNe 1991T and 1997br were spectroscopically normal. (Such diagrams have been published before, e.g., Branch & van den Bergh [1993]). If SNe 1991T and 1997br were simply at the hot, powerful end of a continuous sequence of SNe Ia, we would expect their Si II blueshifts to be higher than in normal SNe Ia. But in Fig. 5, SN 1997br is not exceptionally high compared to normal SNe Ia (even ignoring the exceptionally fast SNe 1983G and 1984A [Branch 1987a], which had all the usual SN Ia spectral features and whose very high blueshifts remain unexplained). SN 1991T falls *below* the normals. This seems to be inconsistent with model CS15DD3 in particular and with the continuous-sequence hypothesis in general. It is not necessarily inconsis-

Fig 5

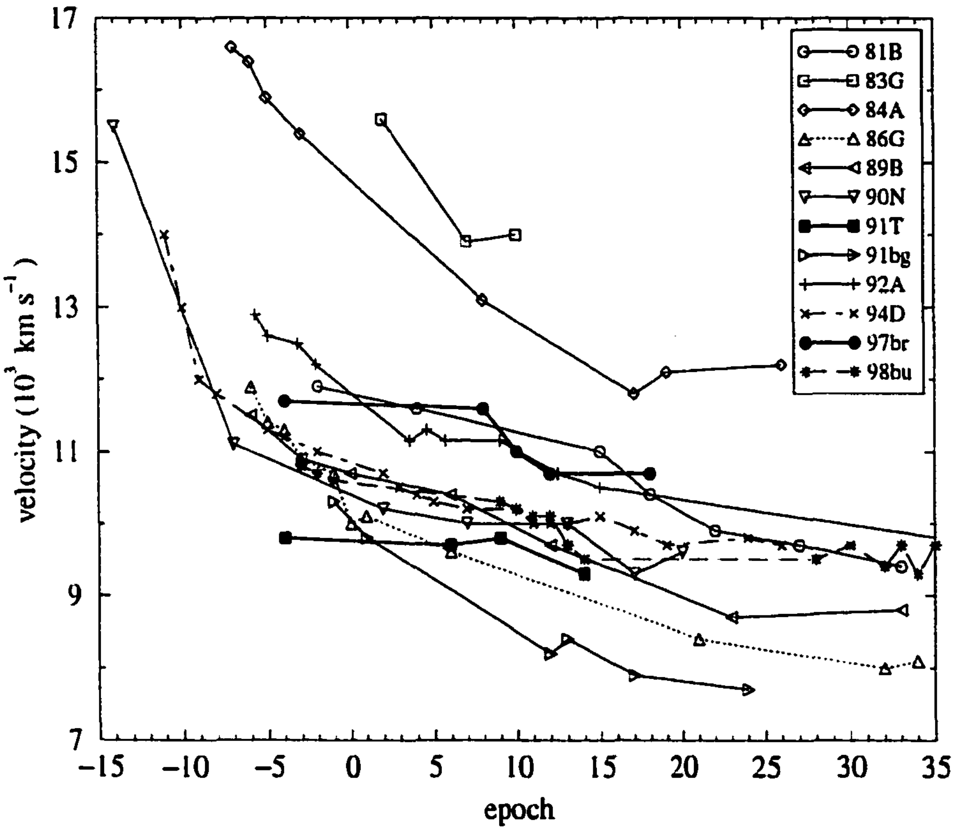

Figure 5.5: The velocity corresponding to the blueshift of the red Si II absorption is plotted against epoch for SNe 1997br, 1991T, and several other well observed SNe Ia.

tent with the scenario proposed by FBHB (see also Ruiz–Lapuente et al. 1992), that in SN 1991T-like events the intermediate–mass elements were compressed between a rapidly expanding iron–peak core and some external mass — perhaps a carbon–oxygen layer surrounding the central portions of a merger of two white dwarfs.

5.4 Conclusion

The lack of evidence for low–velocity C II absorption in the spectra of SN 1997br, and the recognition that the Fe III and Ni III lines of SNe 1997br and 1991T might have been produced by freshly synthesized ^{54}Fe and ^{58}Ni (rather than by ^{56}Ni and ^{56}Fe) have motivated us to consider whether SN 1991T–like events could simply be at the hot end of a continuous sequence of SNe Ia. In general terms, the composition structure of the strong delayed–detonation model CS15DD3 of Iwamoto et al. (1999) could be compatible with the spectra of SN 1991T-like events in some respects, and the composition structure of a model computed for a higher initial metallicity might be better still. Detailed NLTE spectra of models such as CS15DD3 should be calculated for comparison with spectra of SN 1991T–like events.

Nevertheless, the evidence for low-velocity carbon in SN 1991T, the apparent overluminosity of SN 1991T, and as discussed above, the low blueshift of Si II lines in SN 1991T–like events (especially SN 1991T itself), favor the hypothesis that SN 1991T–like events, including SN 1997br, are a discrete subgroup of SNe Ia, possibly involving super–Chandrasekhar mass ejection from a double–degenerate merger. Determining the true nature of SN 1991T–like events will require further observations, especially at very early times, more calculations of hydrodynamical models, and further spectroscopic analysis.

It is our pleasure to thank Darrin Casebeer, Dean Richardson, and Thomas Vaughan for helpful discussions. This work was supported by NSF grant AST-9731450 and NASA grant NAG5-3505.

Chapter 6

Spectral Analysis of the Sub–Luminous Type Ia SNe

In the previous chapter, we have analyzed the spectra of the peculiar, over–luminous and powerful type Ia supernova SN 1997br. We have also discussed about the nature of these powerful and hot SNe Ia. In this chapter, we shall provide the spectral analysis of the sub–luminous, weak and cool type Ia SNe 1991bg and 1999by, the opposite extreme of the peculiar SNe Ia. This chapter consists of two portions. The first portion shall present a SYNOW analysis for each observed spectrum. The second portion shall present an analysis of the "580 nm Si II" feature seen in the spectra of SNe Ia. We shall show that an analysis of this feature is very useful to understand the spectral sequence pointed out by Nugent et al. (1995a). Then, we shall argue that the composition structure of these sub–luminous SNe Ia is not fundamentally different from that of normal SNe Ia. We shall prove that the cool temperature is the cause of most of the peculiarities seen in these sub–luminous SNe Ia.

6.1 Sub–Luminous Type Ia SNe

In this section, we shall present an analysis of the spectra of the sub–luminous type Ia SNe 1991bg and 1999by. For each observed spectrum, a SYNOW analysis shall be given. v_{phot} represents the photospheric velocity. v_{max} is the maximum velocity for the calculation. And, T_{bb}, the blackbody temperature, determines the continuum of each SYNOW fit. And, the fitting parameters for each ion shall be given in tables. For all tables, λ, in the unit of Å, means the wavelength of the reference line of each ion used in the SYNOW calculation. λ is given only once in this entire chapter (i.e. λ is given the first time an ion appears in this chapter. After that, λ for that ion shall be omitted). τ represents the line optical depth of the reference line for each ion. The velocity interval within which an ion is used is between v_{min} and v_{max}, both in the unit of 10^3 km s^{-1}. When no v_{min} is given, the minimum velocity equals the photospheric velocity. v_e represents the e-folding velocity, in the unit of 10^3 km s^{-1}, that determines the exponential radial dependence of the line optical depths. T_{exc} is the excitation temperature, in the unit of 10^3 K, that determines the optical depths of other lines for each ion by using the Boltzmann excitation.

6.1.1 SN 1991bg

ion	Ca II	O I	Si II	Ti II	S II	Mg I	Mg II
λ	3934	7772	6347	3349	5454	5184	4481
τ	40	1.5	2.0	50	0.5	1.2	2.5
v_{min}	...	10.5	...	...	...	11	11
v_{max}	40	15	15	40	11	13	13
v_e	3.0	3.0	3.0	3.0	3.0	3.0	3.0
T_{exc}	12	12	12	12	12	12	12

Table 6.1: Fitting Parameters for Figure 1

Fig. 1 presents an analysis of a spectrum of SN 1991bg, that is 13 days after the explosion. This supernova is the classical example of the sub–luminous SNe Ia.

Some of the important fitting parameters are as follows: v_{phot} = 9,000 km s^{-1}, v_{max} = 40,000 km s^{-1}, and T_{bb} = 16,000 K. Fitting parameters for each ion are shown in Table 1.

This spectrum is near the maximum brightness. In these sub–luminous SNe Ia, it is well–known that the rise time to the maximum brightness is short. As previously has been pointed out, the blue part of this spectrum is dominated by Ti II transitions. The maximum velocity of Si II is determined very well by fitting the Si II λ6355 feature. This maximum velocity is close to what the model W7 (Nomoto et al. 1984, Branch et al. 1985) predicts. The "580 nm Si II" feature is deep as expected from the spectral sequence found by Nugent et al. (1995a). In the next section, we shall present a detailed analysis of this feature, which is actually a blend of the Si II line near 5800 Å and many weak Ti II transition lines. The maximum velocity of S II is only 11,000 km s^{-1}. The shape of the S II "W" feature near 5400 Å is very sensitive to the maximum velocity of S II. A feature near 5000 Å is attributed to Mg I λ5184 which is a new line identification. The velocity interval of Mg I is same as the velocity interval of Mg II, which is an interesting result. Finally, the detachment of O I also helps to improve the fit.

6.1.2 SN 1999by

ion	Ca I	Ca II	O I	Si II	Ti II	S II	Na I	Mg II	Mg I
λ	4227	—	—	—	—	—	5890	—	—
τ	1	20	1.8	2.0	50	2.2	0.2	1.0	0.5
v_{min}	...	...	...	...	...	...	...	11	11
v_{max}	40	40	40	15	16	11	40	15	13
v_e	3.0	3.0	3.0	3.0	3.0	3.0	3.0	3.0	3.0
T_{exc}	12	12	12	12	12	12	12	12	12

Table 6.2: Fitting Parameters for Figure 2

Fig. 2 presents an analysis of a spectrum of SN 1999by, that is 3 days before the

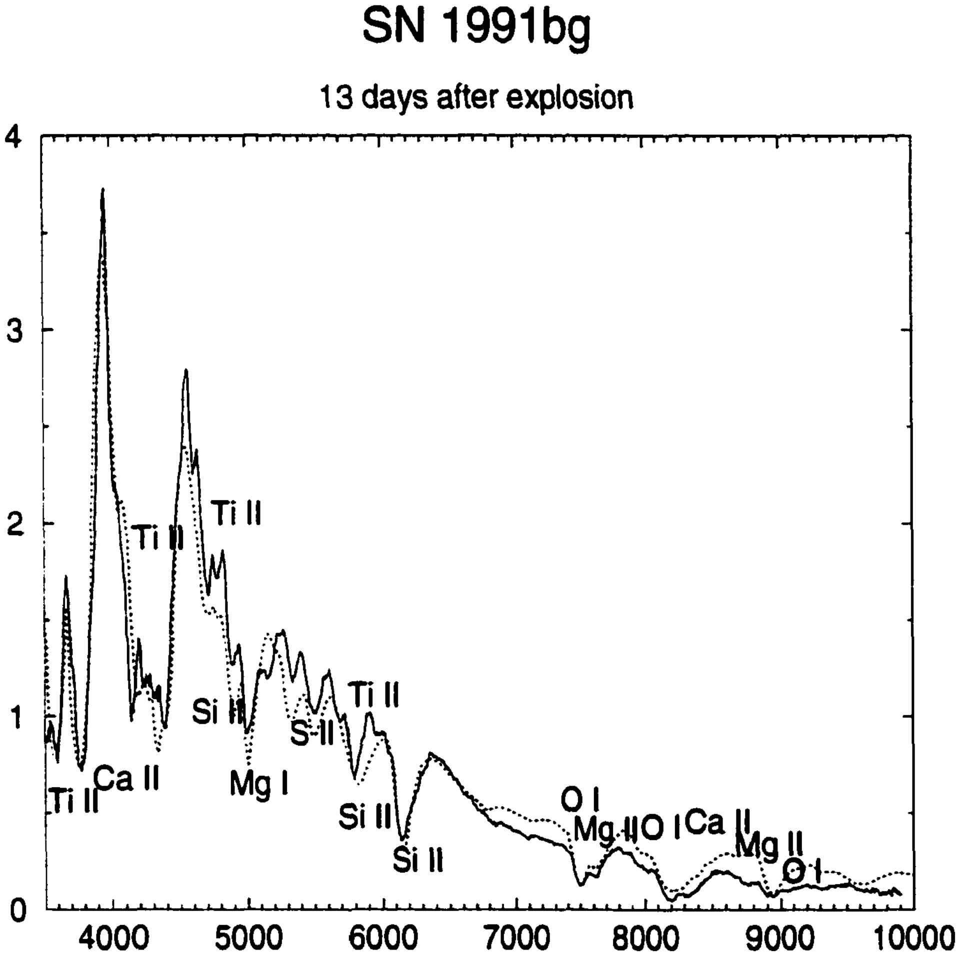

Figure 6.1: The observer is unknown.

maximum light. Some of the important fitting parameters are as follows: v_{phot} = 10,000 km s^{-1}, v_{max} = 40,000 km s^{-1}, and T_{bb} = 12,000 K. Fitting parameters for each ion are shown in Table 2.

This spectrum is very similar to the previous spectrum for SN 1991bg near the maximum light. The blue part of the spectrum is dominated by Ti II, which also strongly contributes to the depth of the "580 nm Si II" feature. Here, we have found that putting a relatively slow maximum velocity of Ti II helps to improve the fit. The velocity intervals for Si II, S II, Mg I, and Mg II are very similar to those what we've found in Fig. 1 for SN 1991bg. Once again, the Mg I feature near 5000 Å is very conspicuous. The S II feature which was W-shaped in Fig. 1 has only one absorption line in this figure. This is a very good indication of the very narrow velocity interval of S II.

ion	Ca I	Ca II	O I	Si II	Ti II	S II	Na I	Mg II	Fe II
λ	—	—	—	—	—	—	—	—	5018
τ	2	40	1.8	2.5	400	1.0	0.2	1.0	1.0
v_{min}	...	...	...	...	...	...	...	11	...
v_{max}	40	40	40	15	16	11	40	15	40
v_e	3.0	3.0	3.0	3.0	3.0	3.0	3.0	3.0	3.0
T_{exc}	10	10	10	10	10	10	10	10	10

Table 6.3: Fitting Parameters for Figure 3

Fig. 3 presents an analysis of a spectrum of SN 1999by, that is 3 days after the maximum light. Some of the important fitting parameters are as follows: v_{phot} = 9,500 km s^{-1}, v_{max} = 40,000 km s^{-1}, and T_{bb} = 10,000 K. Fitting parameters for each ion are shown in Table 3.

Like previous figures, Ti II lines continue to be very strong. But, now, Fe II lines have started to contribute to some of the features. The "W" S II feature now has two absorptions and is actually W-shaped. This is because, as v_{phot} slows down, the velocity interval of S II has become wider. It is interesting to see that the synthetic Ca II H&K feature is somewhat faster than the observed H&K line. This implies that

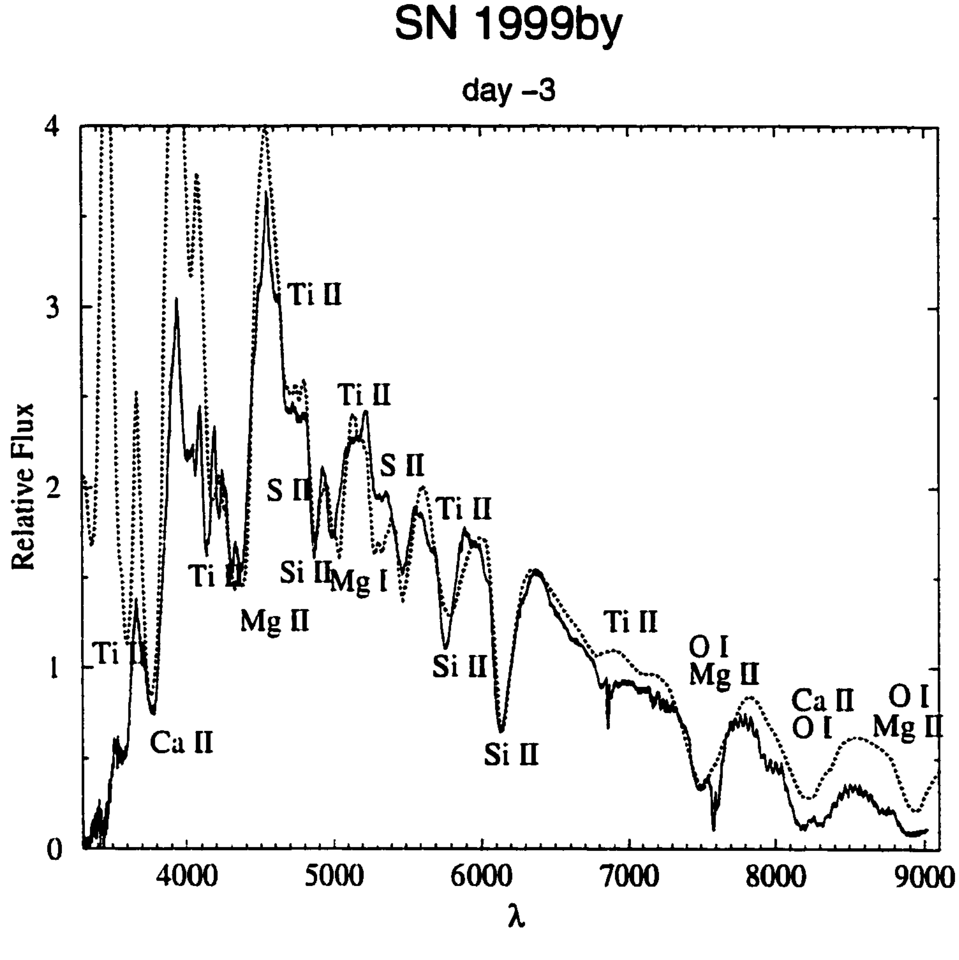

Figure 6.2: The observed spectrum is from Bonanos et al. (2000).

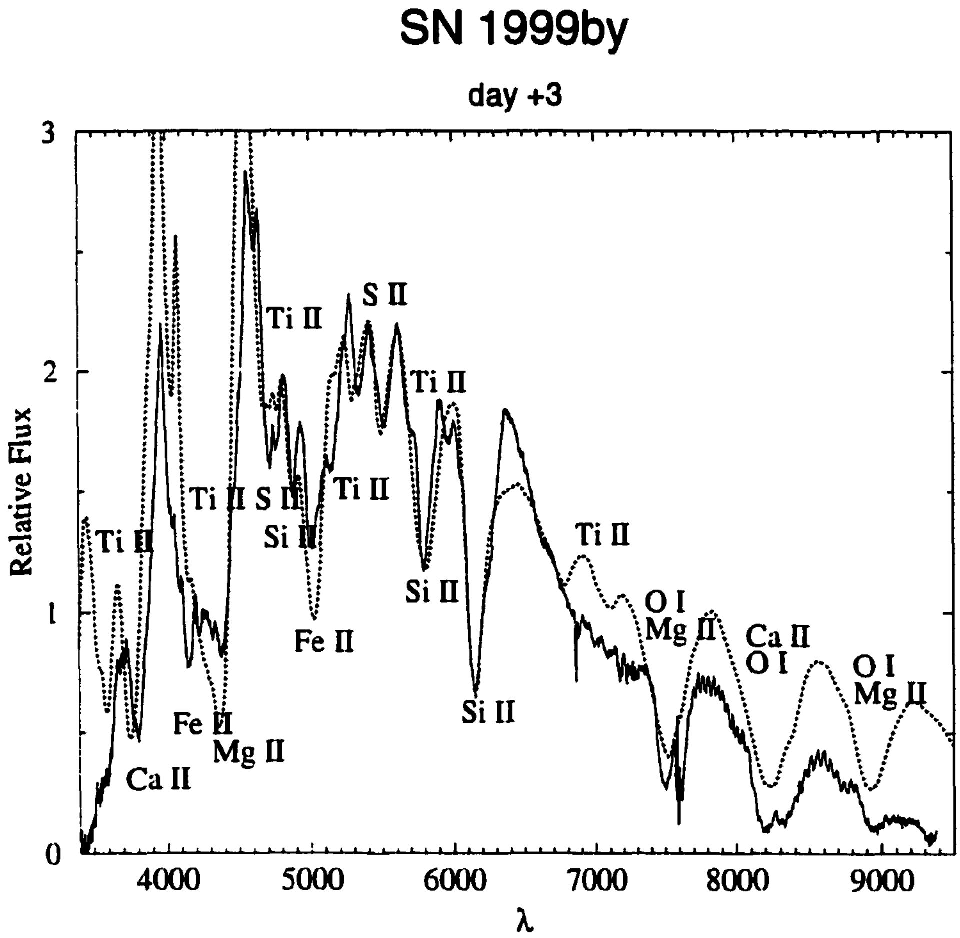

Figure 6.3: The observed spectrum is from Bonanos et al. (2000).

the actual v_{phot} may be slower than what we've found by fitting other features. If so, it may be necessary to detach some of other ions.

Fig. 4 presents an analysis of a spectrum of SN 1999by, that is 6 days after the maximum light. Some of the important fitting parameters are as follows: v_{phot} = 9,500 km s^{-1}, v_{max} = 40,000 km s^{-1}, and T_{bb} = 9,000 K. Fitting parameters for each ion are shown in Table 4.

The blue part of this spectrum is now dominated by Ti II and Fe II. The synthetic Ca II H&K line is somewhat faster than the observed H&K line again, which may indicate the smaller value of v_{phot}. The feature near 6000 Å can be attributed to a

ion	Ca I	Ca II	O I	Si II	Ti II	S II	Fe II
τ	5	40	1.8	2.8	400	1.0	5.0
v_{min}	...	...	...	...	...	...	...
v_{max}	40	40	40	15	16	10	40
v_e	3.0	3.0	3.0	3.0	3.0	3.0	3.0
T_{exc}	9	9	9	9	10	9	9

Table 6.4: Fitting Parameters for Figure 4

Ca I transition. Another Ca I line is also contributing to the red edge of the Si II $\lambda6355$ feature. Because Ca I lines are strong, the temperature of this spectrum must be very cool. The synthetic spectrum has some problems near 5500 Å, which are unexplained at this point.

ion	O I	O II	Ca II	O I	Si II	Ti II	Na I	Fe II	Fe II
λ	—	7321	—	—	—	—	—	—	—
τ	1.5	0.6	40	1.5	1.6	400	0.8	1.0	10
v_{min}	10	...	...	10	8	...	11	10	...
v_{max}	40	30	15	40	15	16	14	40	10
v_e	3.0	30.0	3.0	3.0	3.0	3.0	3.0	3.0	3.0
T_{exc}	6	5	5	4.6	5	5	5	5	5

Table 6.5: Fitting Parameters for Figure 5

Fig. 5 presents an analysis of a spectrum of SN 1999by, that is 25 days after the maximum light. Some of the important fitting parameters are as follows: v_{phot} = 6,000 km s^{-1}, v_{max} = 40,000 km s^{-1}, and T_{bb} = 5,000 K. Fitting parameters for each ion are shown in Table 5.

In this spectrum, v_{phot} was determined by fitting the Ca II H&K line. As a result, many other ions had to be detached. Si II is now detached at 8,000 km s^{-1}, but the fit to the $\lambda6355$ feature is not very good. The blue part of the spectrum is dominated by Ti II and Fe II, and the fit is very good. In particular, a very interesting feature attributed to Fe II can be seen near 5000 Å, which is called the "Hβ" feature by Fisher (2000). As Fisher has discussed, two components of Fe II are necessary to

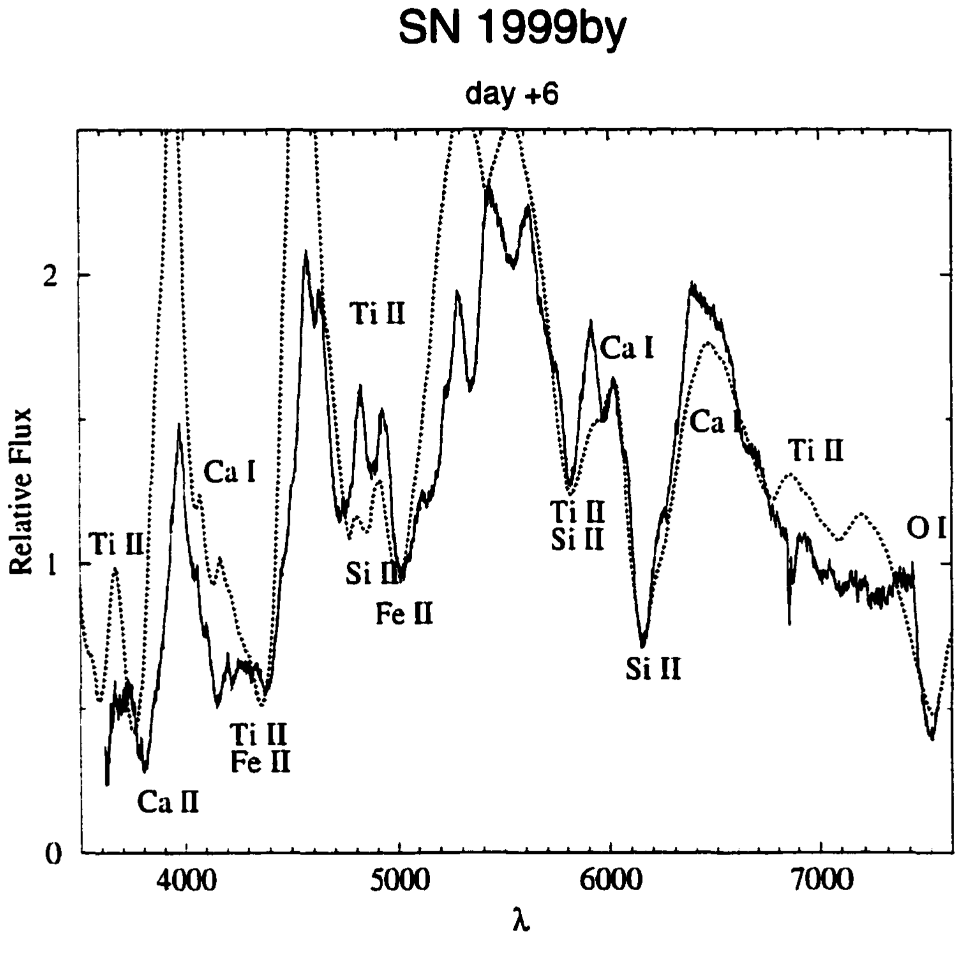

Figure 6.4: The observed spectrum is from Bonanos et al. (2000).

reproduce this feature. In the synthetic spectrum, a discontinuity of the optical depth is introduced at 10,000 km s^{-1}, which is an outer edge of the iron core. The Na I feature near 5700 Å is unusually narrow. This may be due to the emission peak just blue of this feature. But, if not, this gives an interesting constraint to the explosion mechanism of this kind of supernova. The red part of the spectrum is dominated by oxygen. In the synthetic spectrum, the forbidden O II transitions are used to fit the broad feature near 7000 Å. Like Fisher et al. (1999) has done, we had to use a very large value of v_e for this ion. Finally, an absorption feature near 5400 Å can be attributed to an O I transition. We have used a unique value of T_{exc} for this ion to show the forbidden O I feature near 6100 Å. Near this temperature range, this feature become stronger very quickly even by a tiny temperature drop.

6.1.3 Summary

By analyzing the spectra of the sub–luminous SNe Ia 1991bg and 1999by, we have found only normal SN Ia elements. In normal SNe Ia, most of these elements are singly ionized. But, in the cases of the sub–luminous SNe Ia, some of these elements are neutral due to the cool temperature. As a result, we have found the evidence of Mg I and Ca I. The lines of Ti II are not normally seen in the spectra of normal SNe Ia. But, as we shall show in the next section, this is due to the hotter temperature. Therefore, the composition structure of these sub–luminous SNe Ia is not fundamentally different from that of normal SNe Ia. The difference is the temperature and the velocity interval for some of the elements. In the next section, we shall show that most of the peculiarities found in these sub–luminous SNe Ia can be explained by the cool temperature.

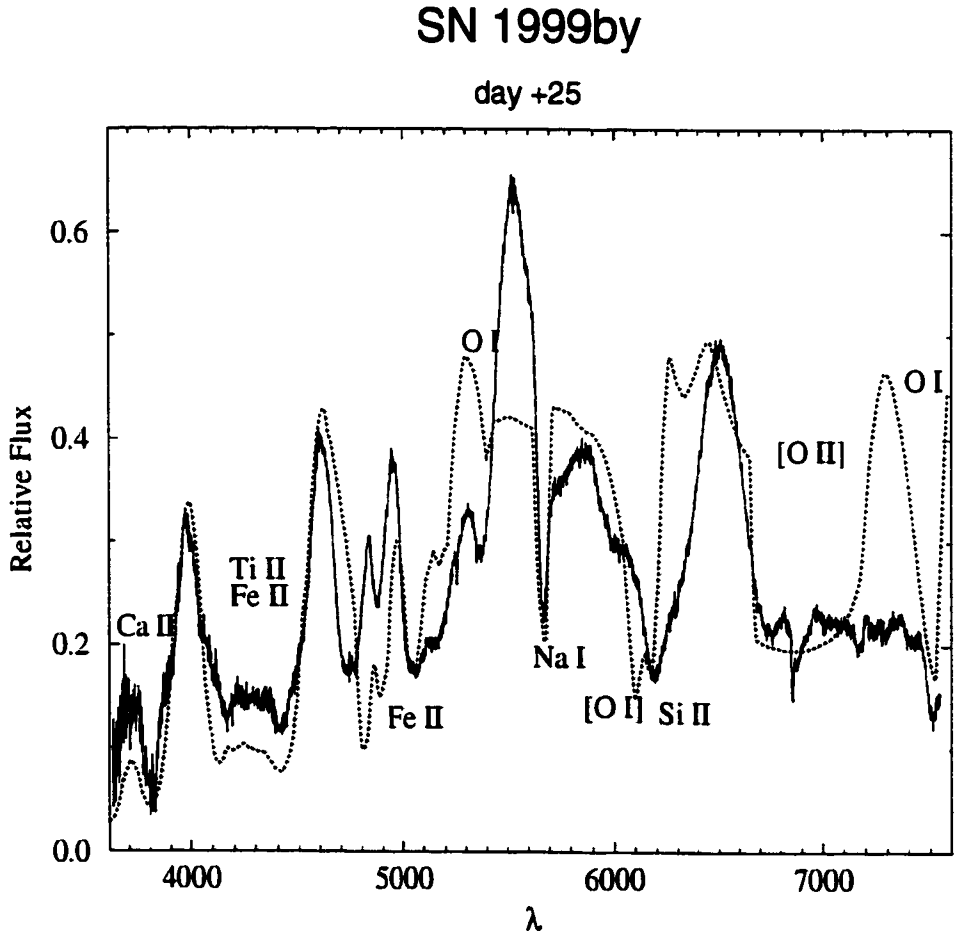

Figure 6.5: The observed spectrum is from Bonanos et al. (2000).

6.2 Analysis of the 580 nm Feature

Nugent et al. (1995a) showed that there is a spectroscopic sequence among SNe Ia. They pointed out several spectral evolutions, and proved that most of these evolutions can be explained by temperature. But, one unsolved mystery has been provided. There are two Si II lines around 600 nm: one is near 615 nm and another is near 580 nm. Nugent et al. found out that the depth of the 580 nm line relative to the depth of the 615 nm line becomes deeper as the temperature becomes cooler. In other words, the relative depth of the 580 nm feature is deeper in the spectra of sub–luminous SNe Ia such as SNe 1991bg and 1999by. This is opposite to the expectation because the excitation potential of the 580 nm line is higher than that of the 615 nm line. Therefore, the relative depth of the 580 nm line should not be deeper in the spectra of sub–luminous SNe Ia. In this section, we shall show that the 580 nm Si II line is actually blended with many weak Ti II lines. And as the temperature becomes cooler, the optical depths of these Ti II lines become larger. As a result, the "580 nm" feature becomes deeper in the spectra of cooler SNe Ia.

6.2.1 The 580 nm Feature and the Depth Ratio

Fig. 6 presents the spectral evolution of the 580 nm feature as a function of the optical depth of Ti II ($\tau_{Ti\ II}$). These are SYNOW synthetic spectra which use only two ions: Si II and Ti II. When $\tau_{Ti\ II} = 0$, only Si II lines are used. In these synthetic spectra, only the value of $\tau_{Ti\ II}$ has been varied. It is obvious that there are Ti II lines everywhere. But, as $\tau_{Ti\ II}$ becomes larger, the 580 nm feature becomes deeper. Therefore, there are Ti II lines near the 580 nm Si II feature.

There is another way of making this 580 nm feature deeper. Fig. 7 presents the spectral evolution of this feature as a function of the excitation temperature of ions. In these SYNOW synthtic spectra, the value of $\tau_{Ti\ II}$ has been kept constant at a relatively large value. Instead, the excitation temperature of ions has been varied. In the blue part of the spectra, the variation is small. This is because the excitation

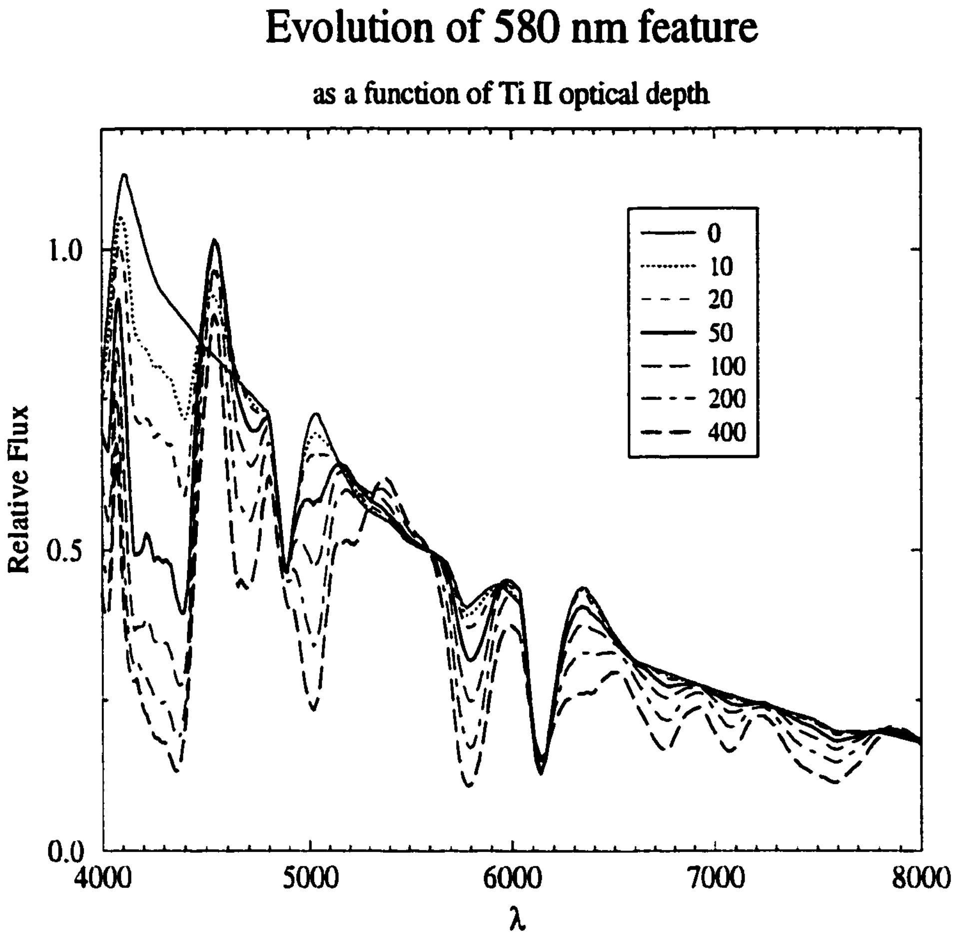

Figure 6.6:

potential of those Ti II line are close to the excitation potential of the Ti II reference line in the synthetic spectra. But, it is obvious that the 580 nm feature is very sensitive to the temperature change. One reason is that the 580 nm Si II line has a higher excitation potential. In addition to this fact, the excitation potential of Ti II lines near this feature is also higher compared to the excitation potential of blue Ti II lines. Therefore, the 580 nm feature becomes deeper at higher temperature. But, these high temperatures are not very realistic because $\tau_{Ti\ II}$ should be relatively small at such high temperatures.

Now, we shall discuss about the "Si II" depth ratio. Fig. 8 illustrates the way of measuring the ratio. Following the definitions used by Nugent et al. (1995a), the

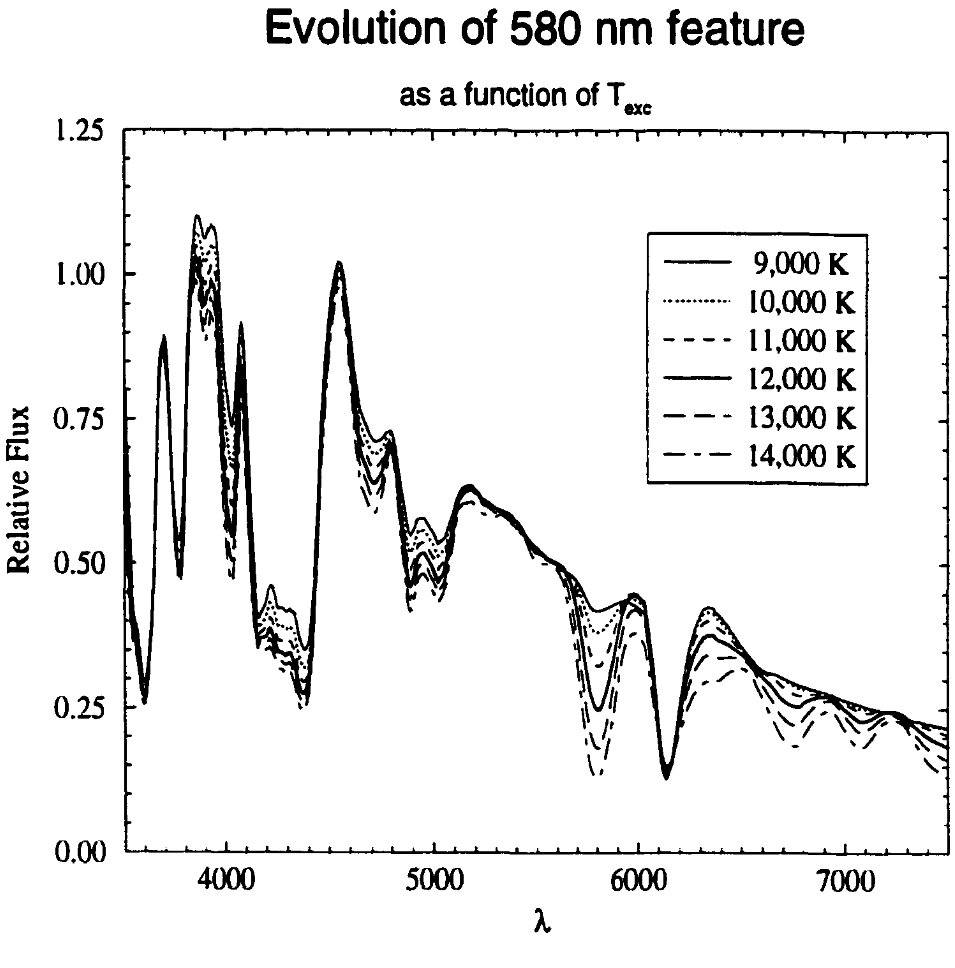

Evolution of 580 nm feature
as a function of T_{exc}
1.25
1.00
0.75
0.50
0.25
0.00
Relative Flux
4000
5000
6000
7000
λ
9,000 K
10,000 K
11,000 K
12,000 K
13,000 K
14,000 K

Figure 6.7:

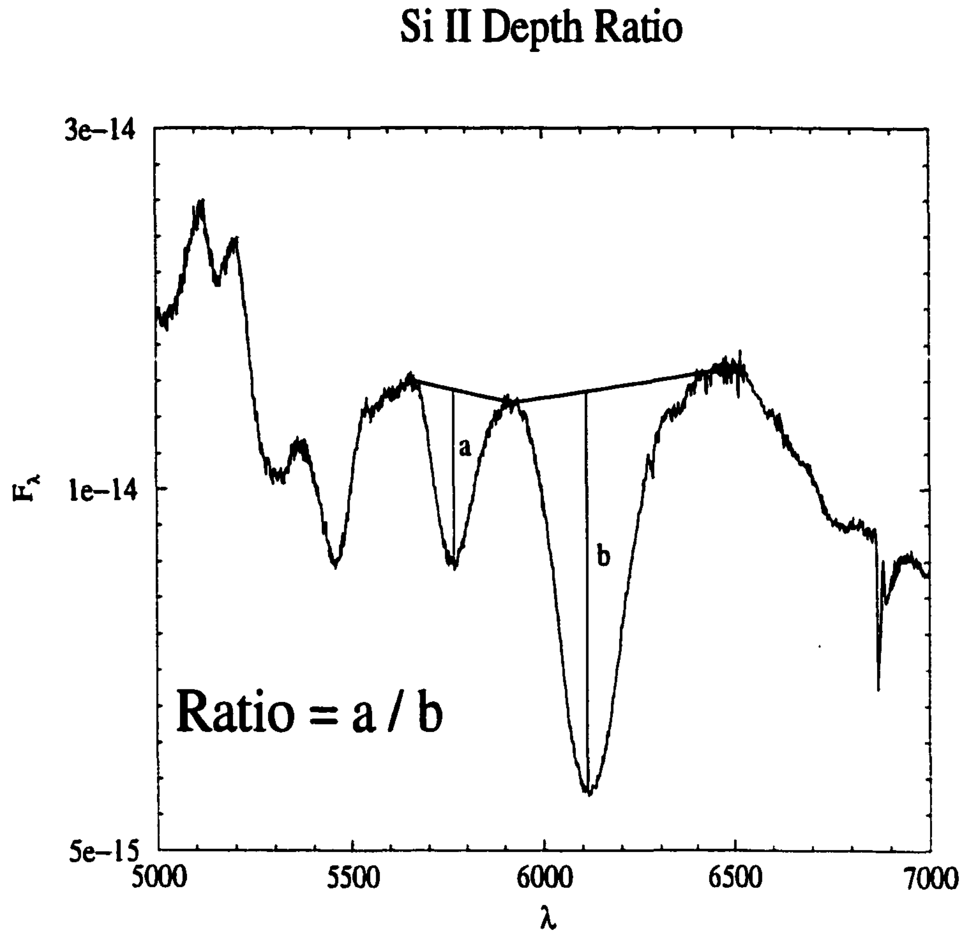

Figure 6.8:

flux should be in F_λ. Then, a continuum line should be drawn over each "Si II" feature (the 580 nm feature and the 615 nm feature). Then, a vertical line should be drawn from the bottom of a feature to the line of the continuum. This vertical line represents the depth of a Si II feature. The depth ratio is simply the ratio of these two depths.

Fig. 9 compares the theoretical depth ratios to the observed depth ratios. These theoretical ratios were calculated from the SYNOW synthetic spectra that have varied only $\tau_{Ti\ II}$. The observed ratios for the sub–luminous SNe Ia, 1991bg and 1999by, fit with the theoretical ratio somewhere between $\tau_{Ti\ II} = 50$ and $\tau_{Ti\ II} = 100$ in the model ratio curve. The observed ratio for a somewhat peculiar SN 1986G (see

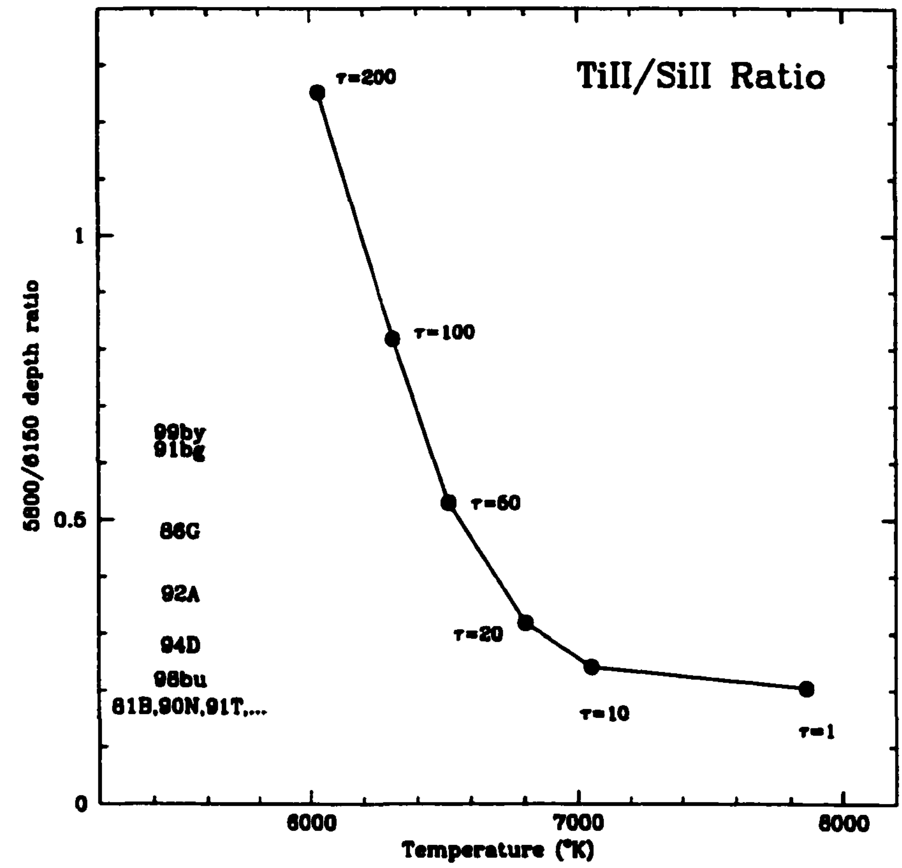

Figure 6.9: This figure is created by Peter Garnavich.

the next chapter for its spectral analysis) is close to the model ratio for $\tau_{Ti\ II} = 50$. Then, the case of SN 1992A is somewhere between $\tau_{Ti\ II} = 20$ and $\tau_{Ti\ II} = 50$. The cases of other SNe are located below $\tau_{Ti\ II} = 20$. As the temperature becomes hotter, the effect of Ti II lines becomes very small. As a result, many hotter SNe are concentrated in a very small range of $\tau_{Ti\ II}$.

Fig. 10 compares the theoretical depth ratios to the observed depth ratios, now, by assuming that the model value of Δm_{15} is proportional to the temperature. As we shall show in the next chapter, Δm_{15} is a very good indication of the temperature of SNe Ia. Some SNe have more than one depth ratio from different epochs. The model depth curve fits with observed data points very well. When the value of Δm_{15}

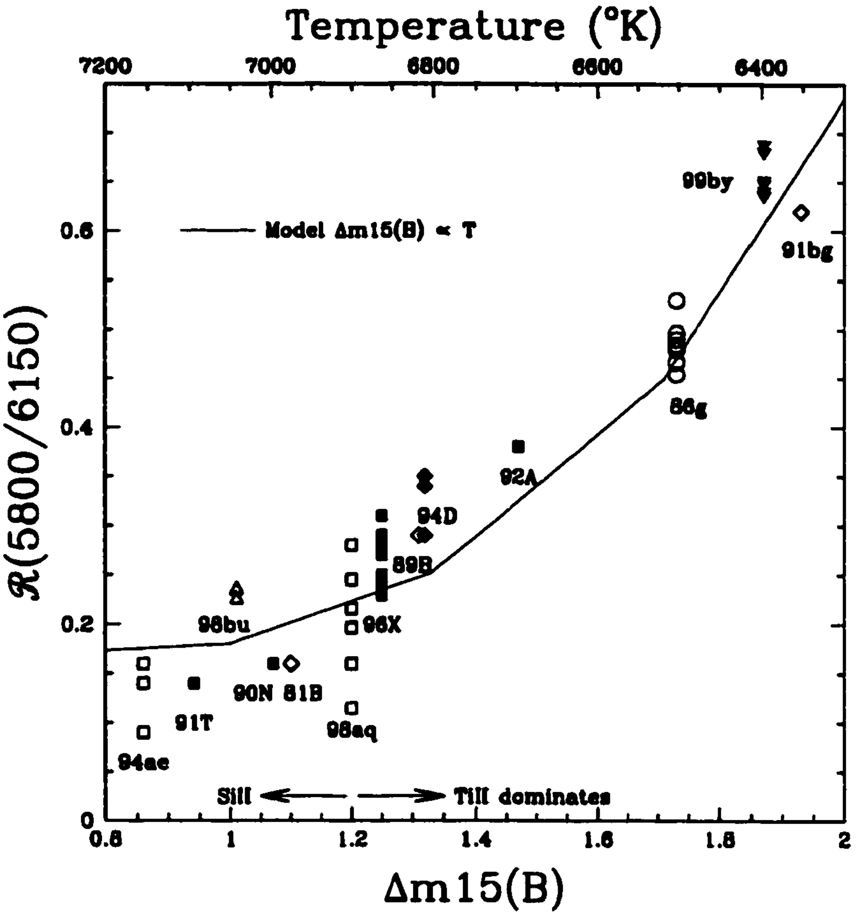

Figure 6.10: This figure is created by Peter Garnavich.

is larger than 1.2, Ti II lines start to dominate the 580 nm feature. When the value of Δm_{15} is smaller than 1.2, the feature is mostly attributed to the 580 nm Si II line. This gives a very tight relationship between Δm_{15} and the depth ratio. This relationship is used to increase the statistical data points in Hatano et al. (2000b), who discuss the spectroscopic diversity among SNe Ia.

Fig. 11 compares the theoretical B-V color to the observed B-V color of SNe Ia. As the figure shows, it is well-known that the color of SNe becomes redder as the value of Δm_{15} becomes larger. This is another peculiarity seen in the sub-luminous SNe Ia, 1991bg and 1999by. The theoretical color is, once again, calculated from the SYNOW synthetic spectra that have varied only $\tau_{Ti\ II}$. The model curve fits with

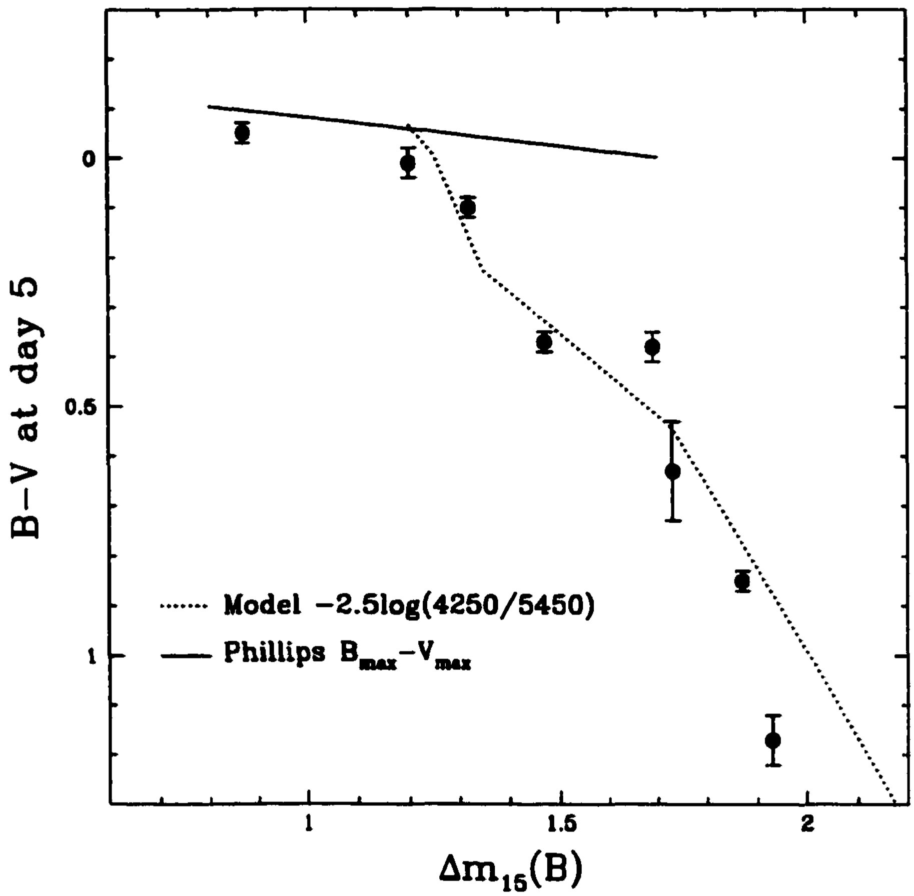

Figure 6.11: This figure is created by Peter Garnavich.

the observations very well. There are many strong Ti II lines near 4250 Å as we have seen earlier in this chapter. Therefore, the flux of this color band becomes lower as the Ti II lines become stronger at the cool temperature. As a result, the B-V color becomes redder as the temperature becomes cooler.

6.2.2 Ti II Lines

We have shown that there are many Ti II lines near the 580 nm Si II feature. And, these Ti II lines strongly contribute to the depth of the 580 nm feature at the cool temperature. Now, we shall analyze the behaviors of these Ti II transitions. Fig. 12

compares the velocity inferred from the minimum of two "Si II" absorption features: one is the 615 nm feture (attributed to λ6355) and another is the 580 nm feature (attributed to λ5972). We compare the velocity of two SNe Ia, 1994D (a normal SN Ia) and 1999by (a sub-luminous SN Ia). The velocity is in the unit of 10^3 km s^{-1}, and the epoch is in the unit of day in which day 0 means the day of the maximum brightness. As expected, the velocity of SN 1999by is, in general, slower than the velocity of SN 1994D. The velocity curves inferred from the 615 nm feature of each supernova are smoothly decreasing. This is because this feature is almost entirely attributed to Si II λ6355, although there are some weak S II lines near this feature. This is why this feature is often used to derive the velocity at the photosphere. On the other hand, the velocity curves inferred from the 580 nm feature are not smoothly decreasing. In the case of SN 1999by, the velocity inferred from the 580 nm feature is very close to the velocity inferred from the 615 nm feature before the time of the maximum brightness. However, after the time of the maximum brightness, the velocity inferred from the 580 nm feature decreases much more quickly than the velocity inferred from the 615 nm feature does. This is because, before the time of the maximum brightness, most of the 580 nm feature may be attributed to Si II λ5972. Thus, the velocity of both features at this time represents the velocity of Si II (those data points are close each other). But, after the time of the maximum brightness, the 580 nm feature is contaminated by redder lines (Ti II lines). As a result, the velocity inferred from the 580 nm feature is slower than the velocity inferred from the 615 nm feature after the time of the maximum brightness. In the case of SN 1994D, the velocity inferred from the 580 nm feature sometimes decreases, but sometimes increases. Around the time of the maximum brightness, the velocity of both features are close each other; thus, both represent the velocity of Si II. But, after the time of the maximum brightness, the velocity inferred from the 580 nm feature becomes much faster than the velocity inferred from the 615 nm feature. This is because the 580 nm feature is, in the case of this supernova, contaminated by bluer lines (Na I lines), and eventually become the Na I line. In the case of SN 1999by, these Na I

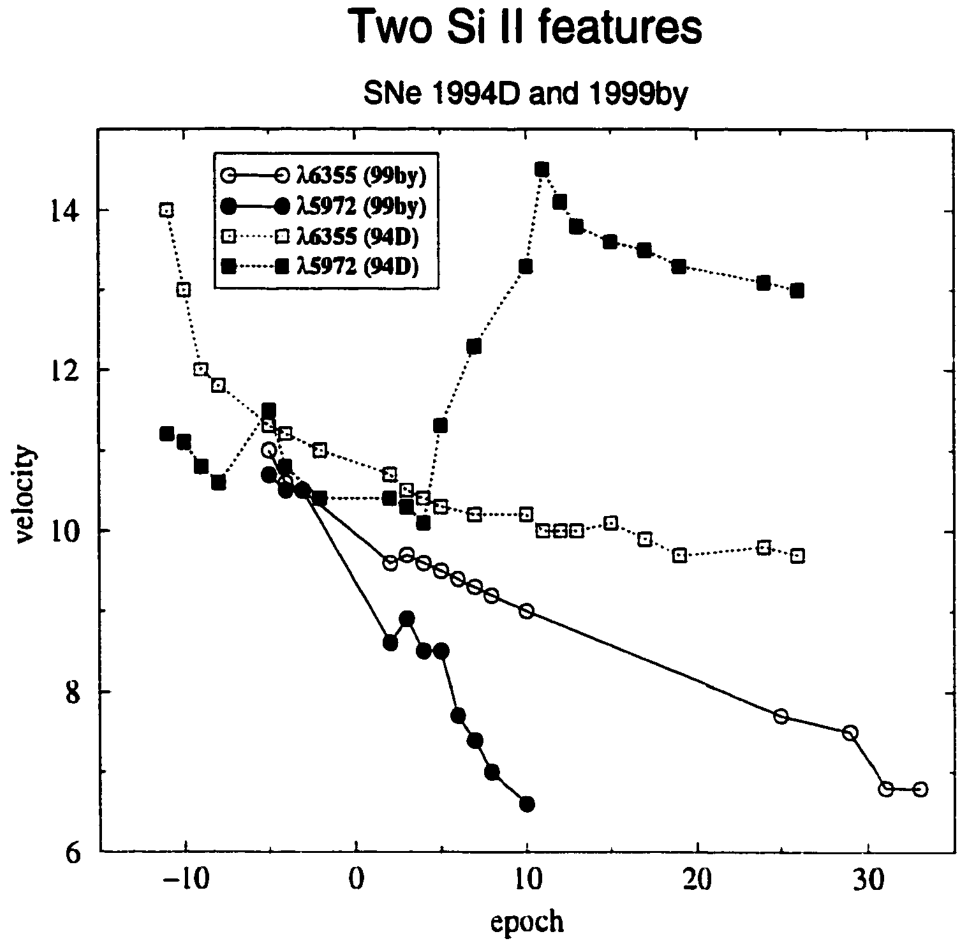

Figure 6.12:

lines are not very strong (see the previous section). Instead, Ti II lines dominate this feature.

Table 6 lists the 10 strongest Ti II transition lines near the 580 nm feature. As expected, most of these lines are redder than Si II $\lambda5972$. These Ti II lines have a similar value of the excitation potential. For the rest of this chapter, we shall use Ti II $\lambda6012.750$ ($\lambda6013$) as the representative of these Ti II lines. This line is expected to be the strongest under an assumed value of a reasonable temperature.

Fig. 13 presents the optical depths of four interesting transition lines as a function of the temperature. We have used the C/O rich composition which is discussed in Hatano et al. (1999a). When the temperature is hotter than about 13,000 K, the

$\log(gf) - \theta\chi$	λ	$\log(gf)$	χ (eV)
-2.3123	6012.750	1.103	8.131687
-2.5893	5994.938	0.808	8.088701
-2.6386	6001.396	0.751	8.070395
-2.6648	6012.804	0.743	8.113845
-2.7105	5987.388	0.673	8.055932
-2.7306	6029.271	0.670	8.096740
-2.7443	6040.120	0.650	8.081670
-2.7447	5971.648	0.634	8.044443
-2.8498	6068.745	0.558	8.113845
-2.9333	5940.344	0.464	8.088701

Table 6.6: 10 strongest Ti II transitions near the 580 nm feature.

Fe III line is very strong. On the other hand, the Si II lines are weak, and the Ti II line is absent. This case represents the peculiar, powerful, and hot SNe 1991T and 1997br (see the previous chapter). But, as the temperature becomes cooler, the Fe III line becomes weaker. Instead, the Si II lines and the Ti II line become stronger. The Si II lines are the strongest when the temperature is about 8000 K, which represents normal SNe Ia (see the next chapter). Then, when the temperature is cooler than about 5000 K, the Ti II line becomes as strong as or stronger than the Si II lines, which represents the peculiar, weak, and cool SNe 1991bg and 1999by. Therefore, this figure well illustrates the spectroscopic sequence among SNe Ia as a function of the temperature.

Fig. 14 presents the "Si II" depth ratio from a different point of view. This figure compares two optical depth ratios as a function of the temperature : the one is the optical depth ratio between two Si II lines and the another is the optical depth ratio between the Ti II line and the red Si II line, in which both represent the 615 nm feature and the 580 nm feature. The optical depth is taken from the previous figure. The optical depth of the Ti II line is multiplied by 100 to account for many other Ti II lines near this one. When the temperature is hot, the contribution from the

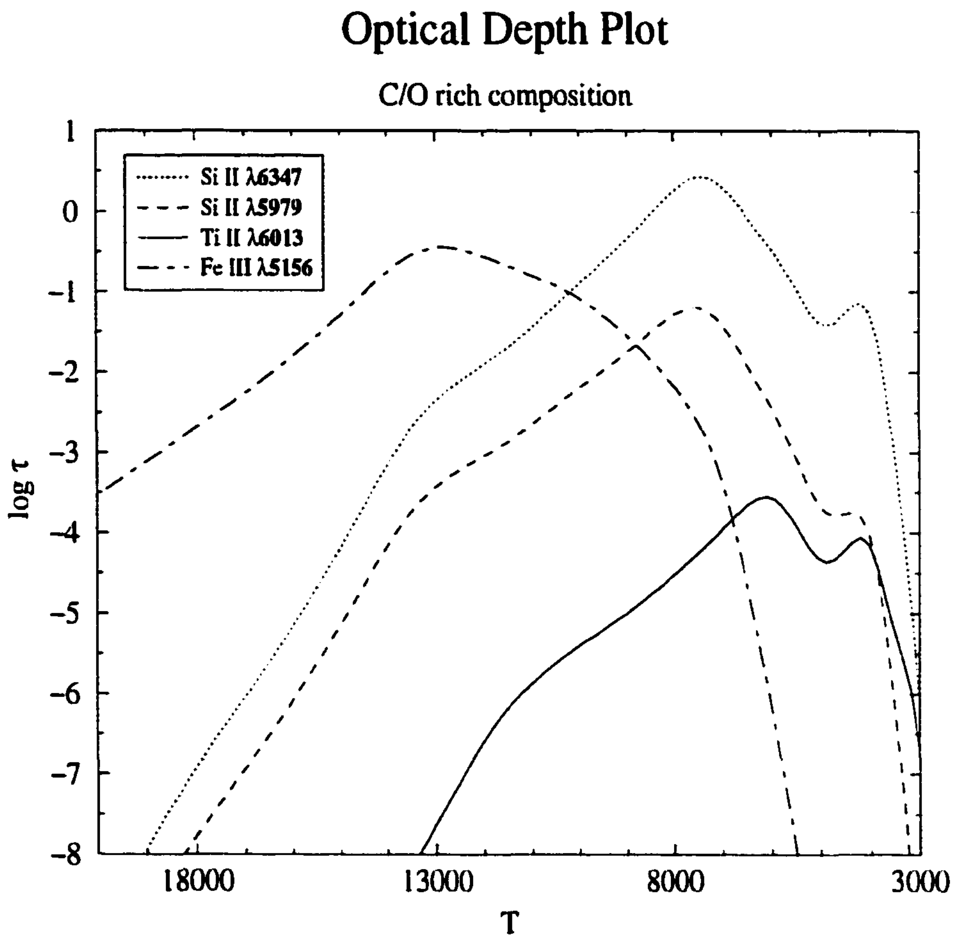
Optical Depth Plot
C/O rich composition
Si II λ6347
Si II λ5979
Ti II λ6013
Fe III λ5156
log τ
T
1
0
-1
-2
-3
-4
-5
-6
-7
-8
18000
13000
8000
3000

Figure 6.13:

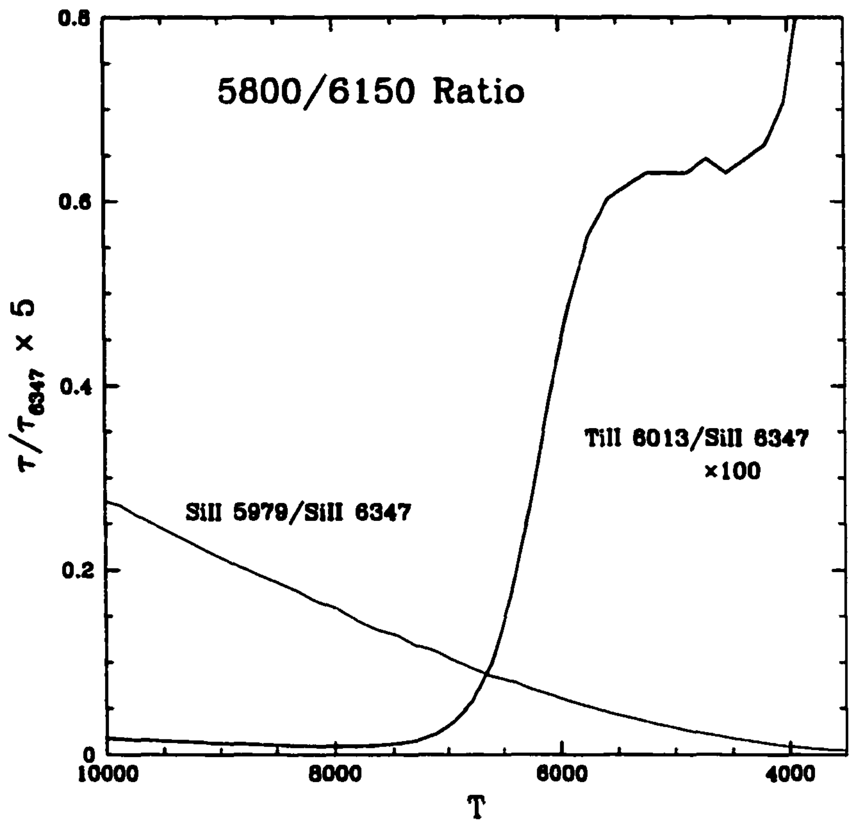

Figure 6.14: This figure is created by Peter Garnavich.

Ti II line is very weak. The depth ratio is the ratio between two Si II lines. Since the blue Si II line has a higher excitation potential, the depth ratio becomes larger for the hotter temperature. But, as the temperature becomes cooler, the optical depth of the Ti II line becomes large very quickly. Hence, the depth ratio becomes the ratio between the Ti II line and the red Si II line.

Chapter 7

Spectral Analysis of Other Type Ia SNe

7.1 Early Time Spectra

In this section, we shall present an analysis of early-time spectra of normal, or slightly peculiar SNe Ia. We shall begin this section by analyzing SN 1986G, a slightly peculiar and relatively weak event. Then, we shall proceed to stronger and brighter SNe along with a sequence of decreasing Δm_{15} . For each observed spectrum, a SYNOW analysis shall be given. v_{phot} represents the photospheric velocity. v_{max} is the maximum velocity for the calculation. And, T_{bb}, the blackbody temperature, determines the continuum of each SYNOW fit. And, the fitting parameters for each ion shall be given in tables. For all tables, λ, in the unit of Å, means the wavelength of the reference line of each ion used in the SYNOW calculation. λ is given only once in this entire chapter (i.e. λ is given the first time an ion appears in this chapter. After that, λ for that ion shall be omitted). τ represents the line optical depth of the reference line for each ion. The velocity interval within which an ion is used is between v_{min} and v_{max}, both in the unit of 10^3 km s^{-1}. When no v_{min} is given, the minimum velocity equals the photospheric velocity. v_e represents the e-folding velocity, in the unit of 10^3 km s^{-1}, that determines the exponential radial dependence of the line optical depths. T_{exc} is the excitation temperature, in the unit of 10^3 K, that determines the optical depths of other lines for each ion by using the Boltzmann excitation.

7.1.1 SN 1986G

ion	Ca II	Mg I	Si II	S II	Mg II	Ti II
λ	3934	5184	6347	5454	4481	3349
τ	50	0.7	3.5	2.2	1.5	20
v_{min}	...	...	...	...	11	...
v_{max}	18	17	20	12	17	16
v_e	3.0	3.0	3.0	3.0	3.0	3.0
T_{exc}	12	12	12	12	12	12

Table 7.1: Fitting Parameters for Figure 1

Fig. 1 presents an analysis of a spectrum of SN 1986G whose $\Delta m_{15} \sim 1.7$, that is 14 days after explosion. Some of the important fitting parameters are as follows: v_{phot} = 10,000 km s^{-1}, v_{max} = 40,000 km s^{-1}, and T_{bb} = 50,000 K. Fitting parameters for each ion are shown in Table 1. The blackbody temperature is rather large. This is probably because the observed spectrum has been over de-reddened. But, in any case, there is no significant physical meaning in this parameter. Thus, we shall use more appropriate excitation temperature (Normally, we set $T_{exc} = T_{bb}$).

First, it is obvious that the blue part of the spectrum is still heavily influenced by Ti II lines, although it's not as strongly as in the cases of SNe 1991bg and 1999by (previous chapter). And, Ti II lines near the 5800 Å feature still contribute to the strength of this "Si II" feature, making the relative ratio of the depths of two Si II features quite large (see previous chapter). Also, only a hint of Mg I line near 5000 Å (probably due to λ5184) may be seen as opposed to the cases of SNe 1991bg and 1999by in which this Mg I line is conspicuous. According to the LTE calculation by

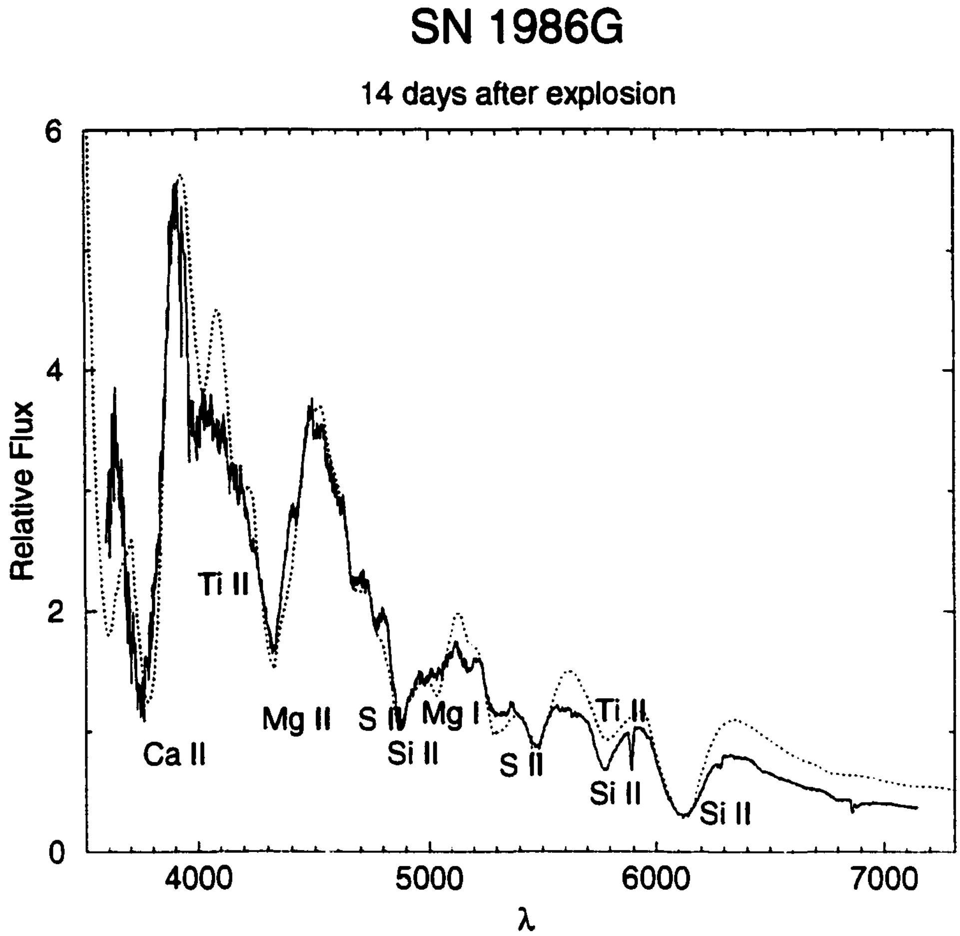

Figure 7.1: The observed spectrum is from Phillips et al. (1987).

Hatano et al. (1999a), Mg I lines may appear only if the temperature is cooler than 7,000 to 8,000 K. Other features in this spectrum may be attributed to usual singly ionized intermediate mass elements such as Mg II, Si II, S II, and Ca II.

7.1.2 SN 1992A

Fig. 2 presents an analysis of a spectrum of SN 1992A whose $\Delta m_{15} \sim 1.5$, that is 12 days after explosion. Some of the important fitting parameters are as follows: v_{phot} = 13,000 km s^{-1}, v_{max} = 40,000 km s^{-1}, and T_{bb} = 12,000 K. Fitting parameters for each ion are shown in Table 2.

ion	Ca II	O I	Si II	Ca II	S II	Fe III	Mg II	Si III
λ	—	7772	—	—	—	3013	—	4553
τ	7.0	1.0	5.0	7.0	1.5	0.3	1.2	0.2
v_{min}	...	...	...	20	...	...	...	...
v_{max}	16	40	18	40	15	40	40	18
v_e	3.0	3.0	3.0	3.0	3.0	3.0	3.0	3.0
T_{exc}	12	12	12	12	12	12	12	12

Table 7.2: Fitting Parameters for Figure 2

At a first glance, the spectrum looks normal. No convincing evidence of Ti II can be seen. The temperature of the line forming region is no longer cool enough to achieve high optical depth of Ti II. Most features can be attributed to usual ions found in the maximum-light spectra of SNe Ia. But, the velocity used to fit the absorption minimum of the Ca II H&K line is higher than v_{phot}, which suggests the existence of high velocity matter, or that the optical depth of this feature is very large. In the synthetic spectrum, the absorption minimum is fit by detached Ca II with v_{min} = 20,000 km s^{-1}. But, the shape of the H&K line also implies that low-velocity Ca II should exist. In the synthetic spectrum, v_{max} of the low-velocity Ca II is 16,000 km s^{-1}. Hatano et al. (1999b) discuss the existence of two component (high-velocity and low-velocity) Ca II in SN 1994D. Unlike SN 1994D, the H&K line appears to be unsplit in this spectrum. This is probably due to the high photospheric velocity of SN 1992A. In the synthetic spectrum, the optical depths of both low-velocity and high-velocity Ca II are not very large. Thus, the existence of two component Ca II in this spectrum is very suggestive.

In the synthetic spectrum, two doubly ionized ions (Si III and Fe III) are used. According to the LTE calculation by Hatano et al. (1999a), the co-existence of these ions with O I is possible. But, their contributions are very small. In the observed spectrum, only hints of Si III line near 4400 Å and Fe III line near 5000 Å can be seen. Thus, these ions are not labled in Fig. 2. The existence of Si HI and Fe III in this spectrum is probable.

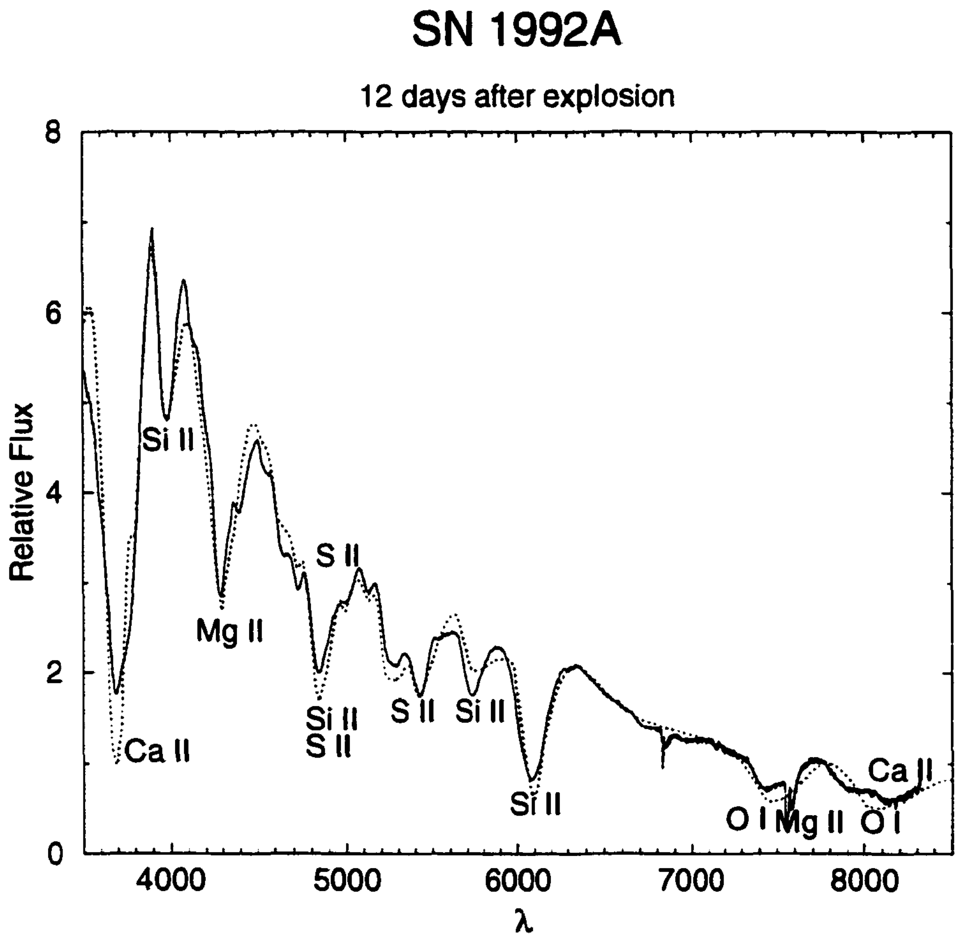

Figure 7.2: The observed spectrum is from Kirshner et al. (1993).

7.1.3 SN 1989B

ion	Ca II	O I	Si II	Ca II	S II	Fe III	Mg II	Si III	Co II	Cr II
λ	—	—	—	—	—	—	—	—	4161	2836
τ	5.0	0.5	3.5	4.0	1.0	0.5	0.8	1.0	0.1	
v_{min}	...	...	...	18	...	...	13	...	...	...
v_{max}	16	40	20	40	14	40	17	13	40	40
v_e	3.0	3.0	3.0	3.0	3.0	3.0	3.0	3.0	3.0	3.0
T_{exc}	12	12	12	12	12	12	12	12	12	12

Table 7.3: Fitting Parameters for Figure 3

Fig. 3 presents an analysis of a spectrum of SN 1989B whose $\Delta m_{15} \sim 1.3$, that is 11 days after explosion. Some of the important fitting parameters are as follows: v_{phot} = 11,000 km s^{-1}. v_{max} = 40,000 km s^{-1}, and T_{bb} = 12,000 K. Fitting parameters for each ion are shown in Table 3.

First, the Si III line near 4400 Å is conspicuous in this spectrum. The Fe III absorption near 5000 Å is also deeper than that feature in the SN 1992A spectrum. On the other hand, the O I and Mg II features near 7500 Å are much weaker compared to SN 1992A. These suggest that the temperature of the line forming region in SN 1989B is hotter than the temperature in SN 1992A, as expected from the values of Δm_{15} . But, like SN 1992A, two component Ca II is still necessary to fit the observed Ca II H&K absorption. The fitting parameters for Ca II are very similar to the parameters used to fit the H&K line in the SN 1992A spectrum.

In addition to usual ions found in the spectra of normal SNe Ia, Fig. 3 provides new line identifications in the spectrum of SN 1989B. A conspicuous absorption line near 3300 Å can be fit by Cr II. And, a weak feature near 3500 Å can be attributed to Co II. In general, it is hard to identify a line in the ultraviolet spectra because of severe line blending by various iron peak elements. Kirshner et al. (1993) implied the existence of Cr II in the ultraviolet spectra of SN 1992A. And, Fisher et al. (1997) used Cr II to fit the 14 days before maximum light spectrum of SN 1990N. But, neither

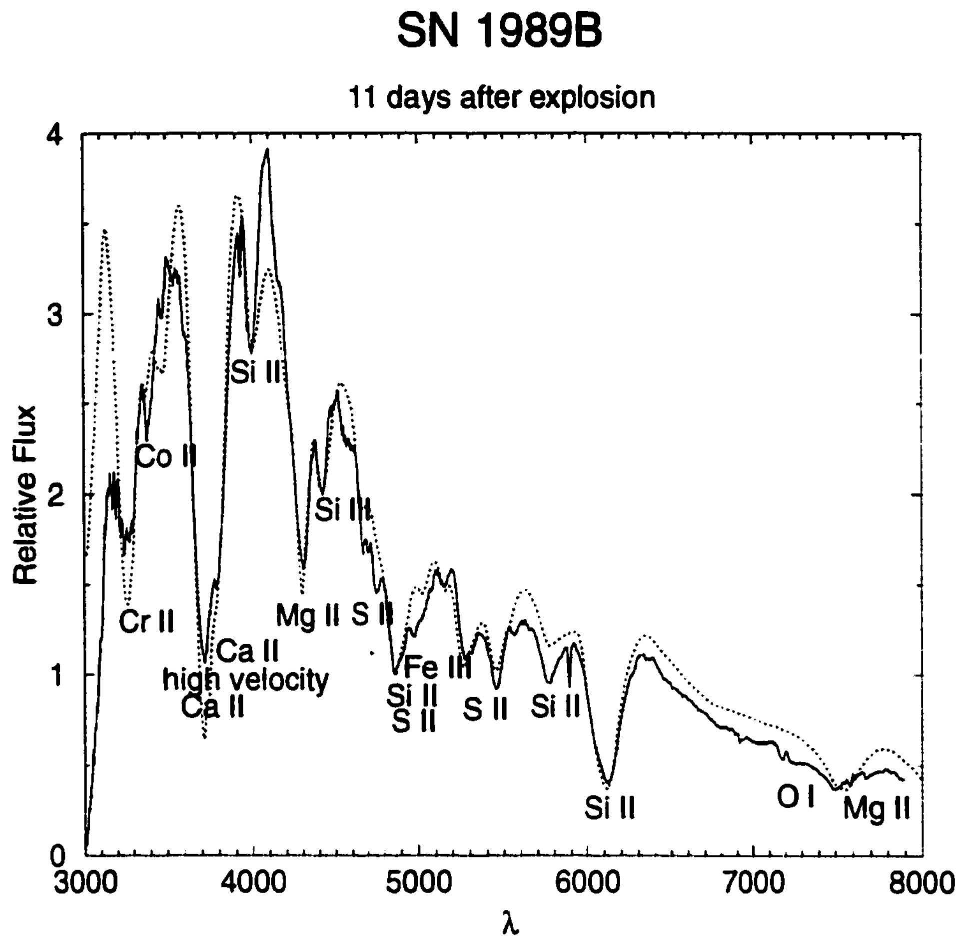

Figure 7.3: The observed spectrum is from Wells et al. (1994).

has clearly identified a Cr II line. Fig. 3 indicates that Cr co-exists with usual SN Ia elements, such as Si and S above 11,000 km s^{-1}. This new line identification could be used to constrain hydrodynamical models.

7.1.4 SN 1994D

Fig. 4 presents an analysis of a spectrum of SN 1994D whose $\Delta m_{15} \sim 1.3$, that is 4 days before maximum light. Some of the important fitting parameters are as follows: v_{phot} = 10,000 km s^{-1}, v_{max} = 40,000 km s^{-1}, and T_{bb} = 12,000 K. Fitting parameters for each ion are shown in Table 4.

ion	O I	Ca II	Ca II	Fe III	Si II	Cr II	S II	Mg II	Si III
τ	0.5	2	6	0.2	2.5	5	2.5	0.5	0.6
v_{min}	...	18	...	...	...	...	...	13	...
v_{max}	40	40	16	40	40	40	12	17	15
v_e	3.0	3.0	3.0	3.0	3.0	3.0	3.0	3.0	3.0
T_{exc}	12	12	12	12	12	12	12	12	12

Table 7.4: Fitting Parameters for Figure 4

Unlike SNe 1992A and 1989B, the Ca II H&K line is obviously split. In the synthetic spectrum, this feature can be fit by two component Ca II. The velocity intervals for Ca II are very similar to the intervals used in SNe 1992A and 1989B. But, now the optical depth of low-velocity Ca II is three times larger than that of high-velocity Ca II. And, v_{phot} equals only to 10,000 km s^{-1}. As a result, the H&K line is clearly split.

In spite of the smaller optical depth, the high-velocity Ca II H&K line is stronger than the low-velocity H&K line. This is due to a geometrical effect (detached lines become deeper). And, this is also probably because Si II and/or Si III line contribute to the depth of the high-velocity H&K line. But, the presence of the high-velocity Ca II is definite. The synthetic feature attributed to Si II and/or Si III line near the Ca II H&K line is too weak to account for the observed absorption (see Hatano et al. 1999b). More importantly, the high-velocity Ca II can nicely account for the weak feature near 8000 Å. This feature is much stronger in the earlier epoch when the high-velocity H&K line is much stronger (Hatano et al. 1999b). Therefore, the high-velocity H&K line is mostly attributed to the high-velocity Ca II.

The value of Δm_{15} is very similar to that of SN 1989B. As expected, therefore, the strengths of Si III line near 4400 Å, of Fe III line near 5000 Å, and of O I/Mg II line near 7500 Å are very similar to those of SN 1989B. Like SN 1989B, the Cr II line near 3300 Å is conspicuous, which indicates that Cr co-exists with usual SN Ia elements, such as Si and S, above 10,000 km s^{-1}.

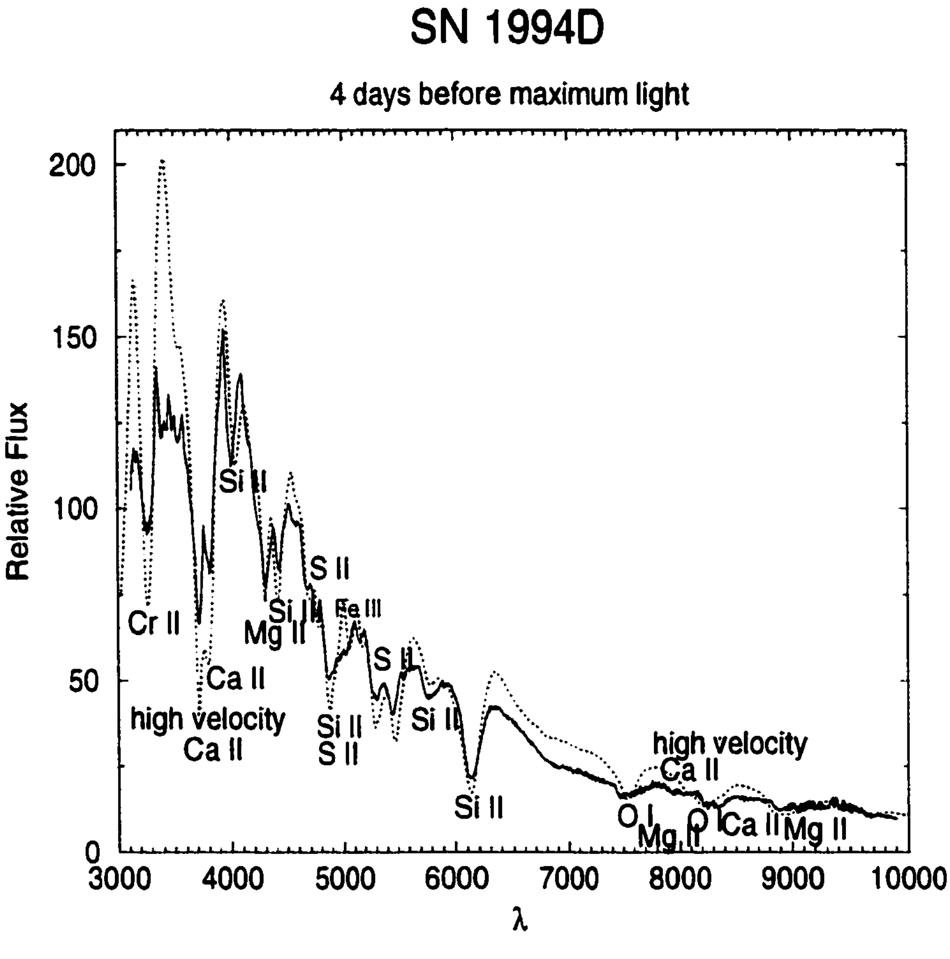

Figure 7.4: The observed spectrum is provided by Alex Filippenko.

7.1.5 SN 1998aq

ion	Ca II	Si III	Si II	Ca II	S II	Fe III	C II
λ	—	—	—	—	—	—	4267
τ	1.8	0.6	0.8	0.5	1.0	0.5	0.05
v_{min}	...	...	...	20	...	...	...
v_{max}	16	16	16	23	14	15	40
v_e	3.0	3.0	3.0	3.0	3.0	3.0	3.0
T_{exc}	14	14	14	14	14	14	14

Table 7.5: Fitting Parameters for Figure 5

Fig. 5 presents an analysis of a spectrum of SN 1998aq whose $\Delta m_{15} \sim 1.2$, that is 12 days before maximum light. Some of the important fitting parameters are as follows: v_{phot} = 12,000 km s^{-1}, v_{max} = 40,000 km s^{-1}, and T_{bb} = 14,000 K. Fitting parameters for each ion are shown in Table 5.

This spectrum looks somewhat peculiar. Si III line near 4400 Å is unusually strong, while there is no convincing evidence of Mg II in the spectrum. A hint of another Si III line near 5500 Å can also be seen (a small absorption between S II "W" feature and Si II feature). Fe III lines also significantly contribute to the features in the spectrum. In spite of its very early epoch (-12 days), observed features are not very broad compared to the features in the spectra of SN 1990N (-14 days, Leibundgut et al. 1991) and SN 1994D (-12 days, Hatano et al. 1999b). The photospheric velocity is also only 12,000 km s^{-1}. Because of this low velocity, S II lines near 4700 Å are well resolved. These suggest that this is a relatively hot, but relatively slow supernova.

The most interesting features in the spectrum are C II lines. The synthetic spectrum fits with these C II lines very well without detaching it. This gives the minimum velocity of carbon to be about 12,000 km s^{-1}. This is, for example, slower than the minimum velocity predicted by the model W7 (Branch et al. 1985).

Fig. 6 presents an analysis of a spectrum of SN 1998aq whose $\Delta m_{15} \sim 1.2$, that is 2 days after maximum light. Some of the important fitting parameters are as follows:

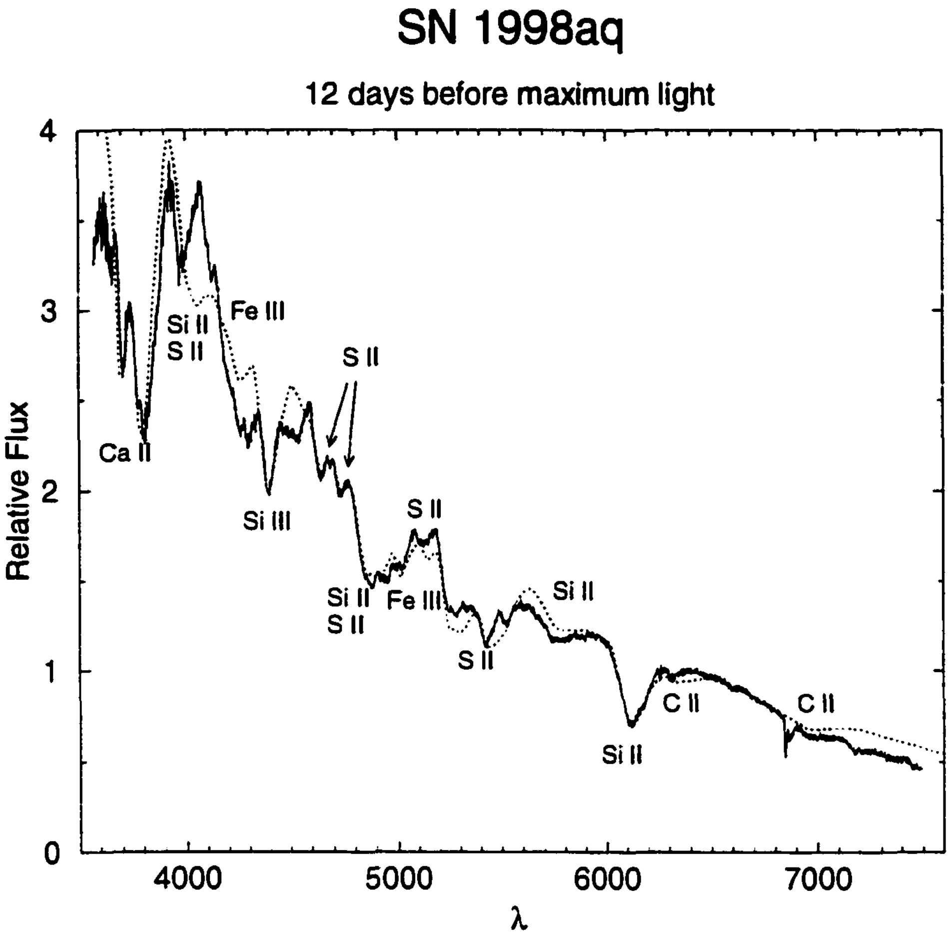

Figure 7.5: The observed spectrum is provided by Peter Garnavich.

ion	Ca II	Si III	Si II	Ca II	S II	Mg II
τ	20	1.0	2.5	1.5	1.7	1.0
v_{min}	...	...	...	18	...	12
v_{max}	14	15	15	21	14	17
v_e	3.0	3.0	3.0	3.0	3.0	3.0
T_{exc}	14	14	14	14	14	14

Table 7.6: Fitting Parameters for Figure 6

v_{phot} = 10,000 km s^{-1}, v_{max} = 40,000 km s^{-1}, and T_{bb} = 14,000 K. Fitting parameters for each ion are shown in Table 6.

By this epoch, C II lines have disappeared. Si III line near 4400 Å is no longer conspicuous. Another Si III line near 5500 Å also has disappeared. Instead, Mg II line near 4300 Å has appeared. And, in general, S II features and Si II features have become stronger compared to the -12 days spectrum. An absorption near 5000 Å is probably due to Fe II rather than to Fe III because there is no evidence of Fe III line near 4200 Å. Therefore, the temperature has become cooler by this epoch.

This spectrum looks, at a first glance, normal. But, it is still somewhat peculiar. First, the features in this spectrum have become broader compared to the features in the -12 days spectrum. Usually, spectral features become narrower as the photospheric velocity decreases. And, there are two absorptions in the spectral region of 4000 ~ 4200 Å. Normally, there is only one absorption in this region (due to Si II and S II). The left feature in this spectrum is probably due to Si II and S II, although the fit is not perfect. The right one is unidentified.

7.1.6 SN 1999aa

ion	Si III	Ca II	Ca II	Si II	He II	Ni III	Fe III
λ	—	—	—	—	4686	2734	—
τ	0.5	2	2	0.5	0.5	5.0	1.5
v_{min}	...	21	...	...	...	...	...
v_{max}	40	40	21	40	40	20	20
v_e	3.0	3.0	3.0	3.0	3.0	3.0	3.0
T_{exc}	13	13	13	13	13	13	13

Table 7.7: Fitting Parameters for Figure 7

Fig. 7 presents an analysis of a spectrum of SN 1999aa whose $\Delta m_{15} \sim 1.2$, that is 10 days before maximum light. This Δm_{15} value has been estimated from using a tight relationship between Δm_{15} and the ratio of the depths of two Si II features

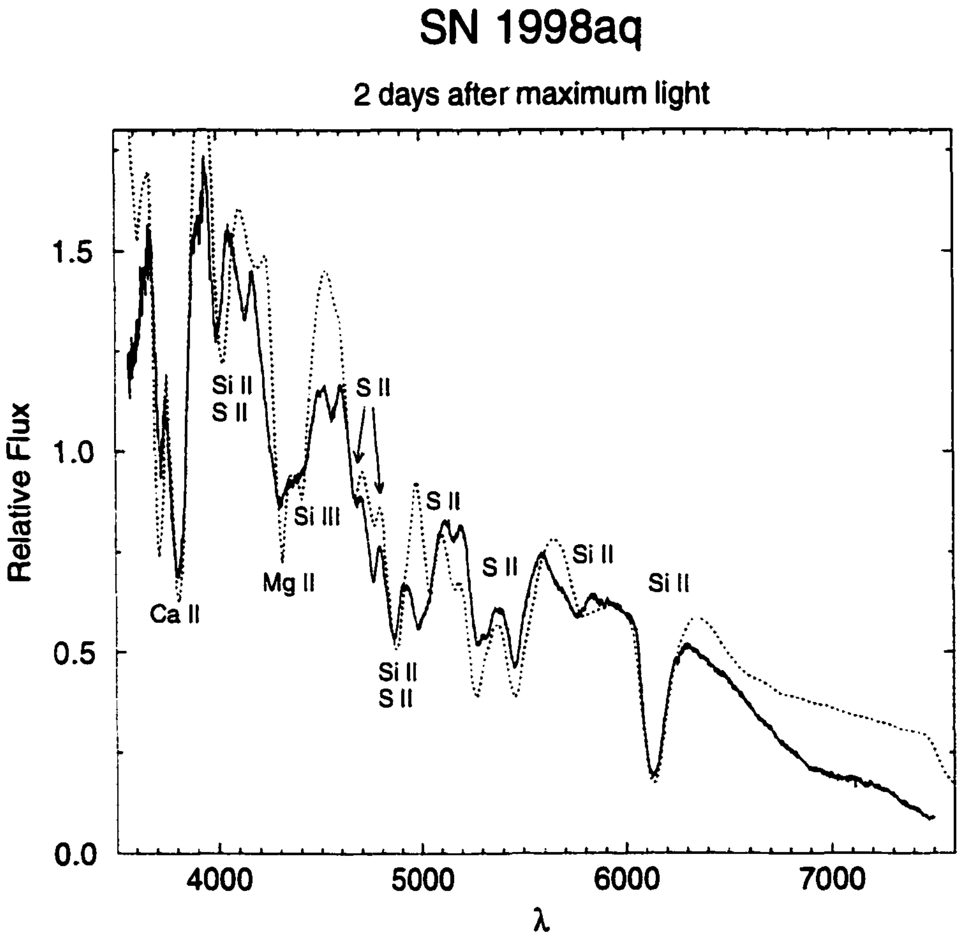

Figure 7.6: The observed spectrum is provided by Peter Garnavich.

near 6150 Å and 5800 Å (Garnavich et al. 2000). The depth ratio was obtained from Fig. 8. But, the actual value of Δm_{15} is 0.92 (W. Li, personal communication). Some of the important fitting parameters are as follows: v_{phot} = 12,000 km s^{-1}, v_{max} = 40,000 km s^{-1}, and T_{bb} = 13,000 K. Fitting parameters for each ion are shown in Table 7.

At a first glance, this spectrum looks like the spectra of peculiar, powerful type Ia supernovae, SN 1991T (Fisher et al. 1999) and SN 1997br (Hatano et al. 2000a). Two Fe III lines (near 4200 Å and near 5000 Å) are very conspicuous. And, Ni III lines are contributing to some of the observed features. An absorption near 6100 Å can be attributed to Si II λ6355. Two weak absorptions (near 4400 ~ 4500 Å) are probably due to Si III (left) and He II (right).

But, unlike other SN 1991T like events, the Ca II H&K line is very strong in this spectrum. The H&K line can be fit by high-velocity Ca II that is detached at 21,000 km s^{-1}. This high velocity Ca II can also account for a weak feature near 8000 Å. The presence of strong Ca II lines in this epoch implies somewhat cooler temperature in this supernova compared to other SN 1991T like events in a similar epoch. Also, in spite of its very early epoch, Si II line near 6100 Å is already present. In the case of SN 1997br, this Si II line appeared only in the later epoch (Hatano et al. 2000a). This means that this supernova is somewhat weaker than other SN 1991T like events, and that has produced more intermediate mass elements.

ion	Si III	Ca II	Ca II	Si II	Mg II	S II	O I	Fe III
τ	0.5	2	5	1.5	0.5	0.7	0.2	1.5
v_{min}	...	16	...	...	13	...	...	...
v_{max}	40	40	14	15	40	13	40	20
v_e	3.0	3.0	3.0	3.0	3.0	3.0	3.0	3.0
T_{exc}	13	13	13	13	13	13	13	13

Table 7.8: Fitting Parameters for Figure 8

Fig. 8 presents an analysis of a spectrum of SN 1999aa whose Δm_{15} ~ 0.92, that is near maximum light. Some of the important fitting parameters are as follows: v_{phot}

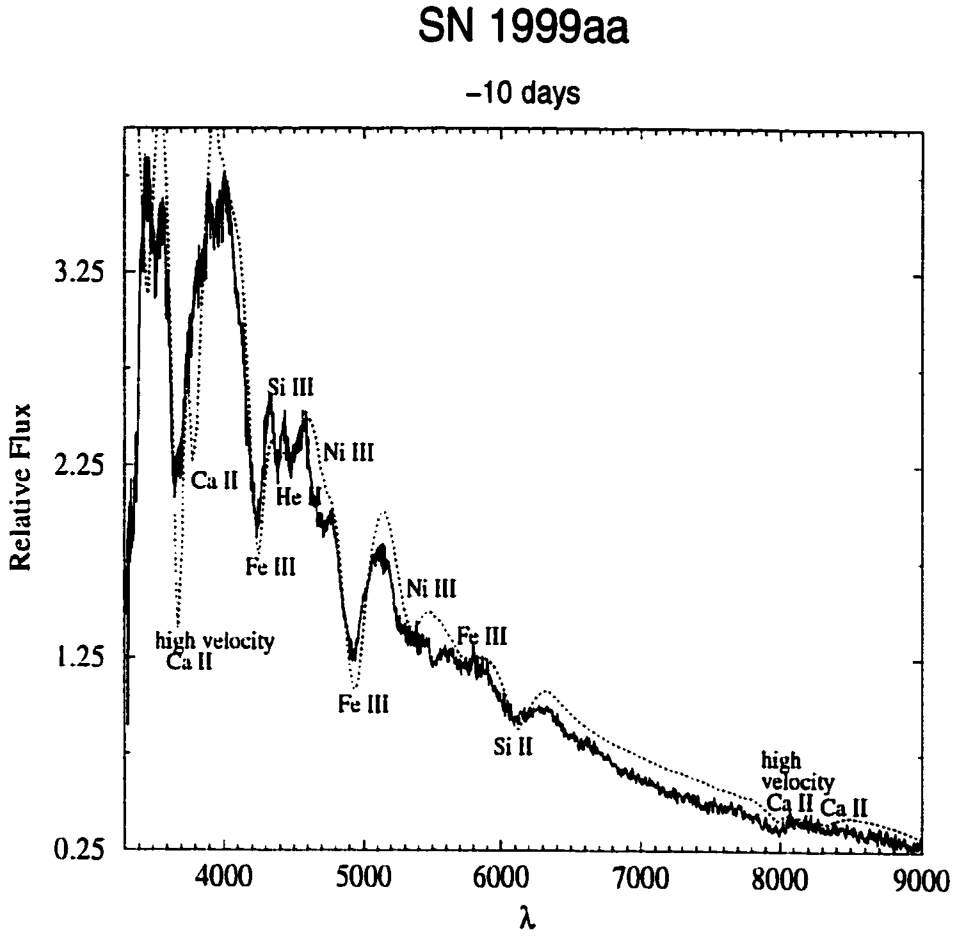

Figure 7.7: The observed spectrum is provided by Alex Filippenko.

= 9,000 km s^{-1}, v_{max} = 40,000 km s^{-1}, and T_{bb} = 13,000 K. Fitting parameters for each ion are shown in Table 8.

By this epoch, the spectrum has become very normal. Most of the observed features can be attributed to usual SN Ia ions such as Si II, S II, Mg II, O I, Si III, and Ca II. But, Fe III lines are still somewhat stronger than usual. And, Si II line near 6100 Å is not as strong as usual. These suggest that this supernova is hotter than normal SNe Ia, and has produced less intermediate mass elements compared to normal SNe Ia. But, Fig. 7 indicates that this supernova is cooler than SN 1991T like events, and has produced more intermediate mass elements compared to SN 1991T like events. Therefore, this supernova is an intermediate event, that is between normal SNe Ia and SN 1991T like SNe Ia.

According to the definitions used by Branch et al. (1993) who have distinguished normal SNe Ia from peculiar SNe Ia like SN 1991T or SN 1991bg based on the sample of SNe Ia that are near maximum light, this supernova would be classified into a normal event. But, Fig. 7 clearly shows that this is a peculiar event. Therefore, it is now necessary to re-define what are normal, and what are peculiar.

By this epoch, the Ca II H&K line has become obviously split. And, there are two Ca II lines around 8000 ~ 8300 Å, that can be attributed to low-velocity and high-velocity Ca II. At the epoch of -10 days, only high-velocity Ca II is seen because the temperature of outer layers is cool enough to achieve high optical depth of Ca II. But, by this epoch, the temperature of inner layers has also become cool enough to produce strong Ca II lines. Therefore, a detailed analysis of these line splits could be very useful to understand the temperature structure of SNe Ia.

7.1.7 SN 1990N

Fig. 9 presents an analysis of a spectrum of SN 1990N whose $\Delta m_{15} \sim 1.1$, that is 10 days after explosion. Some of the important fitting parameters are as follows: v_{phot} = 11,500 km s^{-1}, v_{max} = 40,000 km s^{-1}, and T_{bb} = 10,000 K. Fitting parameters for

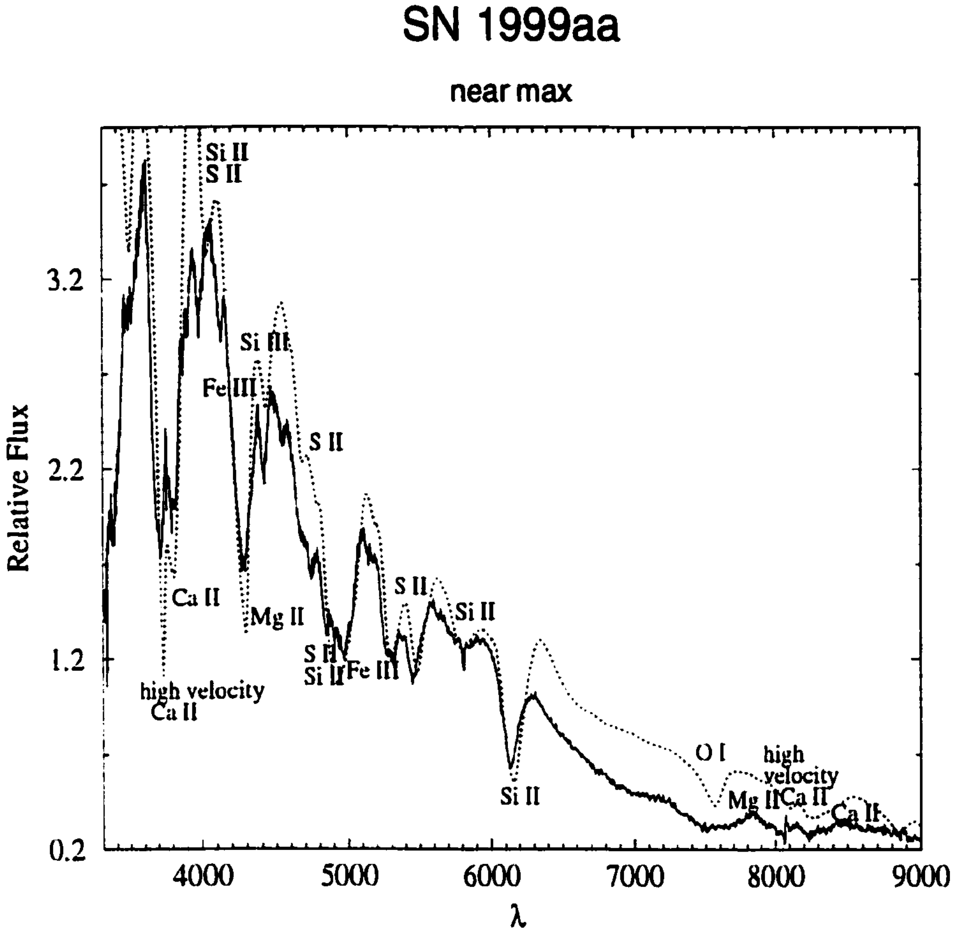

Figure 7.8: The observed spectrum is provided by Alex Filippenko.

ion	Co II	Si II	Si III	S II	Ca II	Ca II	Cr II	Fe III
τ	0.05	1.5	0.5	1.0	1.0	3.0	15	0.7
v_{min}	...	...	...	...	...	20	...	...
v_{max}	40	40	40	14	20	40	40	40
v_e	3.0	3.0	3.0	3.0	3.0	3.0	3.0	3.0
T_{exc}	10	10	10	10	10	10	10	10

Table 7.9: Fitting Parameters for Figure 9

each ion are shown in Table 9.

First, the spectrum indicates that the temperature of this supernova is relatively hot among normal SNe Ia. Si III line near 4400 Å is very conspicuous. And, another Si III line near 5500 Å is clearly seen. Two Fe III features (near 4200 Å and near 5000 Å) are also very strong. On the other hand, Si II line near 6100 Å is not as strong as usual. And, there is no clear evidence of Mg II in the spectrum. These are expected from its small value of Δm_{15} .

Like SNe 1989B and 1994D, a very strong feature near 3300 Å can be attributed to Cr II. Cr II can also account for the most of the low flux around 2500 ~ 3000 Å. Co II contributes to this low flux near 2500 Å. And, there is a weak Co II feature near 3500 Å. It is interesting to see that only two iron-peak ions (Cr II and Co II) can fit the observed ultraviolet spectrum very well. This shows that Cr and Co co-exists with usual SN Ia elements above 11,500 km s^{-1}.

7.1.8 SN 1998bu

ion	Ca II	Ca II	C II	Si II	S II	Fe III	Si III	Mg II	O I
τ	10	2	0.03	2.5	1.0	1.0	1.0	0.3	0.2
v_{min}	...	20	...	...	...	...	...	...	...
v_{max}	16	23	40	18	15	40	16	17	40
v_e	3.0	3.0	3.0	3.0	3.0	3.0	3.0	3.0	3.0
T_{exc}	12	12	12	12	12	12	12	12	12

Table 7.10: Fitting Parameters for Figure 10

Fig. 10 presents an analysis of a spectrum of SN 1998bu whose $\Delta m_{15} \sim 1.0$, that is 12 days after explosion. This Δm_{15} value is very small. There are very few supernovae whose Δm_{15} value is smaller than 1.0. The peculiar, powerful SN 1991T is one of them. Some of the important fitting parameters are as follows: v_{phot} = 12,000 km s^{-1}, v_{max} = 40,000 km s^{-1}, and T_{bb} = 12,000 K. Fitting parameters for each ion are shown in Table 10.

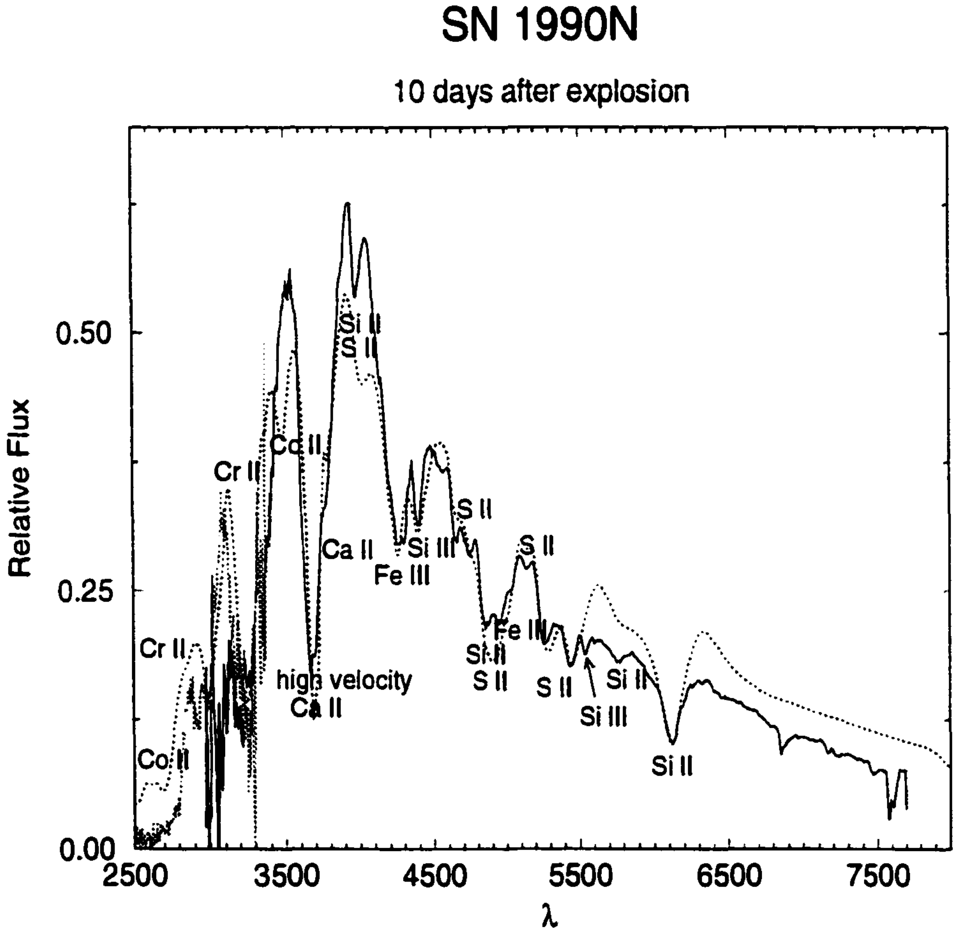

Figure 7.9: The observed spectra (optical and ultraviolet) are from Leibundgut et al. (1991).

As expected, this spectrum is very similar to the previous figure for SN 1990N. But, Si III line near 4400 Å is even stronger. And, another Si III line near 5500 Å is clearly seen. Fe III lines also strongly contribute to the spectral features. Although Mg II is used in the synthetic spectrum, its existence is not very clear because Mg II lines are blended with other lines. Instead, C II lines fit the observed features fairly well. Therefore, this supernova is also a relatively hot event among normal SNe Ia.

This spectrum is a very good example to show that the split of the Ca II H&K line is caused by the presence of high-velocity and low-velocity Ca. The high-velocity component of the H&K feature is fit by Ca II that is detached at 20,000 km s^{-1}. A feature attributed to Si II and/or Si III is too weak to account for the high-velocity component. Then, this high-velocity Ca II can nicely account for a weak absorption feature near 8000 Å.

ion	Ca II	Ca II	Si II	S II	Fe III	Si III	Mg II	O I
τ	8	2	2.5	1.0	1.0	1.0	1.0	0.6
v_{min}	...	20	...	...	...	...	...	...
v_{max}	16	23	16	15	40	13	17	40
v_e	3.0	3.0	3.0	3.0	3.0	3.0	3.0	3.0
T_{exc}	14	14	14	14	14	14	14	14

Table 7.11: Fitting Parameters for Figure 11

Fig. 11 presents an analysis of a spectrum of SN 1998bu whose $\Delta m_{15} \sim 1.0$, that is 18 days after explosion. Some of the important fitting parameters are as follows: v_{phot} = 11,000 km s^{-1}, v_{max} = 40,000 km s^{-1}, and T_{bb} = 14,000 K. Fitting parameters for each ion are shown in Table 11.

Now, the spectrum looks very normal. Mg II line near 4300 Å is very strong, stronger than Si III line near 4400 Å. And, there is no convincing evidence of another Si III feature near 5500 Å. These indicate that the temperature of the line forming region has cooled down. But, the blackbody temperature, T_{bb}, in this figure is somewhat hotter than T_{bb} in the previous figure. This is probably because while T_{bb} is used to fit the continuum in the synthetic spectrum, the continuum in the actual SNe is

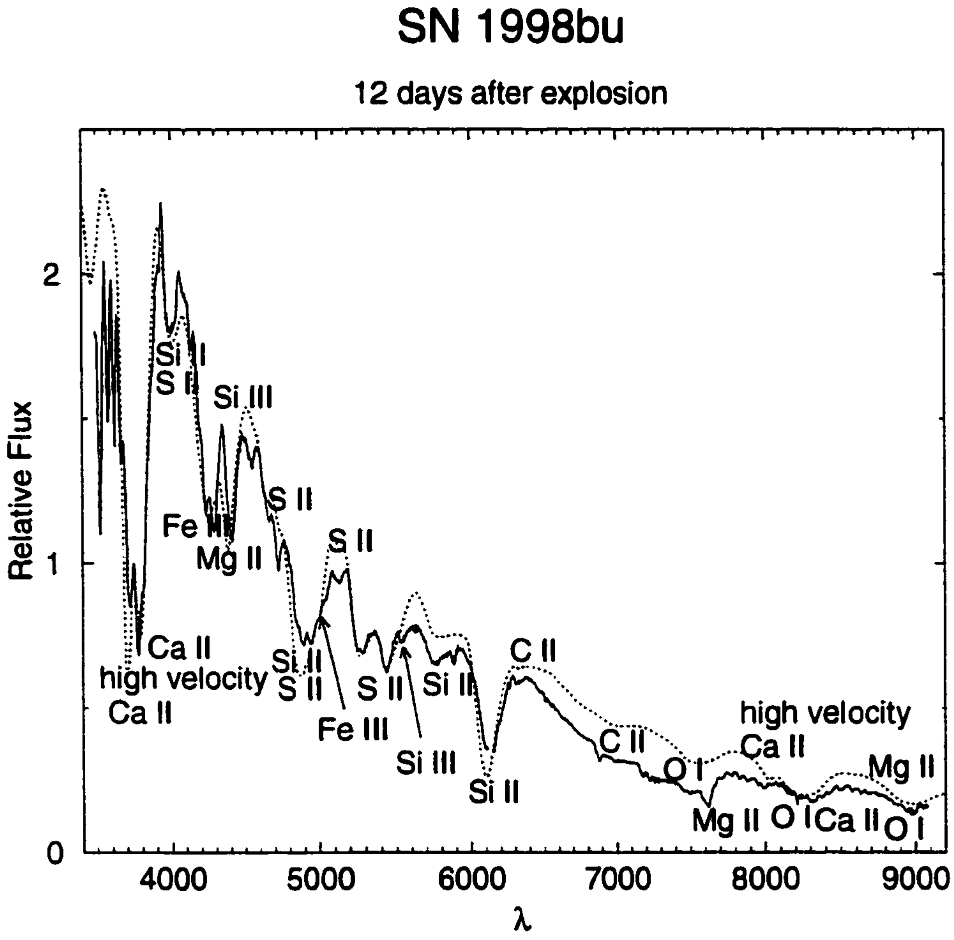

Figure 7.10: The observed spectrum is from Hernandez et al. (2000).

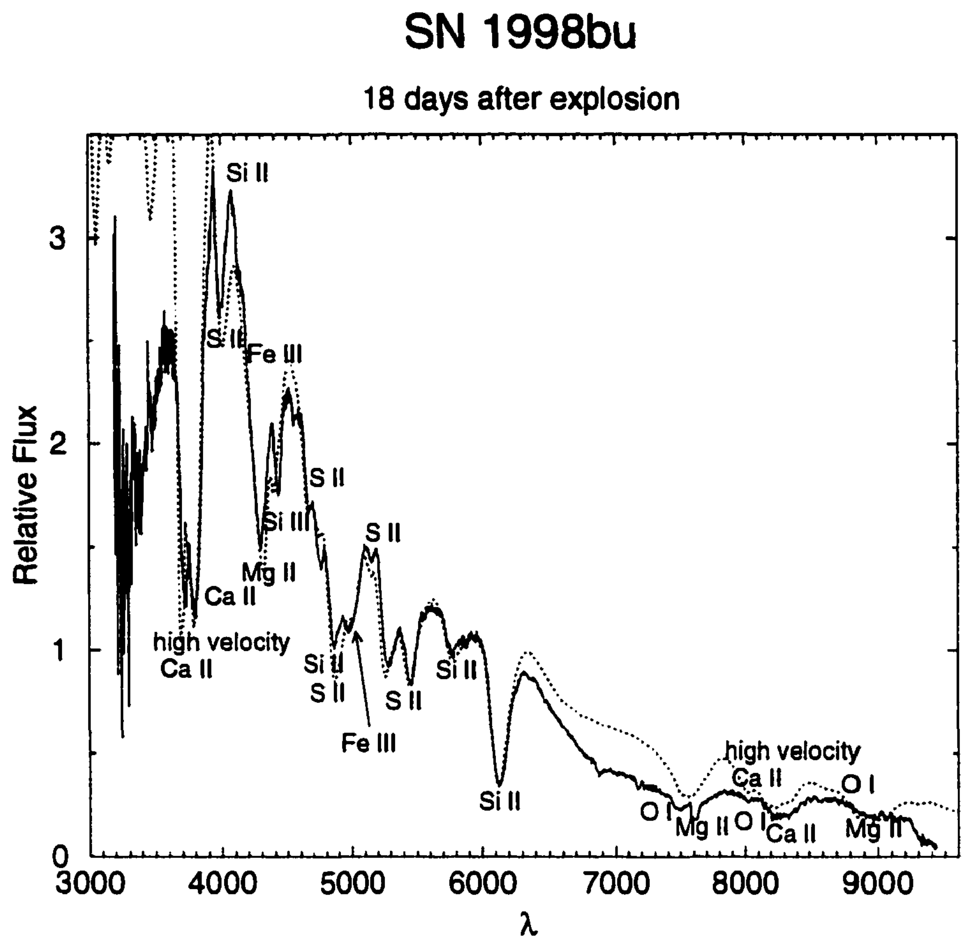

Figure 7.11: The observed spectrum is from Hernandez et al. (2000).

different.

Other than two usual problems seen in SYNOW calculations (continuum of wavelength region longer than 6500 Å and large flux difference near ultraviolet region), the fit is very good. Synthetic Si II and S II features fit the observed features very well. The Ca II H&K line is still split. Consequently, there is an evidence of high–velocity Ca II near 8000 Å.

7.1.9 Discussion

Here, we shall compare the early–time spectra of normal SNe Ia, SNe 1992A (Fig. 2), 1989B (Fig. 3), 1994D (Fig. 4), 1990N (Fig. 9), and 1998bu (Fig. 10). These spectra are ranging from four days before the maximum light to eight days before the maximum light, assuming that the rise time to the maximum light is 18 days. Here, we shall prove that Δm_{15} is closely related to the temperature of SNe by comparing these five spectra focusing on two spectral regions, 4300 $\sim$ 4400 Å and 4800 $\sim$ 5000 Å.

There are three major spectral lines around the first spectral region, 4300 $\sim$ 4400 Å, - due to Mg II, Si III, and Fe III. In the spectrum of SN 1992A whose value of Δm_{15} is the largest among these five SNe, a feature attributed to Mg II is very strong near 4300 Å. On the other hand, there is only a hint of a feature near 4400 Å, which can be attributed to Si III. And, there is no evidence of Fe III in this spectral region. Therefore, the temperature of this SN is relatively cool. In the case of SN 1989B whose value of Δm_{15} is smaller, the Si III line is stronger. But, the Mg II line is still stronger than the Si III line. In the case of SN 1994D whose value of Δm_{15} is even smaller, the Si III line is as strong as the Mg II line. In the case of SN 1990N whose value of Δm_{15} is even smaller, the "Mg II" feature near 4300 Å is now blended with the Fe III line. And, the Si III line is still as strong as this Mg II + Fe III feature. In the case of SN 1998bu whose value of Δm_{15} is the smallest, the Si III line is stronger than the Mg II + Fe III feature. Therefore, smaller value of Δm_{15} implies hotter temperature.

A similar spectral evolution can be observed around the second spectral region, 4800 $\sim$ 5000 Å. In the case of SN 1992A, there is only one strong absorption feature near 4800 Å, which is due to a blend of Si II and S II lines. On the other hand, there is only a hint of a feature near 5000 Å, which could be attributed to Fe III. In the case of SN 1989B, a feature attributed to Fe III is clearly seen near 5000 Å. But, the Si II + S II feature is still stronger than this Fe III feature. In the case of SN 1994D, the relative strength of these two features is about the same as the case of SN 1989B.

And, in the cases of SNe 1990N and 1998bu, this Fe III line is about as strong as the Si II + S II feature. Therefore, once again, smaller value of Δm_{15} implies hotter temperature.

In the spectra of SNe 1989B, 1994D, and 1990N, we have identified a Cr II line in the near ultraviolet. According to the LTE calculation by Hatano et al. (1999a), Cr II is one of the strongest ions around 7,000 K for the oxygen-burned composition. We have found that Cr co-exists with usual SN Ia elements, such as Si and S, generally above about 10,000 km s^{-1}. This is generally consistent with the model W7, the best SN Ia explosion model to date (Nomoto et al. 1984, Branch et al. 1985). In the model W7, the maximum velocity of Cr is about 12,500 km s^{-1}, and it extends all the way to the center. This constraint is also consistent with the models CS15DD1 - DD3 by Iwamoto et al. (1999). But, the minimum velocity of Cr is different among DD1, DD2, and DD3. The minimum velocities are about 5,000 km s^{-1}(DD1), about 8,000 km s^{-1}(DD2), and about 10,000 km s^{-1}(DD3). Thus, if later-time near ultraviolet spectra are available, it may be possible to determine the minimum velocity of Cr. Then, it can be used to constrain the hydrodynamical models. On the other hand, this constraint is not consistent with models by Livne and Arnett (1995). In their models, the maximum velocity of Si is about same as the minimum velocity of Cr. Thus, Cr does not co-exist with Si. Their models produce a large amount of high-velocity Cr.

In the spectra of SNe 1998aq and 1998bu, we have found that the minimum velocity of C II is about 12,000 km s^{-1}. Especially, the fit of SN 1998aq (Fig. 5) is very good. In the model W7, the minimum velocity of C is about 14,000 km s^{-1}. Thus, it is not too far from what we've found. On the other hand, the minimum velocities of C in the models CS15DD1 - DD3 are about 18,000 km s^{-1}(DD1), about 20,000 km s^{-1}(DD2), and about 24,000 km s^{-1}(DD3). Thus, these models probably do not represent SNe 1998aq and 1998bu.

7.2 High–Velocity Supernovae

In this section, we shall present an analysis of the spectra of "high–velocity" type Ia supernovae. The existence of high–velocity SNe Ia was first pointed out by Branch (1987a). Branch showed that the spectral features of SN 1984A are like features of other SNe Ia, but the blueshift of these features is much larger than the blueshift normally seen in the spectra of other SNe Ia. This means that the velocity of each element in SN 1984A is much larger than the velocity normally seen in the spectra of other SNe Ia. We shall begin this section by analyzing the spectrum of SN 1984A, then introduce other high–velocity SNe Ia. Then, we shall summarize the characteristics of these high–velocity spectra.

7.2.1 SN 1984A

ion	Mg II	Ca II	Si III	Si II	S II	Fe III	Fe II
λ	—	—	—	—	—	—	5018
τ	1.5	1000	1.0	7.0	2.0	2.0	1.5
v_{min}	...	...	...	...	...	...	25
v_{max}	40	40	20	40	40	40	30
v_e	3.0	3.0	3.0	3.0	3.0	3.0	3.0
T_{exc}	14	14	14	14	14	14	10

Table 7.12: Fitting Parameters for Figure 12

Fig. 12 presents an analysis of a spectrum of SN 1984A, that is 11 days after explosion. Some of the important fitting parameters are as follows: v_{phot} = 17,000 km s^{-1}, v_{max} = 40,000 km s^{-1}, and T_{bb} = 14,000 K. Fitting parameters for each ion are shown in Table 12.

This is the classical example of high–velocity spectrum. It is obvious that all spectral features are very broad and deep. The Ca II H&K line is very strong. In the synthetic spectrum, the optical depth of Ca II is 1000, which is much larger than usual. The Si II line near 6000 Å, which is normally near 6150 Å in other SNe Ia,

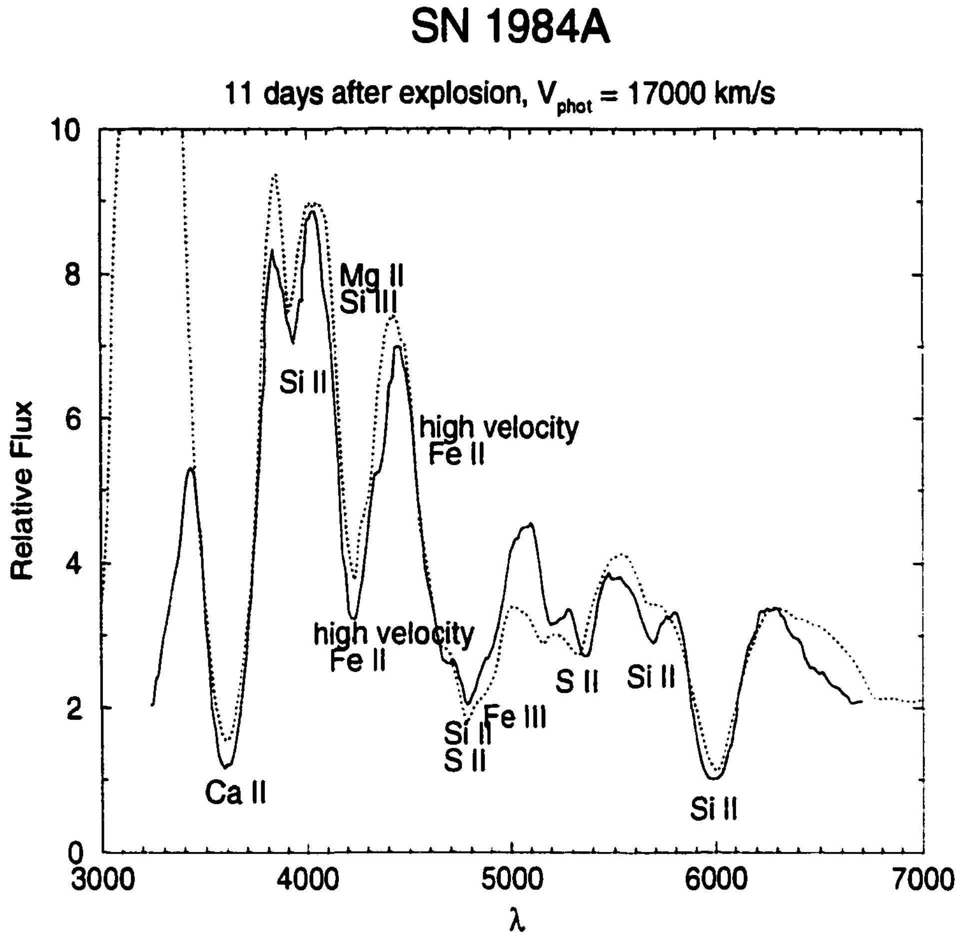

Figure 7.12: The observed spectrum is from Wegner and McMahan (1987).

is also very strong. The S II lines near 5300 Å are blended together. But, the most interesting features are found near 4200 Å and near 4700 Å. In the synthetic spectrum, these lines are fit by high–velocity Fe II that is detached at 25,000 km s^{-1}. Note that T_{exc} of Fe II is different from T_{exc} of other ions. This is because if T_{exc} of Fe II is larger than 10,000 K, serious problems are caused elsewhere in the synthetic spectrum. This also implies that the outer layers of this supernova are cooler than the inner layers. Hatano et al. (1999b) also used the high–velocity Fe II to fit the -12 day spectrum of SN 1994D. In the synthetic spectrum, Mg II, Si III, and Fe III are also used to improve the fit. But, their existence is not very clear.

7.2.2 SN 1997bq

ion	Mg II	Ca II	Si II	O I	S II	Fe III	Fe II
τ	0.7	300	7.0	0.5	2.0	1.0	1.0
v_{min}	...	...	...	...	...	...	22
v_{max}	40	30	40	40	16	18	29
v_e	3.0	3.0	3.0	3.0	3.0	3.0	3.0
T_{exc}	15	15	15	15	15	15	10

Table 7.13: Fitting Parameters for Figure 13

Fig. 13 presents an analysis of a spectrum of SN 1997bq, that is well before maximum light. Some of the important fitting parameters are as follows: v_{phot} = 15,000 km s^{-1}, v_{max} = 40,000 km s^{-1}, and T_{bb} = 15,000 K. Fitting parameters for each ion are shown in Table 13.

As expected, this spectrum is very similar to the spectrum of SN 1984A (previous figure). All spectral lines are very broad and deep. The Ca II H&K line and the Si II line due to λ6355 are very conspicuous. And, the high-velocity Fe II lines are also very strong. Once again, T_{exc} of Fe II, that is detached at 22,000 km s^{-1}, is different from T_{exc} of other ions. Unlike the previous figure, this spectrum extends to the near infrared. There, the Ca II infrared triplet line is very strong as expected. The O I + Mg II feature near 7300 Å is also very broad and deep. In the synthetic spectrum, v_{phot} is 15,000 km s^{-1}, which is already quite high. But, the absorption minimum of the Si II feature near 6000 Å suggests that v_{phot} should be even higher.

7.2.3 SN 1999cl

Fig. 14 presents an observed spectrum of SN 1999cl, whose epoch is unknown. From its slope of the continuum and narrow Na I lines, it is obvious that this supernova is highly extinguished by dust (Garnavich et al. 1999). We use the value of the color excess E(B-V) = 1.0 estimated by Garnavich et al. to correct the spectrum. Fig. 15 shows the corrected spectrum.

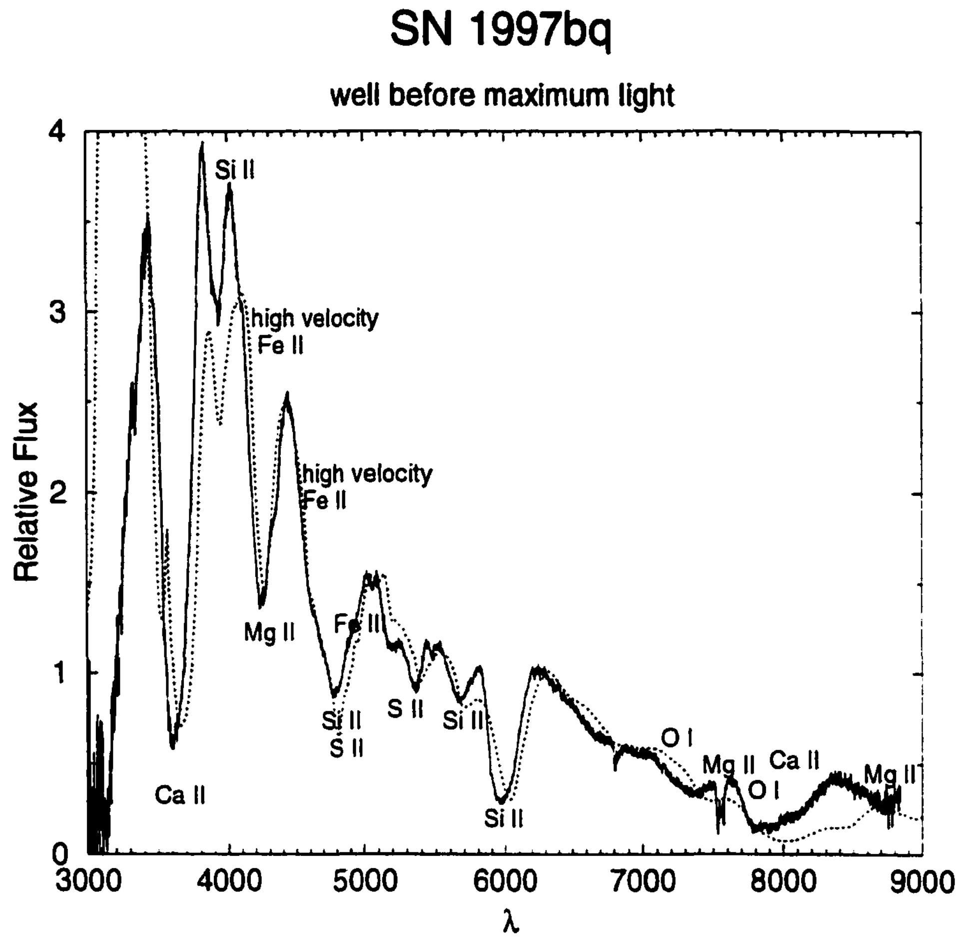

Figure 7.13: The observed spectrum is provided by Peter Garnavich.

ion	Mg II	Ca II	Si III	Si II	S II	Fe III	Fe II
τ	1.5	600	0.5	3.0	1.0	2.0	0.7
v_{min}	...	...	...	...	...	...	22
v_{max}	40	30	40	40	40	40	29
v_e	3.0	3.0	3.0	3.0	3.0	3.0	3.0
T_{exc}	14	14	14	14	14	14	10

Table 7.14: Fitting Parameters for Figure 15

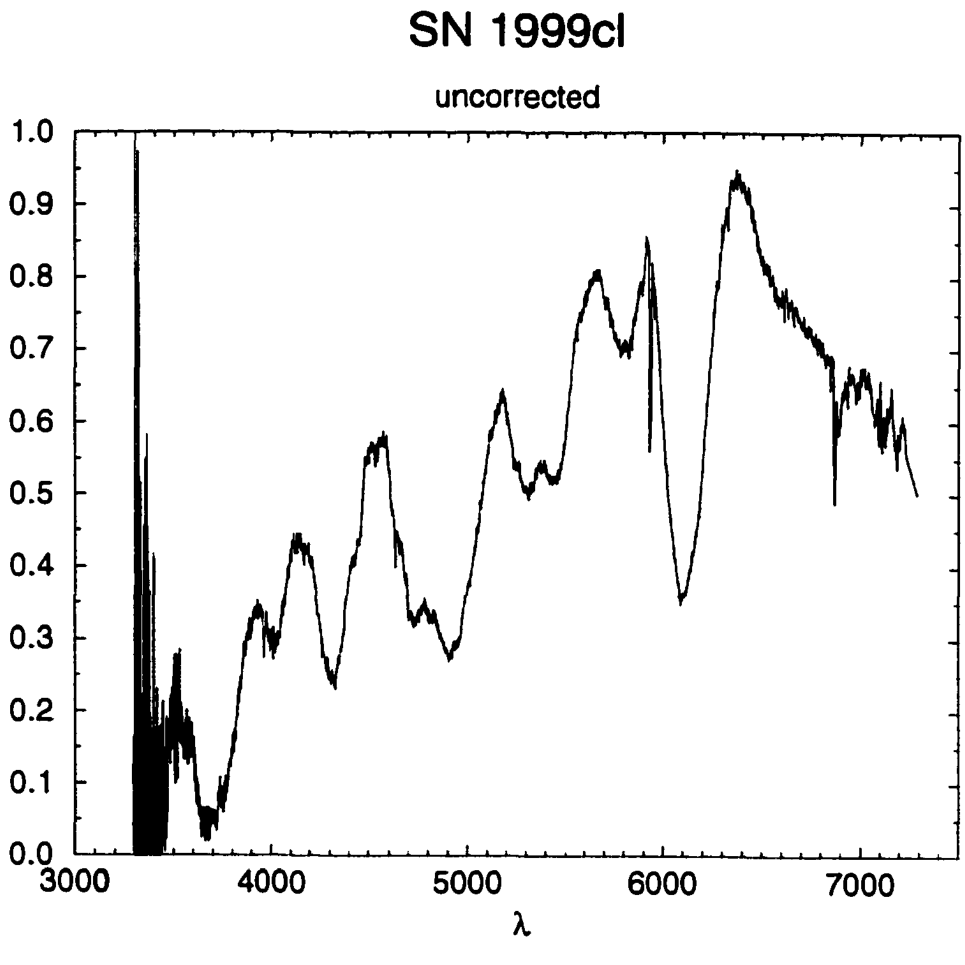

Figure 7.14: The observed spectrum is provided by Peter Garnavich.

Fig. 15 presents an analysis of a spectrum of SN 1999cl, whose epoch is unknown. Some of the important fitting parameters are as follows: v_{phot} = 14,000 km s^{-1}, v_{max} = 40,000 km s^{-1}, and T_{bb} = 14,000 K. Fitting parameters for each ion are shown in Table 14.

This spectrum is very similar to the spectra of SN 1984A and SN 1997bq (previous two figures). The spectral features are very broad and deep. In particular, the S II lines near 5300 Å are blended together. Once again, the high-velocity Fe II is required to fit the observed features. Notice again that T_{exc} of Fe II is different from T_{exc} of other ions. It is interesting to see that the velocity interval of Fe II in this supernova is same as the interval in SN 1997bq. And, when the optical depth of Ca II is this large in the synthetic spectrum, another Ca II feature appears near 6800 Å.

7.2.4 Discussion

Here, we shall summarize the constraints we've found by analyzing the spectra of three high-velocity SNe Ia. First of all, as Branch (1987a) has suggested, we've found only "normal" SNe Ia ions in these spectra. But, the ejection velocity of these ions is much larger than the velocity normally seen in the spectra of other SNe Ia. We've found that v_{phot} of these SNe is at least about 15,000 km s^{-1}or even higher. Thus, these ions must be present above 15,000 km s^{-1}. Among those ions, the existence of Si II, S II, Ca II, and high-velocity Fe II is definite. The existence of O I and Mg II is probable. And, the existence of Si III and Fe III is unclear. In the synthetic spectra, Si III and Fe III are used just to improve the fit. The only detached ion is Fe II which is present in the velocity space of about 22,000 $\sim$ 30,000 km s^{-1}. And, T_{exc} of Fe II cannot be hotter than 10,000 K.

The best SN Ia explosion model to date is the model W7 (Nomoto et al. 1984, Branch et al. 1985). This model can reproduce the near maximum light spectra of normal SNe Ia very well. But, this model cannot satisfy most of the constraints discussed above. First of all, the maximum velocity of Si and S is about 15,000 km

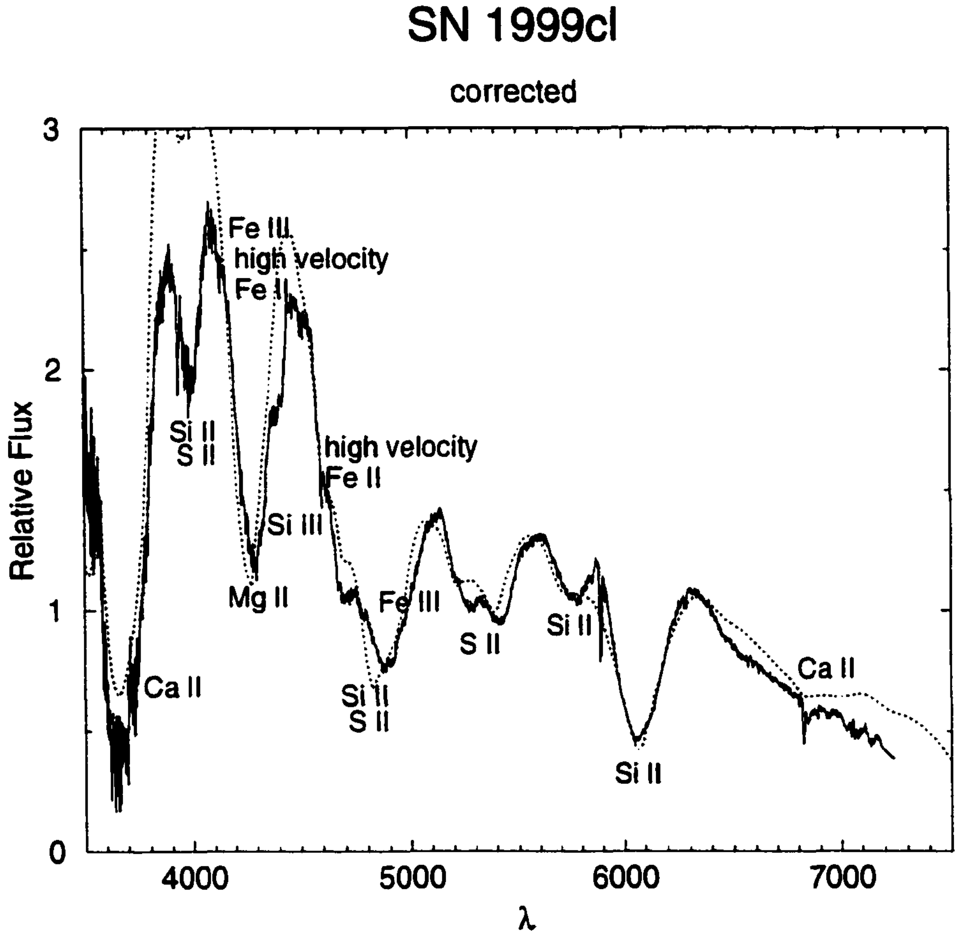

Figure 7.15: The observed spectrum is provided by Peter Garnavich.

s^{-1}. And, the maximum velocity of Ca is about 13,000 km s^{-1}. These velocities are too slow for the spectra of the high-velocity SNe Ia. There is, however, a small amount of Fe above 15,000 km s^{-1}which may represent the high-velocity Fe II.

There are, however, some other models that may satisfy some of the constraints discussed above. For example, delayed detonation models, N21 and N32 (Khokhlov et al. 1993), produce Si, S, and Ca above 15,000 km s^{-1}. Also, low density detonation model, DET2, by Khokhlov et al. produces Si, S, and Ca above 15,000 km s^{-1}. But, a problem of these models is that there is no high-velocity Fe above 22,000 km s^{-1}. And, the models CS15DD1 - DD3 by Iwamoto et al. (1999) and the model CDT3 by Shigeyama et al. (1992) predict high-velocity Si, S, and Ca above 15,000 km s^{-1}as well. But, none of these models produces high-velocity Fe above 22,000 km s^{-1}.

One way to solve this Fe problem is to introduce primordial elements. But, there are some models that produce high-velocity Fe above 22,000 km s^{-1}. Models 6 and 8 by Livne and Arnett (1995) predict the high-velocity Fe in this velocity space. And, there are some Si, S, and Ca above 15,000 km s^{-1}in these two models. But, a problem may be that these models predict a large amount of very high-velocity He, which is not detected in the spectra of high-velocity SNe Ia. If infrared spectra of these high-velocity SNe Ia are available, this problem should be clarified by checking He I λ10830.

A spectrum of high-velocity SNe Ia can be characterized by: 1) very large blueshifts seen in each feature, 2) very broad lines, 3) very strong Si II, Ca II, and O I/Mg II lines which may be due to cool temperature (Hatano et al. 2000b), 4) S II lines near 5300 Å that are blended together, and 5) very high-velocity, detached Fe II. Fig. 16 compares three high-velocity spectra discussed in this section and two additional spectra that satisfy these five conditions. First, one would notice a remarkable homogeneity among these five spectra. One spectrum is very much like another spectrum. But, the epoch of these spectra is very different. The spectrum of SN 1984A is 7 days before maximum light, and the phase that satisfies above five conditions ("high-velocity" phase) continues at least until a few days before maximum light (Barbon et

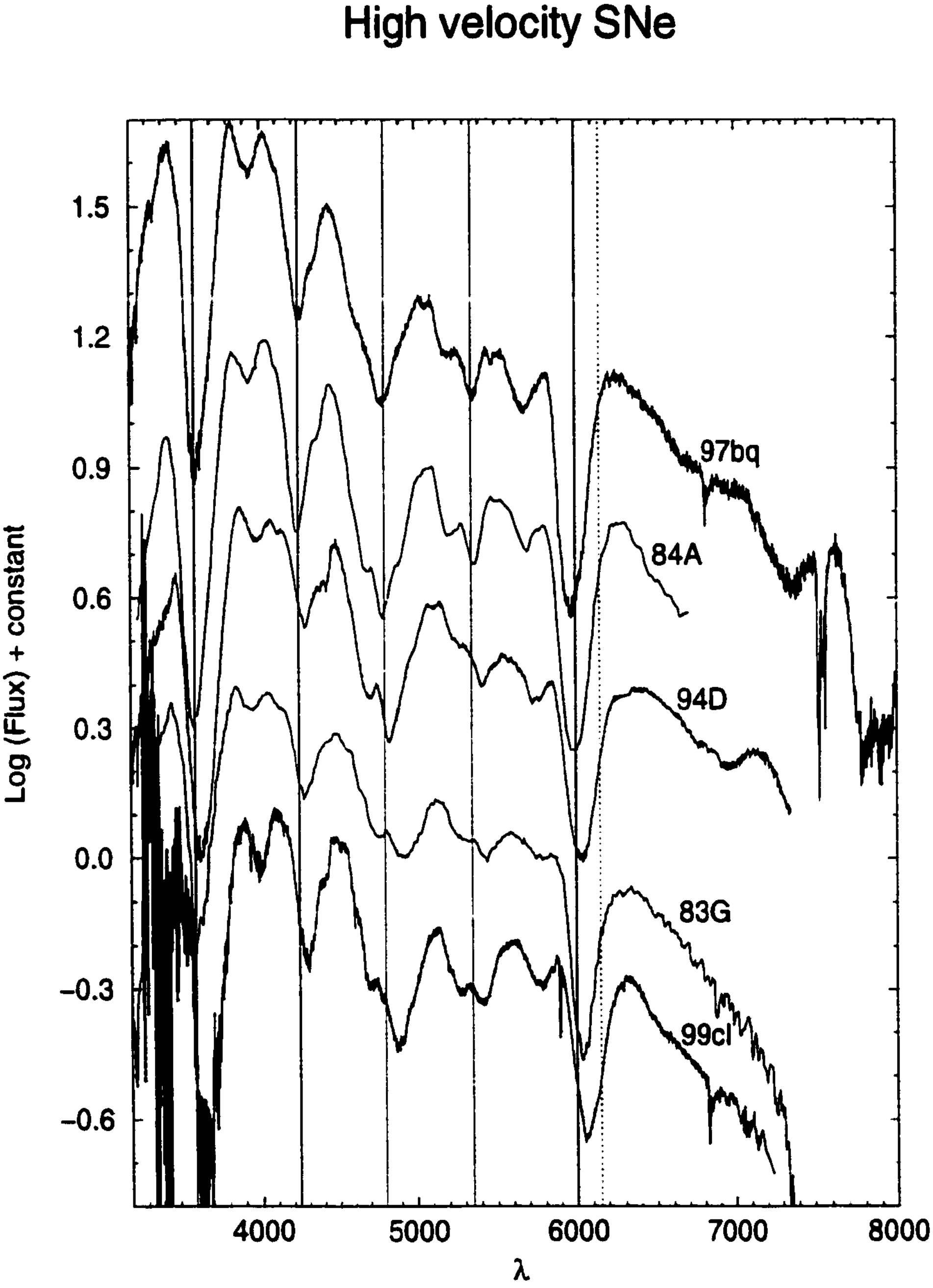

Figure 7.16: The observed SN 1994D (12 days before maximum light) spectrum is from Filippenko (1997b). The observed SN 1983G spectrum (near maximum light) is from McCall et al. (1984). The other spectra are from previous figures.

al. 1989). On the other hand, the spectrum of SN 1994D is 12 days before maximum light, and the high-velocity phase continues only until 10 days before maximum light (Patat et al. 1996, Hatano et al. 2000b). And, the spectrum of SN 1983G is near maximum light; thus, the high-velocity phase lasts at least until the maximum light. Therefore, this means that the duration of the high-velocity phase is different among SNe Ia.

SN 1994D is a very normal SN Ia. But, it has a phase in which the spectrum is identical to a spectrum of SN 1984A, a high-velocity SN Ia. This implies that many other SNe Ia may go through the high-velocity phase. But, in order to see the high-velocity phase in the spectra of normal SNe Ia, it would be necessary to find a SN well before maximum light. On the other hand, not all SNe Ia go through the high-velocity phase. For example, we have seen a spectrum of SN 1990N, that is 14 days before maximum light, in Leibundgut et al. (1991). But, the spectrum does not satisfy most of the conditions for the high-velocity phase. And, a spectrum of SN 1998aq that is 12 days before maximum light (earlier in this chapter) also does not satisfy these conditions. And, a spectrum of the peculiar SN 1991T, that is 13 days before maximum light (Fisher et al. 1999), obviously does not satisfy these conditions.

Hatano et al. (2000b) discuss about the nature of the high-velocity SNe Ia. According to Hatano et al., these high-velocity SNe Ia may be the results of the delayed detonation type explosions. Hatano et al. also give the values of v_{10}(Si II), the velocity inferred from the absorption minimum of the Si II λ6355 at 10 days after the maximum light. The fastest value, among three SNe discussed above, is found in SN 1983G whose duration of the high-velocity phase is the longest. The second fastest value is found in SN 1984A whose duration of the high-velocity phase seems to be the second longest. And, the slowest value is found in SN 1994D whose duration of the high-velocity phase is the shortest. Therefore, the larger the value of v_{10}(Si II), the longer the duration of the high-velocity phase, which is a reasonable result. The longer duration implies more high-velocity elements. Thus, it is possible that the duration of the high–velocity phase is related to the location at which the deflagration turns into a detonation. But, in order to have a better understanding about the nature of these high–velocity SNe Ia, it would be necessary to have more data, especially very early–time spectra of SNe Ia.

Chapter 8

On the Spectroscopic Diversity of Type Ia Supernovae

ABSTRACT

A comparison of the ratio of the depths of two absorption features in the spectra of Type Ia supernovae (SNe Ia) near the time of maximum brightness with the blueshift of the deep red Si II absorption feature 10 days after maximum shows that the spectroscopic diversity of SNe Ia is multi-dimensional. There is a substantial range of blueshifts at a given value of the depth ratio. We also find that the spectra of a sample of SNe Ia obtained a week before maximum brightness can be arranged in a "blueshift sequence" that mimics the time evolution of the pre-maximum-light spectra of an individual SN Ia, the well observed SN 1994D. Within the context of current SN Ia explosion models, we suggest that some of the SNe Ia in our sample were delayed-detonations while others were plain deflagrations.

8.1 Introduction

Advancing our understanding of the diversity among Type Ia supernovae (SNe Ia) is important for identifying the nature of the progenitor binary systems and the explosion mechanisms, as well as for boosting confidence in using SNe Ia as empirical distance indicators for cosmology. To first order, SNe Ia can be divided into normal events that are highly but not perfectly homogeneous, and peculiar events like the powerful SN 1991T and the weak SN 1991bg. The next approximation is to regard SNe Ia as a one–parameter sequence of events, using a photometric observable such as Δm_{15} , the decline of the B magnitude during the first 15 days after the time of maximum brightness (Phillips 1993; Phillips et al. 1999; Suntzeff et al. 1999), or using a spectroscopic observable such as $\mathcal{R}$(Si II), the ratio of the depths of two absorption features near 5800 and 6100 Å that ordinarily are attributed to Si II λ5972 and Si II λ6355, respectively (Nugent et al. 1995a). The Δm_{15} and $\mathcal{R}$(Si II) parameters are observed to be tightly correlated (Nugent et al. 1995a; Garnavich et al. 2000), and because they also correlate with peak absolute magnitude they can be regarded as measures of the explosion strength. A one–parameter description of SNe Ia is useful, and in the context of Chandrasekhar–mass explosions it can be interpreted in terms of a variation in the mass of ejected ^{56}Ni (e.g., Wheeler et al. 1995; Höflich et al. 1996).

However, a one–parameter sequence does not completely account for the SN Ia diversity. Hamuy et al. (1996) found that some light curves having similar values of Δm_{15} show significant differences of detail, and it has been shown that a *two–parameter* luminosity correction using the $B-V$ color and Δm_{15} is both necessary and (so far) sufficient to standardize SNe Ia to a common luminosity (Tripp 1998; Tripp & Branch 1999; Parodi et al. 2000). It also has been noted that some SNe Ia with normal-looking spectra (i.e., having only lines of the usual ions) have exceptionally high blueshifts of their absorption features (e.g., Branch 1987a, 1998), and Wells et al. (1994) noted a lack of correlation between the blueshift of the Si II λ6355 absorption near the time of maximum brightness and the Δm_{15} parameter, in a small sample of well observed SNe Ia (see also Patat et al. 1996). In this chapter, we extend the discussion by showing more clearly that the spectroscopic diversity among SNe Ia is multi–dimensional.

8.2 Data

As a measure of the blueshift of a SN Ia spectrum we adopt the parameter used by Branch & van den Bergh (1993), which we denote as v_{10}(Si II): it is the velocity that corresponds to the blueshift of the flux minimum of the deep absorption feature near 6100 Å, attributed to Si II λ6355, 10 days after the time of maximum brightness. We use the data of Branch & van den Bergh, as well as additional data for the following events: SN 1984A (Barbon, Iijima, & Rosino 1989); SN 1989B (Wells et al. 1994); SN 1991T (Fisher et al. 1999); SNe 1992A and 1998bu (Jha et al. 1999); SN 1994D (Patat et al. 1996; Filippenko 1997b); SN 1997br (Li et al. 1999); and SN 1999by (Bonanos et al. 2000).

As another spectroscopic observable we use the $\mathcal{R}$(Si II) parameter. Most of the $\mathcal{R}$(Si II) values that we use are from Garnavich et al. (2000). For events for which they give several slightly different values of $\mathcal{R}$(Si II), measured at several epochs, we use the median value. For a few other events we have estimated $\mathcal{R}$(Si II) from published spectra that are referenced by Branch & van den Bergh (1993), following the definition of $\mathcal{R}$(Si II) by Nugent et al. (1995a). For another nine events for which spectra suitable for measuring $\mathcal{R}$(Si II) are unavailable, we have used the observed value of Δm_{15} (Phillips 1993; Schaefer 1996, 1998; Riess et al. 1999a; Suntzeff et al. 1999) to "predict" the value of $\mathcal{R}$(Si II), with the help of the tight relation between $\mathcal{R}$(Si II) and Δm_{15} that is displayed by Garnavich et al. (2000).

The characteristic uncertainties are 500 km s^{-1} in v_{10}(Si II) and 0.04 in $\mathcal{R}$(Si II), which are not negligible but not large enough to strongly affect our conclusions.

8.3 Results

8.3.1 $\mathcal{R}$(Si II) versus v_{10}(Si II)

The $\mathcal{R}$(Si II) parameter is plotted against v_{10}(Si II) in Figure 1. If SNe Ia did behave as a simple one–parameter sequence, with the mass of ejected ^{56}Ni being the fundamental physical parameter, we would expect $\mathcal{R}$(Si II) to decrease smoothly as v_{10}(Si II) increases. The more powerful the event, the higher the velocity at the outer edge of the core of iron–peak elements, and therefore the higher the velocity of the silicon–rich layer. For the sample of Figure 1 taken as a whole, this obviously is not the case. Of course, it is possible that the peculiar weak SNe 1991bg, 1999by, and 1986G, and/or the peculiar powerful SNe 1991T and 1997br, comprise physically distinct subgroups of SNe Ia. It is interesting that when we disregard these, and restrict our attention to the spectroscopically normal SNe Ia, it is not even clear that there is any correlation between $\mathcal{R}$(Si II) and v_{10}(Si II) at all. Normal SNe Ia that have similar values of $\mathcal{R}$(Si II) can have substantially different values of v_{10}(Si II), so a one–parameter sequence cannot completely account for the spectroscopic diversity of normal SNe Ia.

If we were able to use blueshifts measured at a fixed time after explosion, rather than at a fixed time with respect to maximum brightness, Figure 1 would look slightly different because of the diversity in SN Ia rise times from explosion to maximum brightness (Riess et al. 1999b), but this would not change our conclusion about the need for more than a one–dimensional spectroscopic sequence.

8.3.2 Pre–maximum spectra

Now we turn to the diversity among pre–maximum–light spectra of SNe Ia. Figure 2 shows spectra of five events, all obtained about one week before the time of maximum brightness, arranged in a "blueshift sequence". The two vertical lines, drawn as an aide to the eye, are blueshifted by 15,000 km s^{-1} with respect to Si II λ6355 and Ca II

Fig 1

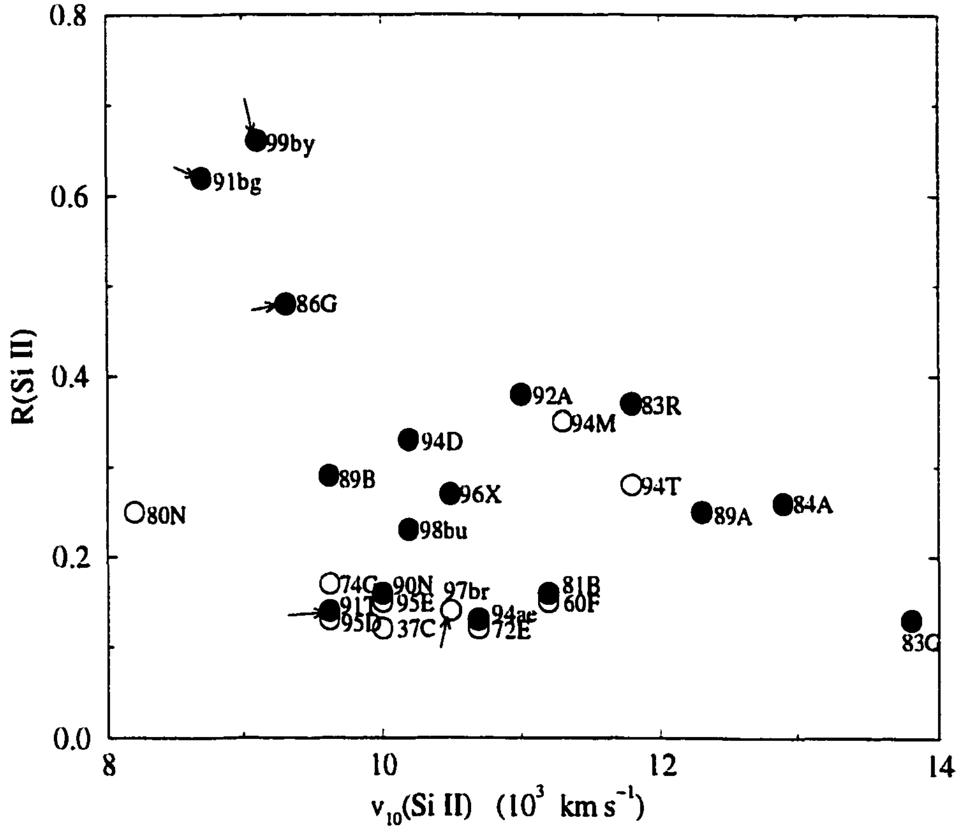

Figure 8.1: The $\mathcal{R}$(Si II) parameter is plotted against v_{10}(Si II). Arrows denote spectroscopically peculiar SNe Ia. Open symbols mean that $\mathcal{R}$(Si II) has been obtained from a relation between Δm_{15} and $\mathcal{R}$(Si II). Characteristic uncertainties are 0.04 in $\mathcal{R}$(Si II) and 500 km s^{-1} in v_{10}(Si II).

Fig 2

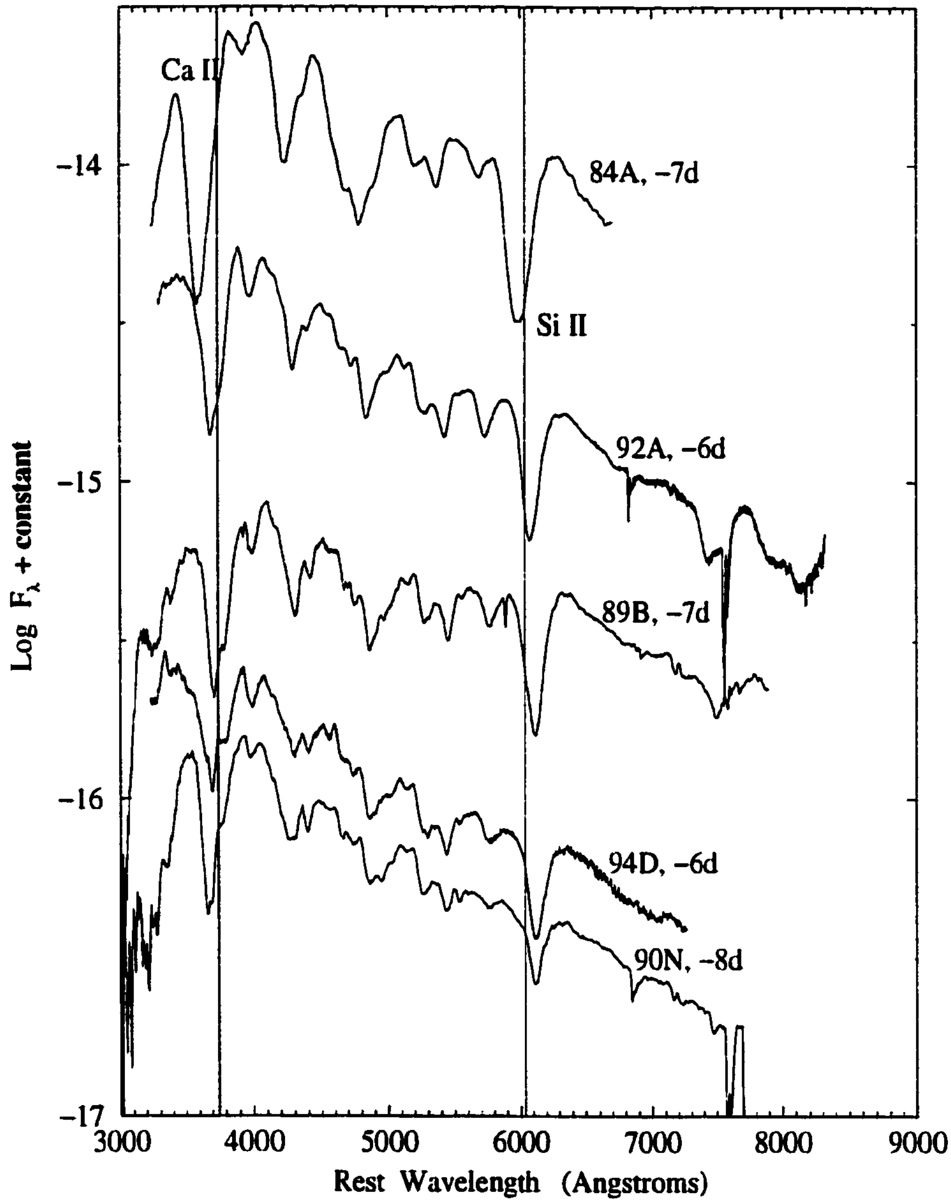

Figure 8.2: Spectra of five SNe Ia about a week before the time of maximum light (SN 1984A: Wegner & McMahan 1987; SN 1992A: Kirshner et al. 1993; SN 1989B: Wells et al. 1994; SN 1994D: Filippenko 1997b; SN 1990N: Leibundgut et al. 1993) are arranged in a blueshift sequence. The vertical lines are blueshifted by 15,000 km s^{-1} from λ6355 (Si II) and λ3945 (Ca II). The vertical displacements are arbitrary.

$\lambda3945$. Some things to notice in Figure 2 are that (1) as is to be expected, the absorption features are broader in the higher–blueshift events; (2) the absorption features tend to be deeper in the higher–blueshift events (not necessarily expected); and (3) the Ca II absorption appears as a single feature in the high–blueshift SNe 1984A and 1992A, while it appears split in the lower blueshift SNe 1989B, 1994D, and 1990N.

For comparison with Figure 2, Figure 3 shows a time series of pre–maximum-light spectra of the particularly well observed SN 1994D. The degree to which Figure 3 resembles Figure 2 is intriguing. The −12 day spectrum of SN 1994D in Figure 3 looks much like the −7 day spectrum of SN 1984A in Figure 2; the SN 1994D absorptions are at their deepest at the earliest times when the blueshifts are the highest; and the Ca II absorption of SN 1994D evolves from unsplit to split. It is almost as if normal SNe Ia follow a standard pattern of pre–maximum spectroscopic evolution after all, but their spectra are not in phase with respect to the time of maximum brightness. (This statement should not be taken too literally, and certainly it cannot be said of the spectroscopically peculiar SNe Ia; there was no pre–maximum phase at which the spectrum of SN 1994D resembled that of SN 1991bg–like or SN 1991T–like events.)

Figure 4 shows some comparisons of observed pre–maximum SN Ia spectra with synthetic spectra that have been generated with the parameterized spectrum–synthesis code SYNOW. [Brief descriptions of the code can be found in recent applications of SYNOW, e.g., Fisher et al. (1999), Millard et al. (1999), Hatano et al. (1999b, 2000a); details are in Fisher (2000)]. The top panel compares the −6 day spectrum of SN 1994D with a best–fit synthetic spectrum that has a velocity at the photosphere of v_{phot}= 11,000 km s^{-1} and includes lines of O I, Mg II, Si II, Si III, S II, Ca II, and Fe II. The second panel compares the −6 day spectrum of SN 1992A with two synthetic spectra. In one of them (dashed line) the SYNOW parameters are the same as in the top panel, except that v_{phot} has been increased from 11,000 to 13,000 km s^{-1}; this produces about the right absorption–feature blueshifts for SN 1992A, but most of the synthetic absorptions are too weak. In the other synthetic spectrum of the middle panel (dotted line), the line optical depths of O I, Si II, and S II have

Fig 3

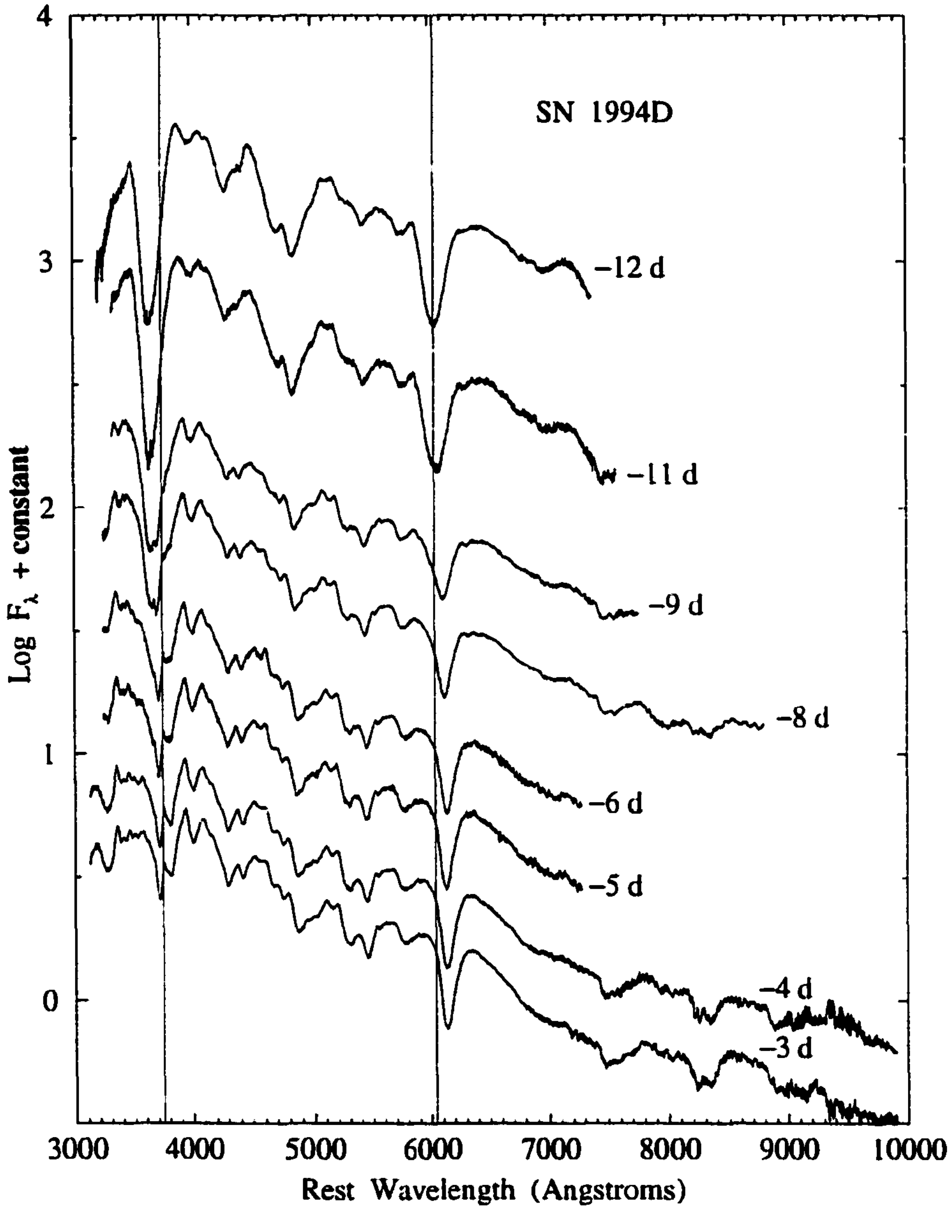

Figure 8.3: A time series of pre-maximum spectra of SN 1994D (Patat et al. 1996; Filippenko 1997b, and unpublished). The vertical lines are the same as in Figure 2.

Fig 4

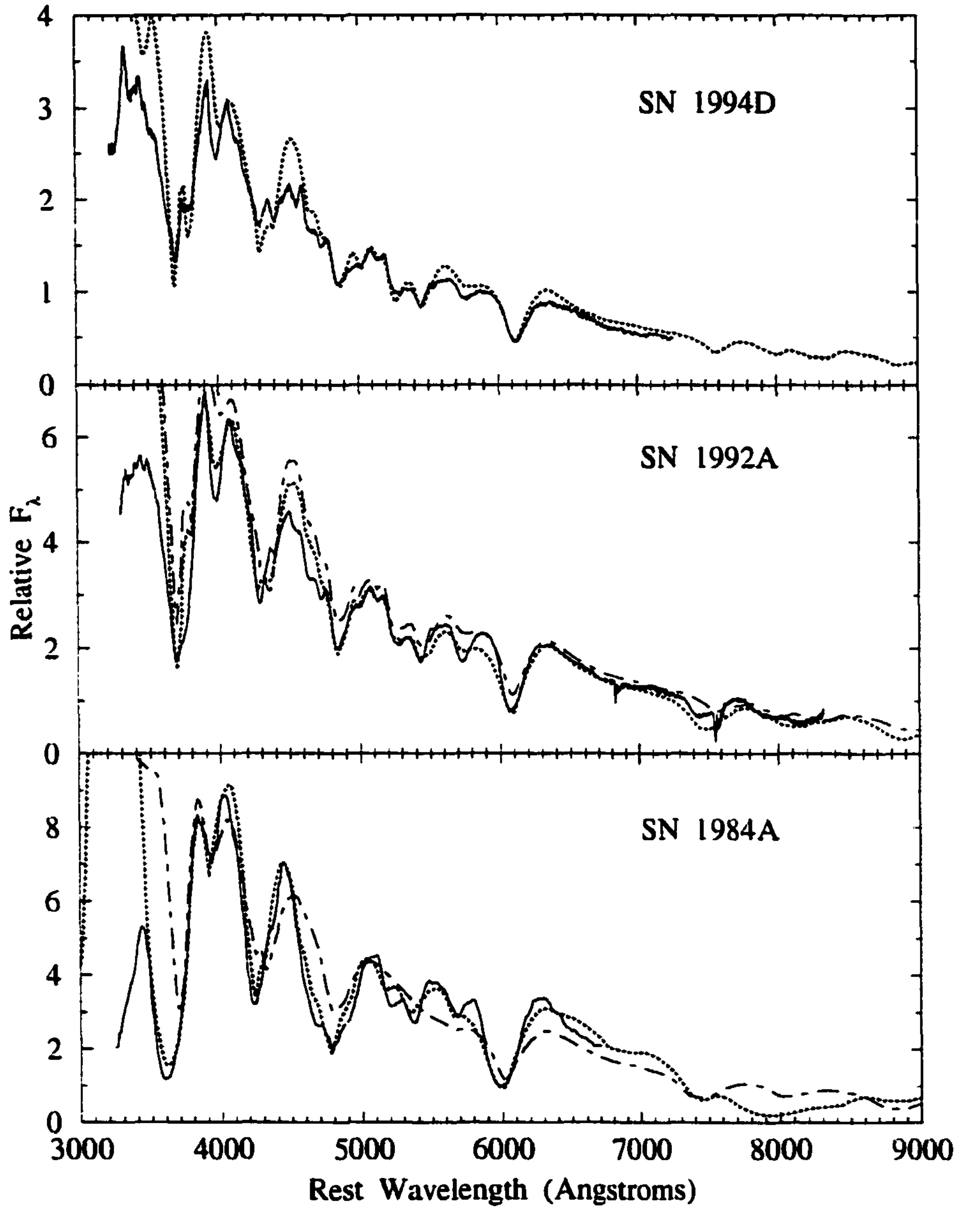

Figure 8.4: Comparisons of observed spectra (solid curves) of SN 1994D at −6 days (top panel), SN 1992A at −6 days (middle panel), and SN 1984A at −7 days (bottom panel) with SYNOW synthetic spectra. See the text for descriptions of the synthetic spectra.

been increased to achieve a better fit. Similarly, in the bottom panel the −7 day spectrum of SN 1984A is compared to two synthetic spectra. In one of them (dashed line) only v_{phot} has been changed, from 13,000 to 17,000 km s^{-1} to get the right blueshifts. In the other (dotted line), the line optical depths of Mg II, Si II, Ca II, and Fe II have been further increased [and a weak high–velocity Fe II component (cf. Hatano et al. 1999b) has been introduced] to make the synthetic absorptions strong enough. Figure 4 shows that these rather different pre–maximum spectra of SNe 1994D, 1992A, and 1984A can be matched well with lines of the same ions, but with different photospheric velocities and line optical depths. In general, the higher the blueshift of the spectrum, the higher the line optical depths.

8.4 Discussion

Attempting an in–depth interpretation of the causes of the spectroscopic diversity illustrated in this chapter would be premature, but a brief discussion is in order. As stressed above, the main point is that spectroscopically normal SNe Ia that have similar values of $\mathcal{R}$(Si II) (or Δm_{15}) have a significant range in v_{10}(Si II), which is not what we would expect if SNe Ia behaved as a simple one–parameter sequence of events. One possible explanation is that two or more explosion mechanisms are involved. In this regard it is noteworthy that Lentz et al. (2000b) find from detailed NLTE calculations that some of the published delayed–detonation models can account for the high Si II blueshift of SN 1984A. It may be that the seven events ranging diagonally from SN 1992A to SN 1983G in Figure 1 are delayed detonations having a range of strengths, while the other spectroscopically normal events (perhaps excepting the very low–blueshift SN 1980N) are plain deflagrations. From this point of view it seems useful to regard the $\mathcal{R}$(Si II) axis as a measure of the ejected mass of ^{56}Ni and the v_{10}(Si II) axis as a measure of the amount of matter ejected at high velocity; the latter is much higher in delayed detonations than in plain deflagrations (Lentz et al. 2000b). It is not clear whether the weak SN 1991bg–like events should be regarded as weak delayed detonations, weak deflagrations, or something else. For suggestions that the powerful SN 1991T–like events may come from super–Chandrasekhar white dwarf merger products, see Fisher et al. (1999) and Hatano et al. (2000a).

We should keep in mind that the distribution of events in Figure 1 also could be affected by asymmetries. Branch & van den Bergh (1993) argued, on the basis of a perceived connection between v_{10}(Si II) and parent–galaxy type, that the whole range of v_{10}(Si II) values cannot be attributed entirely to asymmetries, and SNe Ia in general are observed to have low polarization (Wang et al. 1996), but the possibility that asymmetry does play some role in Figure 1 is not excluded. An asymmetry in the ejected matter is expected to be produced by the presence of a donor star (Marietta et al. 2000). The explosion also could be inherently asymmetric; for example, Livne (1999) finds that a deflagration–detonation transition that begins at a single point, which is more realistic than beginning simultaneously all over a spherical shell, would produce significant asymmetry in the ejected matter.

Figures 2, 3, and 4 raise some additional questions. Why are the line optical depths higher when the blueshifts are higher? In the Sobolev approximation, line optical depths are proportional to the time since the explosion (owing to the decreasing velocity gradient and the increasing size of the resonance region), and this direct time dependence is only partially offset by the decreasing density at the photosphere. Furthermore, it is unlikely that the mass fractions of silicon and calcium *decrease* with velocity in the outer layers of SNe Ia. Therefore, temperature evolution seems to be required to account for the decreasing line strengths that we see in Figure 3. If the temperature of the line–forming layers of SN 1994D increased during the rise towards maximum brightness [as indicated by broad–band photometry (Richmond et al. 1995; Patat et al. 1996; Meikle et al. 1996)] the Ca II and Si II optical depths would have decreased as the optical depths of the weaker Si III and Fe III lines increased (Hatano et al. 1999a); this seems to have been the case for SN 1994D (cf. Hatano et al. 1999b).

If temperature evolution is the primary reason for the spectral evolution during the rise to maximum of SN 1994D, temperature differences may also be responsible for the blueshift sequence of Figure 2. The resemblance of the spectrum of SN 1994D at -12 days to that of SN 1984A at -7 days may mean that the high–velocity layers of SN 1984A at -7 days were still as cool as those of SN 1994D at -12 days. The higher densities in the high–velocity layers of delayed detonations are likely to cause them to be cooler than those of plain deflagrations at a fixed time after explosion.

Metallicity differences also can produce some differences in the pre–maximum spectra of SNe Ia, although they cannot significantly affect the post–maximum v_{10}(Si II) parameter (H"oflich, Wheeler, & Thielemann 1998; Lentz et al. 2000a).

Our suggestion that Figure 1 is populated by both delayed detonations and deflagrations seems to be a reasonable working hypothesis within the context of current SN Ia explosion models, but there are many uncertainties associated with such models (Hillebrandt & Niemeyer 2000). Our understanding of the causes of the spectroscopic diversity of SNe Ia is still in a rudimentary state. Many more high–quality observed spectra and much more spectroscopic analysis are needed.

It is our pleasure to thank Darrin Casebeer, Dean Richardson, and Thomas Vaughan for helpful discussions. This work was supported by NSF grants AST-9731450 and AST–9417213 and by NASA grant NAG5-3505.

Chapter 9

Conclusion

This thesis generally consists of two portions. The first portion presented ion signatures in supernova spectra — optical, ultraviolet, and infrared. We discussed about the basic physics regarding the line formation in the atmosphere of supernovae. We considered six different compositions that may be seen in supernovae. Then, we provided the optical depth of each ion, which may be seen in the spectra of supernovae, plotted as a function of the temperature. We also provided a SYNOW synthetic spectrum of each ion that may become strong enough to be identifiable in the spectra of supernovae. These synthetic spectra cover the wavelength region ranging from near ultraviolet to near infrared. Therefore, this first portion may be used as the "atlas" to study the spectra of all types of supernovae, at any photospheric phase, at optical, ultraviolet, and infrared.

The second portion presented an analysis of the spectra of type Ia supernovae — from the peculiar and hot SN 1991T like events, to a normal SN 1994D, and to the peculiar and cool SN 1991bg like events. We confirmed that the temperature is the fundamental cause of the spectroscopic sequence among type Ia supernovae. We found out that the composition structure of these peculiar events is not fundamentally different from that of the normal type Ia supernovae. We proved that the extreme temperature is the main cause of most of the peculiarities seen in these peculiar events.

And, even among normal type Ia supernovae, there are some spectral evolutions as a function of the temperature.

However, the temperature is not the whole story. We showed that there is another spectroscopic sequence among normal type Ia supernovae as a function of the velocity — from the slow SN 1990N to the fast SN 1984A. We, once again, showed that the composition structures among these supernovae are not fundamentally different. Elements are just moving at the different velocities. And, the fastest supernovae are also relatively cool events. But, the spectra of these high–velocity events look very different from the spectra of the cool SN 1991bg like supernovae, which are also very slow events. On the other hand, the slowest supernovae among the normals are also relatively hot events. And, the velocity of the hot SN 1991T like supernovae is relatively slow. What does this mean?

This tells us that the spectroscopic sequence among type Ia supernovae is multi–dimensional. And, more than one explosion mechanisms are involved, as discussed in the previous chapter. But, it is possible to discover "one" of many sequences. The one is the temperature sequence, and the another is the velocity sequence. And, there could be many more "one dimensional" sequences that are part of the multi–dimensional structure. However, we have at least proved that the composition of all type Ia supernovae is essentially the same. Therefore, this thesis has provided the one, very important step toward the complete understanding of type Ia supernovae.

We would like to conclude this thesis by introducing a recent supernova SN 2000H. Fig. 1 presents its SYNOW analysis. This supernova was first considered as a peculiar, cool type Ia supernova, like SNe 1991bg and 1999by, by the observers of this spectrum. They suggested that the feature near 6200 Å is attributed to Si II λ6355, which is asymetric and extremely slow. And, the feature near 5700 Å is the "580 nm Si II" feature, which makes the Si II depth ratio quite large. Therefore, they suggested that this supernova is more extreme than SNe 1991bg and 1999by.

But, our SYNOW analysis showed that the feature near 5700 Å is actually attributed to a He I line, and two other weaker He I lines are seen. And, the asymetric feature is actually a blend of Si II $\lambda 6355$ and Hα, and a hint of Hβ may be seen. This analysis was later confirmed by the Italian group who has found out that a later time spectrum is dominated by He I lines, and hydrogen lines are also strong. Thus, we were the first ones who have provided these He I identifications. This, once again, proved the power of SYNOW.

But, how should we classify this supernova? It has both strong Si II $\lambda 6355$ and strong Hα. And, He I lines are also very strong. We call it a type IIb supernova, but there could be other ways of classification. This surely is a new class of supernova. Thus, we have not seen all types of supernovae, yet. In the future, more peculiar supernovae shall be discovered. At the time, the power of SYNOW shall be proved again.

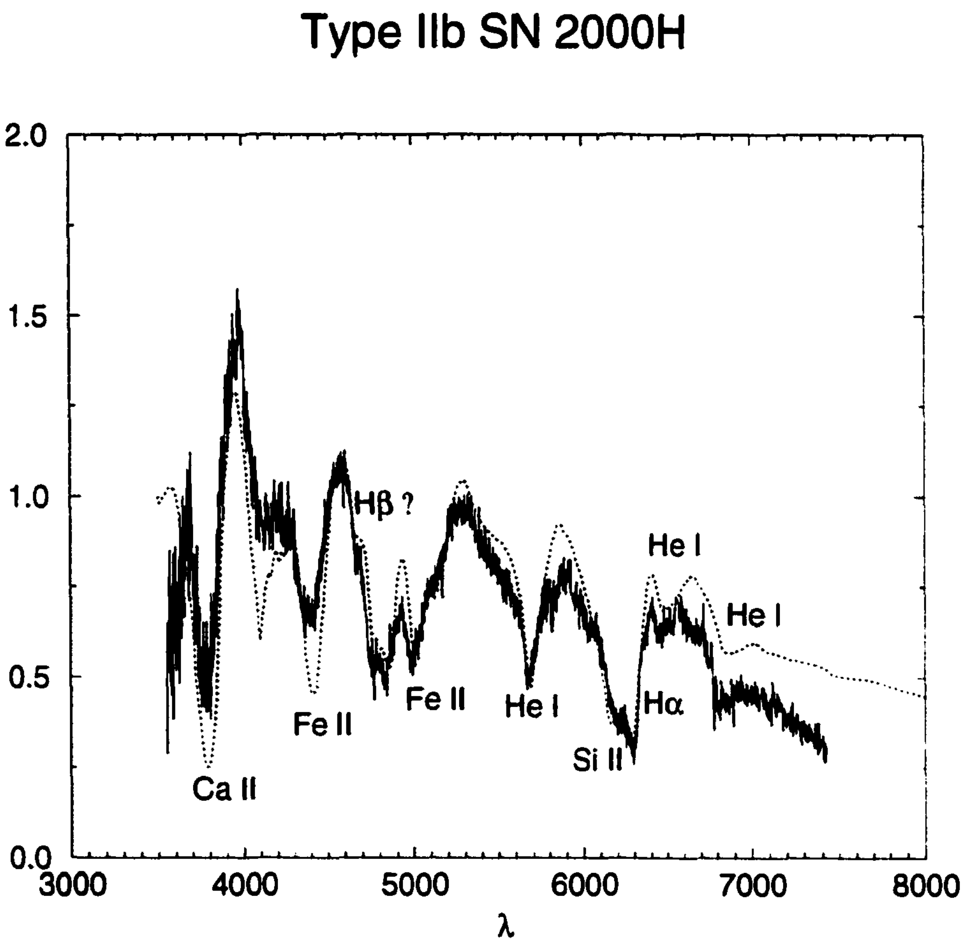

Figure 9.1: The observed spectrum is provided by Peter Garnavich.

Chapter 10

References

- Barbon, R., Iijima, T., & Rosino, L. 1989, A&A, 220, 83
- Bonanos, A. et al. 2000, in preparation
- Branch, D. 1987a, ApJ, 316, L81
- Branch, D. 1987b, ApJ, 320, L121
- Branch, D. 1998, ARAA, 36, 17
- Branch, D., et al. 1983, ApJ, 270, 123
- Branch, D., et al. 1993, AJ, 106, 2383
- Branch, D., Doggett, J. B., Nomoto, K., & Thielemann, F.-K. 1985, ApJ, 294, 619
- Branch, D., van den Bergh, S., 1993, AJ, 105, 2231
- Castor, J. I. 1970, MNRAS, 149, 111
- Clocchiatti, A., et al. 1997, ApJ, 483, 675
- Deaton, J., Branch, D., Fisher, A., & Baron, E. 1998, in preparation
- Filippenko, A. V. 1997a, in Thermonuclear Supernovae, ed. P. Ruiz-Lapuente, R. Canal, & J. Isern, Kluwer, Dordrecht, p. 1
- Filippenko, A. V. 1997b, ARA&A, 35, 309
- Filippenko, A. V., et al. 1992a, AJ, 104, 1543
- Filippenko, A. V., et al. 1992b, ApJ, 384, L15
- Filippenko, A. V., et al. 1995, ApJ, 450, L11

• Fisher, A., 2000, PhD thesis, University of Oklahoma

• Fisher, A., Branch, D., Nugent, P., & Baron, E. 1997, ApJ, 481, L89

• Fisher, A., Branch, D., Hatano, K., Baron, E., 1999, MNRAS, 304, 67 (FBHB)

• Garnavich, P. et al. 1999, IAUC 7190

• Garnavich, P. M. et al. 2000, in preparation

• Hamuy, M. et al. 1996, AJ, 112, 2438

• Harkness, R. P. 1991a, in Supernovae, ed. S. E. Woosley (New York, Springer), 454

• Harkness, R. P. 1991b, in SN1987A and Other Supernovae, ed. I. J. Danziger & K. Kjär (Garching, ESO), 447

• Harkness, R. P., et al. 1987, ApJ, 317, 355

• Hatano, K., Branch, D., Fisher, A., Baron, E., Filippenko, A. V., 1999b, ApJ, 525, 881

• Hatano, K., Branch, D., Fisher, A., Millard, J., Baron, E., 1999a, ApJS, 121, 233

• Hatano, K., Branch, D., Qiu, Y. L., Baron, E., Thielemann, F.-K., & Fisher, A. 2000a, ApJ, submitted

• Hatano, K., Branch, D., Lentz, E. J., Baron, E., Filippenko, A. V., & Garnavich, P. 2000b, ApJL, submitted

• Hernandez, M., et al. 2000, MNRAS, in press

• Hillebrandt, W., & Niemeyer, J. C. 2000, ARAA, in press

• Höflich, P. 1995, ApJ, 443, 89

• Höflich, P., Khokhlov, A., Wheeler, J. C., Phillips, M. M., Suntzeff, N. B., & Hamuy, M. 1996, ApJ, 472, L81

• Höflich, P., Wheeler, J. C., & Thielemann, F.-K. 1998, ApJ, 495, 617

• Iwamoto, K., Brachwitz, F., Nomoto, K., Kishimoto, N., Umeda, H., Hix, W. R., & Thielemann, F.-K., 1999, ApJS, 125, 439

• Jeffery, D. J., Leibundgut, B., Kirshner, R. P., Benetti, S., Branch, D., & Sonneborn, G. 1992, ApJ, 397, 304

• Jeffery, D. J., & Branch, D. 1990, in Jerusalem Winter School for Theoretical Physics, Vol. 6, Supernovae, ed. J. C. Wheeler, T. Piran, & S. Weinberg (Singapore, World Scientific), 90

- Jeffery, D. J., Branch, D., Filippenko, A. V., & Nomoto, K. 1991, ApJ, 377, L89
- Jha, S. et al., 1999, ApJS, 125, 73
- Khokhlov, A. J., Müller, E., & Höflich, P. 1993, A&A, 270, 223
- Kirshner, R. P., et al. 1993, ApJ, 415, 589
- Kobayashi, C., Tsujimoto, T., Nomoto, K., Hachisu, I., & Kato, M. 1998, ApJ, 503, L155
- Leibundgut, B., et al. 1991, ApJ, 371, L23
- Leibundgut, B., et al. 1993, AJ, 105, 301
- Lentz, E., Baron, E., Branch, D., & Hauschildt, P. 2000b, in preparation
- Lentz, E., Baron, E., Branch, D., Hauschildt, P., & Nugent, P. 2000a, ApJ, 530, 966
- Li, W. D., et al., 1999, AJ, 117, 2709
- Livne, E. 1999, ApJ, 527, 97
- Livne, E. and Arnett, W. D. 1995, ApJ, 452, 62
- Lucy, L. B. 1991, ApJ, 383, 308
- Marietta, E., Burrows, A., & Fryxell, B. 2000, ApJS, ??, 516
- Mazzali, P. A., & Chugai, N. 1995, A&A, 303, 118
- Mazzali, P. A., Danziger, I. J., & Turatto, M. 1995, A&A, 297, 509
- Mazzali, P. A., & Lucy, L. B. 1998, MNRAS, 295, 428
- McCall, M. L., et al. 1984, MNRAS, 210, 839
- Meikle, W. P. S. et al. 1996, MNRAS, 281, 263
- Meikle, W. P. S. & Hernandez, M. 1999, J. Ital. Astr. Soc., in press
- Millard, J. et al., 1999, ApJ, 527, 746
- Nomoto, K., Thielemann, F.-K., & Yokoi, K. 1984, ApJ, 286, 644
- Nugent, P., Baron, E., Branch, D. Fisher, A., & Hauschildt, P. H. 1997, ApJ, 485, 812
- Nugent, P. E., Baron, E., Hauschildt, P. H., Branch, D., 1995b, ApJ, 441, L33

• Nugent, P. E., Phillips, M. M., Baron, E., Branch, D., Hauschildt, P., 1995a, ApJ, 455, L147

• Oke, J. B. & Searle, L. 1974, ARAA, 12, 315

• Parodi, B. R., Saha, A., Sandage, A., & Tammann, G. A., 2000, ApJ, in press

• Patat, F., Benetti, S., Cappellaro, E., Danziger, I. J., Della Valle, M., Mazzali, P. A., & Turatto, M. 1996, MNRAS, 278, 111

• Perlmutter, S. et al. 1999, ApJ, in press

• Phillips, M. M., 1993, ApJ, 413, L105

• Phillips, M. M., Lira, P., Suntzeff, N. B., Schommer, R. A., Hamuy, M., & Maza, J. 1999, AJ, 118, 1766

• Phillips, M. M., et al. 1987, PASP, 99, 592

• Phillips, M. M., et al. 1992, AJ, 103, 1632

• Richmond, M. W., et al. 1995, AJ, 109, 2121

• Riess, A. G. et al. 1998, AJ, 116, 1009

• Riess, A. G. et al. 1999a, AJ, 117, 707

• Riess, A. G. et al. 1999b. AJ, 118, 2675

• Ruiz-Lapuente, P., Cappellaro, E., Turatto, M., Gouiffes, C., Danziger, I. J., Della Valle, M., Lucy, L. B., 1992, ApJ, 387, L33

• Schaefer, B. E., 1996, ApJ, 460, L19

• Schaefer, B. E., 1998, ApJ, 509, 80

• Schmidt, B. P., et al. 1994, ApJ, 434, L19

• Shigeyama, T., et al. 1992, ApJ, 386, L13

• Sobolev, V. V. 1960, Moving Envelopes of Stars (Cambridge, Harvard University)

• Sparks, W. B., Macchetto, F., Panagia, N., Boffi, F. R., Branch, D., Hazen, M. L., Della Valle, M., 1999, ApJ, 523, 585

• Suntzeff, N. B. et al., 1999, AJ, 117, 1175

• Treffers, R. R., Filippenko, A. V., Van Dyk, S. D., & Richmond, M. W. 1994, IAU Circ. No. 5946

• Tripp, R. 1998, A&A, 331, 815

- Tripp, R., & Branch, D. 1999, ApJ, 525, 209
- Vacca, W. D., & Leibundgut, B. 1996, ApJ, 471, L37
- Wang, L., Wheeler, J. C., Li, Z., & Clocchiatti, A. 1996, ApJ, 467, 435
- Wegner, G., & McMahan, R. K. 1987, AJ, 92, 287
- Wells, L. A., et al. 1994, AJ, 108, 2233
- Wheeler, J. C., Harkness, R. P., Khokhlov, A. M., & Höflich, P. 1995, Phys. Rep., 256, 211
- Wheeler, J. C., Höflich, P., Harkness, R. P., & Spyromilio, J. 1998, ApJ, 496, 908
- Wheeler, J. C. & Levreault, R. 1985, ApJ, 294, L17
- Yamaoka, H., Nomoto, K., Shigeyama, T., Thielemann, F.-K., 1992, ApJ, 393, L55